

TARGETING LOCOREGIONAL CHARACTERISTICS OF NEOPLASMS

A Dissertation

by

RYAN MICHAEL CLANTON

Submitted to the Office of Graduate and Professional Studies of
Texas A&M University
in partial fulfillment of the requirements for the degree of

DOCTOR OF PHILOSOPHY

Chair of Committee,	John Ford
Co-Chair of Committee,	Rodolfo Aramayo
Committee Members,	Koichi Kobayashi
	Julian Leibowitz
	Michael Deveau
Head of Department,	Yassin Hassan

December 2017

Major Subject: Nuclear Engineering

Copyright 2017 Ryan Michael Clanton

ABSTRACT

The selective delivery of radionuclides to cancerous tissues remains a problematic issue. The lack of specificity and sensitivity for many therapeutic and diagnostic strategies limits their safety and efficacy by putting healthy organs and tissues at risk. This is especially true for lung tumors, which seem to have limited blood flow. Therefore, therapeutic and diagnostic strategies with high specificity are needed to overcome these limitations. Metastases are the main cause of patient deaths, accounting for approximately 90%. It is therefore imperative that a systemic targeting approach be developed that is specific to the tumor microenvironment rather than a single target. The specific aims of this dissertation were to: 1) develop radiolabeled gold nanoparticles (AuNPs) for tumor therapy and imaging, 2) develop a nose-only mouse nebulizer system for use with/within optical or radioisotope imaging equipment, and 3) test the theranostic nanoparticles and nebulizer system on a mouse lung tumor bearing model. The first aim was performed by synthesizing I-125, Au-198, and As-211 AuNPs. The second aim utilized Solidworks 3D CAD software and employed 3D printing technology for fabrication. The third aim was performed with fluorescent Cy5.5 labeled nanoparticles designed to be used for diagnostic imaging.

ACKNOWLEDGEMENTS

I would like to thank my friends and family for their support during this endeavor. I would also like to thank the Texas A&M Institute for Preclinical Studies and the department of Nuclear Engineering for helping me fund and pursue this research in their labs. I would like to thank Dr. Akabani, Dr. Aramayo, and Dr. Ford for their guidance throughout different timepoints of my Ph.D. research. I would like to thank Zaher Hamoui for his production of ^{198}Au and his help in synthesis of the nanoparticles. I would also like to thank Thomas Michael Martin for his production of ^{211}At for synthesis of radioactive nanoparticles. I would like to thank my undergraduate students, Andrew Butters and Soleil Hernandez for helping me on the nebulization system and some of the writing/research. I would also like to thank the Texas A&M Engineering Innovation Center for supporting me in the prototyping and printing of these nebulization bed devices. I also want to extend my gratitude to Dr. Ronan MacLoughlin and Aerogen, INC., which provided the ultrasonic mesh nebulizer. Finally, I would like to thank Justin Smolen and the Dr. Wooley's lab for their mouse model and expertise needed in helping me complete characterization of the mouse nebulizer bed system.

CONTRIBUTORS AND FUNDING SOURCES

Contributors

This work was supported by a dissertation committee consisting of Professor John Ford [Advisor] and Professor Rodolfo Aramayo [Co-advisor] of the Department of Nuclear Engineering and Biology. The committee further consisted of Professor Koichi Kobayashi and Professor Julian Leibowitz of the Department of Microbial Pathogenesis and Immunology as well as Professor Michael Deveau of the Department of Small Animal Clinical Sciences.

Zaher Hamoui contributed to the production of ^{198}Au , synthesis of the nanoparticles, and data analysis of ^{198}Au nanoparticles. Thomas Michael Martin contributed to the production of ^{211}At and the synthesis of those radioactive nanoparticles. The undergraduate students, Andrew Butters and Soleil Hernandez, helped in development of the nebulization system and some of the writing/research about nebulizers. Gamal Akabani and Ronan MacLoughlin for the Aerogen INC. nebulizer insert and its characterization. All other work conducted on the dissertation was completed by the student.

Funding Sources

Graduate study was partially funded by the Department of Energy, grant numbers DE-SC0007371 and DE-SC0008433, the U.S. Nuclear Regulatory Commission, grant

number NRS-38-10-923, and the National Space Biomedical Research Institute Mentored Research Fellowship in Space Life Sciences (NASA NCC 9-58). I was also supported in part by assistantships from the Department of Nuclear Engineering and Biology at Texas A&M University. The content of this research is the sole responsibility of the authors and do not necessarily represent the official views of the Department of Energy.

NOMENCLATURE

ABCB1	ATP Binding Cassette Subfamily B Member 1
ADME	Absorption, Distribution, Metabolism, and Elimination
ADFs	Actin Depolymerization Factors
AuNP	Gold Nanoparticles
Au-I-NPs	Non-Radioactive Iodinated Gold Nanoparticles
BMDCs	Bone Marrow Derived Cells
CCD	Charge-Coupled Device
CD	Clusters of Differentiation
CI	Cell Index
CPP	Cell-Penetrating Peptide
CSCs	Cancer Stem Cells
CT	Computerized Tomography
CTCs	Circulating Tumor Cells
CXCR4	Chemokine Receptor Type 4
CLI	Cherenkov Luminescence Imaging
Dstrn	Dextrin
DIUF	Deionized Ultra-Filtered
DSB	Double Strand Breaks
Dynlrb1 or KM23-1	Dynein Light Chain Roadblock-Type 1

EDC	<i>N</i> -(3-dimethylaminopropyl)- <i>N</i> '-ethylcarbodiimide hydrochloride or 1-Ethyl-3-Carbodiimide hydrochloride
EDS	Electron Diffraction Spectroscopy
EPR	Enhanced Permeability and Retention
FBS	Fetal Bovine Serum
FGF2	Type 2 Fibroblast Growth Factor
GSD	Geometric Standard Deviation
HAuCl ₄	Gold (III) Chloride Trihydrate
HIF-1 α	Hypoxia Inducible Factor 1
HIV-1 TAT	Human Immunodeficiency Virus Type-1 Trans-Activating Regulatory Protein
HPGe	High-Purity Germanium Detector
HRTM	Human Respiratory Tract Model
ICRP	International Commission on Radiological Protection
IL3	Inferior Lobe
IL-4	Interleukin-4
Iqgap1	IQ-domain GTPase-activating protein-1
LET	Linear Energy Transfer
LL5	Left Lung
mAb	Monoclonal antibody
MGCs	Multinucleated Giant Cells
ML2	Middle Lobe

MPPD	Multiple-Path Particle Dosimetry Model
MR	Molecular Radiotherapy
MRD	Minimum Residual Disease
MRI	Molecular Resonance Imaging
MFR/PTPNS1	Macrophage Fusion Receptor
MSCs	Mesenchymal Stem Cells
MMAD	Mass Median Aerodynamic Diameter
MMP	Matrix Metalloproteinase
MDR1	Multidrug Resistance Protein 1
Na ₃ C ₆ H ₅ O ₇	Sodium Citrate
NCRP	National Council on Radiation Protection and Measurement
NHS	N-hydroxysuccinimide
NMAD	Number Median Aerodynamic Diameter
NSC	Nuclear Science Center
NSG	NOD/SCID IL-2-Receptor Gamma Deficient
PAMs	Pulmonary Alveolar Macrophages
PBST	PBS Tween
PCL4	Post-Caval Lobe
PEG	Polyethylene Glycol
PET	Positron Emission Tomography
ROS	Reactive Oxygen Species
RNOS	Reactive Nitrogen Oxide Species

RTCA	Real-Time Cell Analyzer
SASP	Senescence-Associated Secretory Phenotype
SA- β -Gal	Senescence-Associated β -Galactosidase
SCID	Severe Combined Immune Deficiency Mutation
SDF1	Stromal Cell-Derived Factor 1
SL1	Superior Lobe 1
SMAD	Surface Median Aerodynamic Diameter
SNARE	Soluble NSF Attachment Protein Receptor
SPECT	Single Photon Emission Tomography
SSB	Single Strand Breaks
STL	Stereolithography
Sufo-NHS	N-hydroxysulfosuccinimide
TCP	Tumor Control Probability
TEM	Transmission Electron Tomography
TLC	Total Lung Capacity
TNTs	Tunneling Nanotubes
TRT	Targeted Radionuclide Therapy
VCAM1	Vascular Cell Adhesion Molecule
Vcan	Versican
VMAD	Volume Median Aerodynamic Diameter
XRD	X-Ray Diffraction

TABLE OF CONTENTS

	Page
ABSTRACT	ii
ACKNOWLEDGEMENTS	iii
CONTRIBUTORS AND FUNDING SOURCES.....	iv
NOMENCLATURE.....	vi
TABLE OF CONTENTS	x
LIST OF FIGURES.....	xiii
LIST OF TABLES	xviii
CHAPTER I INTRODUCTION AND LITERATURE REVIEW	1
1.1. The Theories of Carcinogenesis.....	1
1.1.1. Inflammation	1
1.1.2. Mitochondrial Dysfunction	2
1.1.3. Radiation Carcinogenesis and Genetics	4
1.1.4. Cancer Stem Cells	6
1.1.5. Cell Fusion	7
1.1.6. Aneuploidy and Chromosome Instability.....	8
1.1.7. De-differentiation and Trans-differentiation.....	10
1.1.8. Potential Microbial Contribution.....	12
1.1.9. Fusion/Adhesion Molecules	13
1.1.10. Tunneling Nanotubes	16
1.1.11. Hypoxia	19
1.1.12. Reactive Oxygen Species and Aldehydes	21
1.1.13. Summary	24
1.2. Paradigm of Radiation Therapy	26
1.3. Enhanced Permeability and Retention	35
1.4. PEGylation for Stabilization, Labeling, and Targeting.....	37
1.5. The Radiochemical/biological Properties of ¹⁹⁸ Au.....	39
1.6. The Radiochemical/biological Properties of ¹²⁵ I.....	40
1.7. The Radiochemical/biological Properties of ²¹¹ At.....	42
1.8. Combining AuNPs with Radionuclides	46
1.9. Synthesis of ¹²⁵ I/ ²¹¹ At-AuNPs.....	48
1.10. Synthesis of Fluorescent AuNPs Probes	50
1.11. Delivery of Theranostics to the Lungs	51

1.12.	The Merit of Nebulizers in Drug Delivery to the Lungs and Therapy.....	53
1.13.	The Vibrating Mesh Atomizer	54
1.14.	Aerosol Characterization.....	55
1.15.	Comparison of Human and Mouse Lungs.....	56
1.16.	Particle Deposition Mechanisms.....	59
1.17.	Clearance Mechanisms.....	61
1.17.1.	Clearance via the Mucociliary Escalator.....	61
1.17.2.	Pulmonary Alveolar Macrophages	62
1.17.3.	Particle Translocation.....	63
1.18.	Models.....	64
CHAPTER II MATERIALS AND METHODS		66
2.1.	Production of Radioactive ^{198}Au Gold Nanoparticles.....	66
2.2.	Production of Radioactive ^{125}I Integrated Gold Nanoparticles	70
2.3.	Non-radioactive Iodine Nanoparticle Synthesis.....	72
2.4.	Production of Radioactive ^{211}At Integrated Gold Nanoparticles	73
2.5.	Nanoparticle Characterization.....	74
2.6.	Nebulizer System Design:.....	77
2.7.	Manufacturing	78
2.8.	Atomizer and Particle Distribution	79
2.9.	In-vivo/Ex-vivo Imaging Equipment	81
2.10.	Integration	84
2.11.	Anesthesia System.....	85
2.12.	Mixing Chamber	85
2.13.	Exhaust/Aerosol Removal System	86
2.14.	Physiological Monitoring.....	87
2.15.	Containment & Isolation System	88
2.16.	Cytotoxicity.....	89
2.17.	Mouse Imaging and Nebulizer System Characterization.....	90
CHAPTER III RESULTS		94
3.1.	SKBr-3 RTCA cell seeding experiments	94
3.2.	Estimation of number of ^{198}Au radioactive atoms per nanoparticle.....	95
3.3.	Characterization of $^{198}\text{AuNPs}$	99
3.4.	Cytotoxicity of $^{198}\text{AuNPs}$ and $^{198}\text{AuNPs-HIV-1 Tat}$	100
3.5.	Determining Influence of Time on Iodine Addition	103
3.6.	Characterization of Iodine Integrated AuNPs	104
3.7.	Activity distribution of Iodine Integrated AuNPs	108
3.8.	Astatine-211 Integrated Nanoparticles	110
3.9.	Characterization of Nebulizer	111
3.10.	Mouse Nebulization Studies	112
CHAPTER IV DISCUSSION AND FUTURE WORK		119

CHAPTER V CONCLUSIONS	133
REFERENCES	138

LIST OF FIGURES

	Page
Figure 1. Summary of radiation, oxidative stress, cell fusion, and cancer. Adapted with permission (Clanton et al. 2015).....	25
Figure 2. In vitro studies using tumor spheroids showing that internalization of antigen reaches a steady state with diffusion, which limits penetration and thus therapy effectiveness. Depending on antigen concentration, antigen plateaus at different depths within the spheroid. Reprinted with permission (Ackerman, Pawlowski, and Wittrup 2008).	30
Figure 3. Beta-gal expression of invasion-related genes after various single radiation doses showing an enhancement at doses below 2 Gy and subsequent reduction afterwards. The genes involved were <i>Dstn</i> , <i>Iqgap1</i> , <i>Vcan</i> , and <i>Dynlrb1</i> . These four genes are involved in cell proliferation, angiogenesis, invasion and migration adapted from data obtained in previous study (Loesch et al. 2015).	33
Figure 4. Gold nanoparticles (AuNPs) offer unique opportunities as carriers in the delivery of theranostically relevant compounds to the tumor via the enhanced permeability and retention effect (EPR).....	36
Figure 5. A relative comparison of radiobiological characteristics of various radiations as a function of absorbed dose, showing the relatively superior effectiveness of high-LET radiation, such as alpha-particles and auger electrons. X-rays and beta particles would be on the low-LET curve.....	45
Figure 6. Comparison of the human (right) and mice (left) lung.	57
Figure 7. Mechanisms of particle deposition in the airways. Depending on the diameter and velocity of the particle the mechanisms are inertial impaction, gravitational sedimentation, and diffusion.	60
Figure 8. Experimental apparatus to produce gold nanoparticles: (1) heat block with round bottom insert for heat transfer purposes; (2) 100 ml round bottom flask (3-neck), containing stir bar and reactants; (3) reflux column; (4) charcoal in cotton to act as a filter; (5) cold water inlet for reflux column; (6) reflux water outlet; (7) hot plate.	68
Figure 9. (A) UV-Vis absorbance as a function wavelength (nm) for different AuNP standards of 5, 10, 15, 20, 30, 40, 60, 80 and 100 nm in diameter obtained using a spectrophotometer (NanoDrop 2000C, Thermo Scientific, Inc.). (B) Absorbance peak as a function nanoparticle diameter obtained using	

different AuNP standards of 5, 10, 15, 20, 30, 40, 60, 80 and 100 nm. The relationship found was $A = 5.1602 \times 10^2 + 1.1918 \times 10^{-1} \times D + 4.5615 \times 10^{-3} \times D^2$ with a correlation coefficient of $R = 0.99905$. Adapted with permission (Hamoui 2015).	74
Figure 10. (A) The extinction coefficient, ϵ , as a function of nanoparticle diameter, d , was previously estimated by Liu et al., (Liu et al. 2007). Therefore, this estimation was compared with those calculated using the standards supplied by CytoDiagnostics, Inc. (B) Then a comparison between gold nanoparticle concentrations obtained from standards versus those calculated using the extinction coefficient, ϵ , given by the equation established from Liu et al., (Liu et al. 2007). The difference between our standards and those calculated were within reasonable range of each other. Adapted with permission (Hamoui 2015).....	76
Figure 11. Preliminary design of the mouse nebulizer (cross-sections) to be implemented with the micro-PET/CT. The AeroGen, Inc. nebulizer inlet is located on top the system and the anesthesia gas mixture inlet are on the back. A vacuum outlet allows for the clearance of the cavity to prevent condensation.	79
Figure 12. On the left is the particle-size distribution of aerosols produced by an AeroGen/Aeroneb, Inc. mesh nebulizer sold by Harvard Apparatus (Apparatus 2017). On the right is the aerosol deposition fraction vs particle size in mice obtained via simulations with Multiple-Path Particle Dosimetry Model (MPPD) software (Anjilvel and Asgharian 1995; National Institute for Public Health and the Environment (RIVM) 2002). Head: animal head; TB: tracheobronchial tree; P: parenchyma.	80
Figure 13. Detailed diagram of the AlbiraSi®, images supplied by courtesy of Bruker PCI with permission.	81
Figure 14. Detailed diagram of the Bruker In-vivo Xtreme®, images supplied by courtesy of Bruker PCI with permission.	83
Figure 15. The assembly of the device with vacuum and anesthesia lines connected in the rear and the AeroGen nebulizer mounted on top and integrated into the Albira Si.....	84
Figure 16. The vacuum system used during experimentation. This vacuum system would remove any potential leakage of fluorescent probe or radionuclide from the mouse housing portion of the nebulizer system.	87

Figure 17. This figure portrays the BIOPAC respiratory gating detector. This detector will allow monitoring of the mouse breathing and how much aerosol is being delivered based on the breathing pattern.	88
Figure 18. This figure depicts how each lobe of the mouse lungs was characterized before being split up for imaging.....	92
Figure 19. RTCA cell Index (CI) response as a function of time for seeding per well of 3,300 (pink), 5,000 (blue), 10,000 (green) and 25,000 (red) per well. The optimal seeding was determined at 10,000 cells per well within a time lapse of less than 196 h. Reprinted from (Hamoui 2015).	94
Figure 20. TEM figures of in-house produced AuNPs and schematic representation showing the functionalization of a radioactive AuNP using PEGylation methods and attachment of the cell penetrating peptide HIV-1-Tat. Reprinted with permission (Hamoui 2015).	96
Figure 21. Depicted is a poisson distribution for the fraction or probability of having a certain number of radioactive atoms of ^{198}Au per nanoparticle as a function of SA (MBq mg^{-1}). The potential fraction of nanoparticle that will have zero radioactive atoms decreases exponentially as a function of SA. The nominal diameter for the nanoparticles used in these calculations was 15.9 nm. Adapted with permission (Hamoui 2015).....	98
Figure 22. In this figure (A) is the UV-Vis spectrum of radioactive gold nanoparticles, and (B) is TEM image analysis, which demonstrated a narrow particle size distribution, with a size range between 11.6 and 23.5 nm and an average diameter of 15.9 nm. The surface plasmon resonance had a maximum peak observed around 525 nm with an absorbance of 1.341 corresponding to a gold nanoparticle diameter of 32.9 nm at a concentration of 2.29×10^{11} NP/ml. A lognormal distribution was fitted to the data which depicted a negative skew of the measured distribution towards larger size nanoparticles. In collaboration with Hamoui with permission (Hamoui 2015).	100
Figure 23. (A) Normalized Cell Index as a function of time for SKBr-3 cells exposed to nonradioactive AuNP (green line) and control (red line). (B) Normalized Cell Index as a function of time for SKBr-3 cells exposed to $^{198}\text{AuNPs}$ -HIV-1 Tat with an activity of 50 kBq (green line) and 100 kBq (blue line), $^{198}\text{AuNPs}$ with an activity of 50 kBq (pink line) and 100 kBq (brown line), and control (red line). (C) Normalized Cell Index as a function of time for SKBr-3 cells exposed to $^{198}\text{AuNPs}$ -HIV-1 Tat (green line) and $^{198}\text{AuNPs}$ (blue line) with an activity of 500 kBq and control (red line). (D) Normalized Cell Index as a function of time for SKBr-3 cells exposed to $^{198}\text{AuNPs}$ -HIV-1 Tat with an activity of 1000 kBq (green line) and 1500	

<p> kBq (blue line), ¹⁹⁸AuNPs with an activity of 1000 kBq (pink line) and 1500 kBq (brown line), and control (red line). The solid black lines represent the incubation time between the addition of the AuNP and the time when the medium was replaced. In collaboration with Hamoui with permission (Hamoui 2015). </p>	102
<p> Figure 24. Estimated diameter of AuNPs using UV-Vis obtained with nonradioactive sodium iodine (NaI) added at different time points following after addition of sodium citrate during AuNP synthesis. Reprinted with permission (Clanton et al. 2017). </p>	104
<p> Figure 25. The solutions of the gold nanoparticle containing different quantities of iodine in fetal bovine serum and phosphate buffer saline are depicted. The larger the amount of iodine added the more stable the nanoparticles appear in phosphate buffer saline. Reprinted with permission from (Clanton et al. 2017). </p>	107
<p> Figure 26. TEM image of AuNPs synthesized with non-radioactive iodine. The average diameter was 20 ± 5 nm (95% CI). Reprinted with permission from (Clanton et al. 2017). </p>	108
<p> Figure 27. This figure presents Poisson distributions assessing the fraction of radioactive atoms per nanoparticle. The average diameter of an AuNP was 20 nm. Reprinted with permission from (Clanton et al. 2017). </p>	109
<p> Figure 28. Distribution of radioactive atoms per nanoparticle based on a nominal mean of $\mu = 1.47$. The fraction of nanoparticles with no radioactive atoms was 0.23, and the fraction with one or more radioactive atoms was 0.77. </p>	111
<p> Figure 29. <i>Ex Vivo</i> imaging was performed on each lobe of the mouse lungs. In A and B, from top left to bottom right the lobes are arranged from superior lobe (SL1), middle lobe (ML2), inferior lobe (IL3), post-caval lobe (PCL4), and left lung (LL5). Signal of tape on right of each dish is reflectance. The settings were 690 nm for the excitation and 750 nm for emission. A is the control mouse and B is 170907F. These images were set to minimum intensity of 300 and a maximum intensity of 800. </p>	112
<p> Figure 30. This figure depicts the multiarea time lapse of the left lung for (A) control with very low auto-fluorescence, (B) control with some auto-fluorescence/bubbles, (C) Cy5.5-PEG-Au-I-Nps, and (D) Cy5.5-PEG-AuNPs. </p>	115
<p> Figure 31. Confocal images of micelle dispersion in each of the 5 mouse lung lobes utilizing the mouse nebulizer system developed. As can be seen, the </p>	

nebulizer system can deliver the micelles to every portion of the mouse lungs..... 117

Figure 32. This is a side by side comparison of the mouse nebulization delivery technique compared to the previously performed method of intratracheal delivery. These are all the left lung and as can be observed results with the nebulization delivery were more repeatable and consistent then intratracheal delivery. 118

Figure 33. Proposed mechanisms of integration into gold nanoparticles occurring via collisions of iodine induced citrate displaced regions. Collisions could potentially occur between averaged sized nanoparticles or smaller nanoparticles on larger nanoparticles. The lines depict interactions with neighboring molecules. Reprinted with permission (Clanton et al. 2017). 125

LIST OF TABLES

	Page
Table 1. The mice were split into two groups either having the AuNPs or the Au-I-NPs and are categorized below.....	91
Table 2. The distribution of signal in sum intensity or counts per square centimeter for each lobe of the lungs for each mouse examined in this study.....	113
Table 3. The Sum of (Pico-Watts per square millimeter) signal normalized by the area in squared cm for each lobe, divided into AuNP or Au-I-NP delivery, of the lungs for each mouse examined in this study.	113

CHAPTER I

INTRODUCTION AND LITERATURE REVIEW

1.1. The Theories of Carcinogenesis

Without a deeper understanding of how cancer develops it will be difficult to pursue unique features of the tumor microenvironment in order to treat cancer. In other words, it is not easy to solve a problem until the problem is understood. As such, I will begin by discussing the different but highly related cancer etiologies (Clanton et al. 2015).

1.1.1. Inflammation

Rudolf Virchow was a pioneer in cancer research during the mid-1800s when he hypothesized that cancer develops in areas of chronic inflammation. He proposed a hypothesis that cancer arose from inflammatory sites, which he based on his observations that inflammatory cells infiltrated solid tumors in a similar process to wound healing (Sanford 2005; Virchow 1865; Balkwill and Mantovani 2001; Landskron et al. 2014). While Virchow was in Germany, Louis Pasteur was in France developing the idea of bacteriology, which investigated the invasion of foreign pathogens and how they potentially contribute to disease (Smith 2012). Virchow had complex feelings about this concept. He didn't believe that pathogens caused cancer because many individuals, with the same types of pathogens, were perfectly healthy compared to those that had cancer but he did believe that microbes could potentially produce substances that caused the inflammation leading to cancer.

We now know that they were both correct. To show their connection, the hypoxia inducible factor 1 α (HIF-1 α), which is responsible for hypoxia, also increases the survival of phagocytic cells in a hypoxic environment (Hong et al. 2014). It is also a key component of wound healing, infection, and tumor formation (Zinkernagel, Johnson, and Nizet 2007; Hong et al. 2014; Semenza 2002). It has also been shown to be induced by lipopolysaccharides or other compounds produced by bacteria (Werth et al. 2010). One key component of the papers mentioned above is that HIF-1 α seems to be directly correlated to migration of not only immune cells but the cancer cells indicating some similarity between the two (Semenza 2002; Hong et al. 2014).

1.1.2. Mitochondrial Dysfunction

Following Virchow, Warburg in 1924 hypothesized that mitochondrial dysfunction could lead to cell death or immortalization (Warburg 1956; Warburg 1924). The main evidence for this was the observed switch from aerobic to anaerobic respiration. He also noticed a significant increase in the production of reactive oxygen species (ROS) by cancer cells (inflammation) (Wallace 2005b). Hypoxia and ROS seem to be deeply interconnected and studies suggest that hypoxia can induce oxidative stress via an over-generation of ROS (Pialoux et al. 2009). Furthermore, hypoxia can result in mitochondrial dysfunction, leading to ROS production (Fearon et al. 2016; Weinberg et al. 2000). Mitochondrial dysfunction can be the result of an inadequate number of mitochondria, inability to provide necessary substrates, or a dysfunction in the electron transport chain and ATP-synthesis machinery (Nicolson 2014). This mitochondrial

uncoupling or the abrogation of ATP synthesis, has been shown to be in response to the mitochondria's membrane potential, which has been shown to promote the Warburg effect, potentially contributing to chemoresistance (Samudio, Fiegl, and Andreeff 2009).

To compensate for mitochondrial dysfunction three situations can occur, (1) fusion of partially dysfunctional mitochondria allowing functional components of damaged mitochondria to compensate for each other, (2) the generation of entirely new mitochondria by fission, and (3) mitophagy, which is the removal and complete degradation of dysfunctional mitochondrial (Nicolson 2014). Therefore, mitochondrial dysfunction brings about an alteration in the ratio of mitochondrial fission to fusion events, resulting in either an excess of long chain (i.e. MCF7) or clustered mitochondrial fragments (i.e. MDA-MB-231 and MDA-MB-436) (Zhao et al. 2013). This process is regulated by four proteins; mitochondrial fusion protein 1, mitochondrial fusion protein 2, optic atrophy type 1, and dynamin-related protein 1. Dynamin-related protein 1 is of particular interest because it is involved in the fission process that leads to mitochondrial fragmentation. This fragmentation and expression of dynamin-related protein 1 have been shown to be 2.5 to 5-fold higher in MDA-MB-231 and MDA-MB-436 than in MCF7 and as such seems to contribute to a 10-fold higher migratory and invasive potential in these two MDA cell lines (Zhao, Zhou, and Li 2016). Silencing dynamin-related protein 1 inhibits glioma cell proliferation and invasion via the RHOA/ROCK1 pathway (Yin et al. 2016).

The quantity of mitochondrial fragmentation can be directly linked to the exacerbation of lamellipodia formation resulting in increased motility/protrusion, driving the metastatic potential of cancer cells (Rehman et al. 2012). Lamellipodia are the key features at the front leading edge of motile cells and are believed to be the key formations required for cell migration, thus they drive the metastatic potential of cancer cells (Zhao, Zhou, and Li 2016). Silencing dynamin-related protein 1 or overexpressing mitochondrial fusion protein one (presenting long chain in MCF7) inhibition of lamellipodia formation was shown to occur (Zhao, Zhou, and Li 2016).

1.1.3. Radiation Carcinogenesis and Genetics

The theory of radiation carcinogenesis was brought about with the discovery of radiation and as a consequence of scientific curiosity. X-rays were first discovered by Wilhelm Röntgen in 1895 (Sansare, Khanna, and Karjodkar 2011). X-rays would almost immediately enter the medical field for dental radiographs and other cranial imaging procedures where there was indications of hair loss in patients and many individuals were obtaining hand burns and loss of skin due to excess exposure (Sansare, Khanna, and Karjodkar 2011). This brought about radiotherapy when a Viennese physician Leopold Freund, provided the first scientific proof of the biological effectiveness of X-rays against tissue abnormalities such as a huge *nervus pigmentosus pilosus* (hair nerves) on the back of a 5-year old girl (Kogelnik 1998). It wasn't until Hermann Joseph Muller in three experiments performed between 1926 and 1927 that it was demonstrated that X-rays could cause genetic mutations and changes in the genome (Muller 1927).

Radiation carcinogenesis categorizes cell damage into two groups, the first being direct due to direct interactions of radiation with cell components and the second being indirect damage due to the ROS that is formed from radiation imparting energy to water, which then causes damage to the cell (Biaglow 1981). Double strand breaks (DSBs) and cluster damage are considered the main culprits behind carcinogenesis. Clustered DNA damage occurs when two or more lesions are formed within one or two helical turns of the DNA. Clustered Damage is made up of DSBs with base lesions or abasic sites, non-DSB clusters of base lesions, and abasic sites and single strand breaks (Eccles, O'Neill, and Lomax 2011). These impair the repair process and can cause genetic mutations that cause apoptosis or loss of growth control, propagating into cancer (Eccles, O'Neill, and Lomax 2011). Therefore, at the present, radiation biologists have continually emphasized that ROS are not the main culprit of mutagenesis. This is because ROS produce three orders of magnitude more single strand breaks (SSBs) than they do double strand breaks (Caldecott 2008). As such damage done by radiation, which has a significant amount of cluster damage and DSBs, is considered to have a higher risk of mutagenesis. DSBs also take up to an hour before a human cell will recognize them and begin the repair process. This would mean there is a significant amount of time for additional DSBs to form and inappropriate rejoining to occur. Thus it makes sense why the clonal theory of cancer development suggests that all cancers originate from the accumulation of genetic alterations in a single cell and how radiation promotes these alterations more than inflammation (Sąsiadek and Karpiński 2009).

1.1.4. Cancer Stem Cells

Over the past decade significant research has been placed into the separation and isolation of specific subsets of tumorigenic cells, most specifically cancer stem cells (CSCs), from solid tumors. These CSCs have one or a couple distinct cellular markers, such as membrane antigens representing their cluster of differentiation (CD), that separate them from non-tumorigenic cells (Al-Hajj et al. 2003; Bonnet and Dick 1997; Haraguchi et al. 2006; Olempska et al. 2007; Lapidot et al. 1994; O'Brien et al. 2007; Prince et al. 2007; Ricci-Vitiani et al. 2007; Schatton et al. 2008; Seigel et al. 2007; Singh et al. 2003; Singh et al. 2004; Wang et al. 2007; Zen et al. 2007). CSCs are like normal stem cells in their self-renewal capacity, unlimited proliferative potential, infrequent or slow replication cycles, and resistance to toxic xenobiotics as well as radiation. CSCs also share high DNA repair capacity and the ability to give rise to daughter cells that differentiate (Hadnagy et al. 2006; Hirschmann-Jax et al. 2004). Conversely, CSCs differ from stem cells in that they demonstrate dysregulated self-renewal or differentiation programs and instead of new, healthy tissues can form new tumors instead (Hermann et al. 2007). Their daughter cells can also undergo cell cycle arrest at various stages of differentiation and have limited proliferative potential. Furthermore, even though these daughter cells make up the bulk of a tumor, represented by their rapid replication, they have a very limited metastatic potential (Bagley and Teicher 2009). Thus, CSCs appear to be the main culprit of metastasis (Hermann et al. 2007).

1.1.5. Cell Fusion

More theories have recently been developed or re-defined by myself and other researchers to bring light to certain features unexplained by the cancer stem cell theory (Lu and Kang 2011; Zhou et al. 2015; Kemp, Wilkins, and Scolding 2014; Clanton et al. 2015). For example, cell fusion as a mechanism of tumorigenesis was first postulated by Otto Aichel in the 1900s (Lu and Kang 2009).

Cell fusion is one of the most underappreciated phenomena in the human body; being prevalent in a wide range of physiological and pathological conditions from fertilization, tissue development during embryogenesis, osteoclastogenesis, and during the repair of various tissues. Cell fusion can be split into two categories and classified as either homotypic or heterotypic (Lu and Kang 2011). Homotypic fusion is when two cells with the same end fate undergo fusion predominantly resulting in a stem cell with the same functions of the previous two. Heterotypic fusion is when two cells that are different undergo fusion resulting in either a heterokaryon (hybrid with two nuclei) or syncharyons (hybrid developed from nuclear fusion) (Lu and Kang 2011).

The heterokaryons could potentially be associated with the multi-nucleated giant cells while the synkaryons would most likely be linked with those that have lost chromosomes (aneuploidy) and are rapidly dividing (Lu and Kang 2011). Early evidence dates back to the late 60's and early 70's when scientists were labeling thymidines of circulating monocytes with tritium which were later found within the multi-nucleated giant cells

(MGCs) of inflammation induced lesions (Murch et al. 1982). Further evidence of cell fusion resulting in inflammatory MGCs was shown by Murch *et. al.* back in 1982 (Murch et al. 1982).

Inflammation seems to be one of the key triggers in cell fusion, to exemplify this one study was capable of showing that the fusion process was amplified in response to irradiation but then subsequently inhibited through the administration of the anti-inflammatory corticosteroid prednisolone (Kemp, Wilkins, and Scolding 2014). As another example, the only known environmental risk factor for glioblastomas is ionizing radiation (Chandana et al. 2008; Braganza et al. 2012). As such, radiation is specifically known for inducing cell fusion on the blood brain barrier and at rates drastically higher than the amounts that would occur normally without exposure (Espejel, Romero, and Alvarez-Buylla 2009; Wiersema et al. 2008). If we look at melanin and neuromelanin as radioprotectants, or substances that prevent the inflammation and damage that would potentially result in increased cell fusion, then it begins to make sense why the incidence of glioblastomas in the Caucasian population is approximately double the incidence of the African American population (DeAngelis 2001).

1.1.6. Aneuploidy and Chromosome Instability

Aichel believed that the spontaneous fusion between somatic cells could lead to chromosomal abnormalities, which could propagate into cancer development. As such, aneuploidy, which is characterized as the presence of an abnormal number of

chromosomes in a cell, is present in virtually all solid tumors (Li et al. 2000). Cell fusion does not initially generate aneuploidy, but it does lead to tetraploidy, which has been shown to precede aneuploidy in both clinical and experimental models of cancer (Lu and Kang 2011; Heselmeyer et al. 1996; Fujiwara et al. 2005). Furthermore, the metastatic potential of a tumor cell population has also been linked to cell fusion by the enhancement of ploidy levels and chromosome duplications (Larizza and Schirmacher 1984). There have been many studies purporting evidence of *in-vivo* cell fusion occurring between tumor cells and normal host cells (Larizza and Schirmacher 1984). Even though the concept is dated, examples of how bone marrow-derived cells (BMDCs) are affecting the tumor population are continuing to arise, especially as therapeutic methods utilizing stem cells increase (Luo et al. 2014; Karnoub et al. 2007; Amariglio et al. 2009; Erdo et al. 2003).

What is very interesting is that even though cell fusion is a well-accepted and documented occurrence in normal tissues, it seems to be relatively ignored until recently in cancer research. As an example, there was a very interesting proof-of-concept by Zhou and his colleagues demonstrating that the fusion of cytogenetically stable cells can connect to oncogenesis and tumor development (Zhou et al. 2015). In Zhou's study, non-transformed rat intestinal epithelial cells were fused resulting in hybrid cells with an unstable aneuploid karyotype and elevated rates of DNA damage (Zhou et al. 2015). Furthermore, a population of the hybrid cells were highly tumorigenic in mice, forming a tumor after the injection of only 200 cells (Zhou et al. 2015).

1.1.7. De-differentiation and Trans-differentiation

To add on to what Otto Aichel first postulated, it should be emphasized that many variations of cell fusion can occur that could possibly contribute to the formation of a diverse array of heterogenic neoplastic cells. This may occur within the same tumor as well, creating opportunities for CSC populations with different CD markers to develop, making isolation and treatment of CSCs very arduous if based on these markers alone. The fusion of bone marrow derived cells (BMDCs) with Purkinje neurons, cardiomyocytes, and hepatocytes with evidence that trans-differentiation has been shown to occur, with no evidence of trans-differentiation without fusion (Chen et al. 2011; Alvarez-Dolado et al. 2003).

Trans-differentiation is a key characteristic of many tumors (Shekhani et al. 2013; Han et al. 2014). Since cell fusion occurs first upon the epithelial and endothelial tissues such as the vascular tissue, brain, skin, lungs, and intestines then this may provide evidence for their involvement of cancer development in these tissues (Silk et al. 2013; Jiang et al. 2004; Okamoto et al. 2002; Theise et al. 2000; Weimann, Charlton, et al. 2003; Johansson et al. 2008; Weimann, Johansson, et al. 2003).

Many researchers attributed the apparent plasticity of bone marrow derived stem cells to produce new liver cells, cardiomyocytes, and neurons to be trans-differentiation (conversion of one cell type to another), however new findings are suggesting cell fusion to be the reason of why cancer cells undergo trans-differentiation (Alvarez-Dolado et al.

2003). The most significant evidence of this is the fusion of somatic cells from different species of mammals (Croce 1976; Nowak-Imialek et al. 2010; Wang et al. 1998; Kemp et al. 2011). During development and tissue repair the fusion of whole cells or vesicle transfer of DNA between cells, each cell from different origins, is an important physiological process (Bjerkvig et al. 2005). As previously mentioned, Purkinje neurons, cardiomyocytes, and hepatocytes have been shown to undergo fusion with BMDCs with evidence that trans-differentiation occurring in these fused cells, which is a key characteristic of cancer cells (Chen et al. 2011; Shekhani et al. 2013; Han et al. 2014). Furthermore, experiments by Ying *et al.* and Terada *et al.* both showed that in situations where trans-differentiation was assessed that there was also evidence that cell fusion was occurring (Ying et al. 2002; Wurmser and Gage 2002; Terada et al. 2002). When this is taken into consideration, it makes the authors question how mouse embryos can be injected with teratocarcinoma cells of other another mouse and create chimeras with variable fur color and cancer rate dependent on the amount of teratocarcinoma cells injected (Illmensee and Mintz 1976; McBurney 1977; Papaioannou et al. 1978; Papaioannou et al. 1975).

Since embryonic stem cells are explicitly known for cell fusion, this should make the scientific community question whether the bone marrow derived cells can result in similar characteristics. To elaborate on this concept, teratomas, which are considered encapsulated tumors made up of different tissues or organs, are made from embryonic stem cells that didn't initially undergo differentiation during embryogenesis. As such

they share many similarities with tumor populations that most individuals have heard of. For example, the transplantation of undifferentiated murine embryonic stem cells into the heart can potentially result in them becoming active or beginning to develop into different tissues, with significant heterogeneity (Nussbaum et al. 2007). Teratomas are also usually benign but can also be metastatic (malignant) as well. Typical cancers can also be placed into two categories; either primary tumors (benign or malignant) or secondary tumors (always malignant) with both categories being well known for their heterogeneity in the neoplastic compartment (Lathia et al. 2011). These two categories are easily distinguished when looking at the brain. Primary brain tumors are tumors that begin in the brain and make up only 2% of all adult cancers in the United States (Chandana et al. 2008). Secondary brain tumors, also known as metastatic tumors, begin as cancers in other regions of the body (DeAngelis 2001; Yamamori et al. 2012). The previously mentioned MGCs are also sometimes found in Glioblastomas as well (Kozak and Moody 2009).

1.1.8. Potential Microbial Contribution

Considering many of the epithelial surfaces are where microbes thrive, it would be erroneous to ignore what potential effects they could have in cell fusion or in the complete differentiation of fused cells, which some microbes may induce directly but the main evidence points toward inflammation (Kespichayawattana et al. 2000; Johansson et al. 2008; Yamada et al. 2004; Verschoor et al. 1990). This is interesting and alarming since bacterial translocation to the blood occurs through various methods such as bug

bites, oral cavities, antibiotics, superficial wounds, and even chemotherapeutics can disrupt the gut barriers (McLaughlin et al. 2002; Swank and Deitch 1996; Gendron, Grenier, and Maheu-Robert 2000; Amar et al. 2011; Nakayama, Itoh, and Takahashi 1997; Berg 1983). Therefore, it is not surprising that the effects of bacteria continue in the microenvironment of the tumor as well. This may be either good or bad depending on the balance of bacteria and the type of bacteria within and around the tumor (Zhang 2014; Iida et al. 2013; Lokody 2014; Viaud et al. 2013; Yan et al. 2007; Boleij et al. 2012; Trinchieri 2013). Tumors, circulating tumor cells (CTCs), and metastasized tumors are all microenvironments in which certain bacteria can survive and thrive due to the growth factors that are produced and local immunosuppression (Morrissey, O'Sullivan, and Tangney 2010). This was clearly shown in a study performed by Yu, which found that bacteria could be injected straight into the blood stream, without any modification to make them specific to the cancer (Yu et al. 2004). In fact, they were highly effective at using light-emitting bacteria to see the preferred target neoplasms (Yu et al. 2004). Consequently, bacteria can be used for neoplasm targeting, a strategy that was first being investigated over 150 years ago when doctors were noticing shrinkage in tumor volume after purposeful infection with bacteria (Pawelek, Low, and Bermudes 2003).

1.1.9. Fusion/Adhesion Molecules

Considering Virchow's observations of the infiltrative inflammatory cells into neoplasms, it's no wonder that fusion of macrophages with tumor cells could potentially

take place and lead to the expression of macrophage antigens by tumor cells (Lazova, Chakraborty, and Pawelek 2011; Powell et al. 2011; Shabo and Svanvik 2011). Even the variant of the glycoprotein cell differentiation marker 44 (CD44v) that is proposed to be involved in some metastatic tumors is also transiently expressed by B and T lymphocytes and macrophages after antigenic stimulation (Arch et al. 1992). Thus, it cannot be ignored that CD44 is also an adhesion molecule used for macrophage fusion and when inhibited or blocked with antibodies prevents metastasis and repopulation, but not completely (Avin, Haimovich, and Hollander 2004; Cui et al. 2006; Guo et al. 1994; Orian-Rousseau 2010; Quere et al. 2011; Seiter et al. 1993; Sterling, Saginario, and Vignery 1998; Jin et al. 2006).

This is most likely because of the profuse and diverse amount of fusogens, or integral membrane proteins that enable cell fusion, that are present on cancer stem cell populations. Interestingly, many of the so called human fusogens have been contested and shown to be merely adhesion proteins that bring the cells closer together, making the fusion process easier (Noubissi et al. 2015). This would make looking for variants of CD markers an important consideration, as variants of CD markers exist in other cancers as well (Emlet et al. 2014; Kemper et al. 2010; Ferrandina et al. 2008).

Furthermore, CD47 is another fusogenic protein expressed by macrophages that has been found to be an adverse prognostic factor on human acute myeloid leukemia stem cells, the same cancer stem cells that also express the previously mentioned CD44

(Majeti et al. 2009; Quere et al. 2011; Chen and Olson 2005; Bjerkvig et al. 2005).

Therefore, multiple variants or the expression of certain CD markers may propagate or progressively enhance the invasiveness of cancer stem cells when they are present together.

Another receptor is the P2Z/P2X7 receptor, whose expression level has been directly correlated to the amount of spontaneous cell fusion occurring in macrophage cultures, while also being highly expressed by primary bone tumors; as well as neuroblastoma, breast, and prostate cancers (Chiozzi et al. 1997; Adinolfi, Amoroso, and Giuliani 2012).

Another important marker is the tetraspanin family protein, CD9, the only protein that has been shown to be indispensable in sperm-egg fusion, while also being a cancer stem cell marker for various cancers (Ghani et al. 2011; Nishida et al. 2009; Chen and Olson 2005; Wang and Han 2015; Kawashima et al. 2002; Kischel et al. 2012; Rappa et al. 2015). To add to the diversity of fusogenic substances, interleukin-4 (IL-4), PTPNS1 (also known as the macrophage fusion receptor, MFR), Chemokine Receptor type 4 (CXCR4, receptor and ligand), and stromal cell-derived factor 1 (SDF1) have also been linked to the cell fusion process and with cancer stem cells as well (Bjerkvig et al. 2005; Rempel et al. 2000; Kucia et al. 2005; Gelmini et al. 2008; Teicher and Fricker 2010). The expression of both SDF1 and CXCR4 are actually directly correlated with increasing tumor grade and angiogenic potential in human glioblastoma (Rempel et al. 2000).

1.1.10. Tunneling Nanotubes

Even though cell fusion has been shown to occur in various degrees between immune cells, stem cells, and normal cells, the exact mechanism is not fully known, especially since there doesn't seem to be any involvement by α -helical bundles (the core components of fusogen soluble NSF attachment protein receptors (SNAREs) and Class I viral fusion proteins) (Chen and Olson 2005). This is where I believe tunneling nanotubes, which are normally made up of F-actin bundles, sometimes microtubules, that allow for the creation of membrane channels utilized for cell-to-cell communication and transfer of organelles (like mitochondria), Golgi vesicles, and even DNA to neighboring and distant cells become of importance (Gerdes, Bukoreshtliev, and Barroso 2007; Lou, Fujisawa, Barlas, et al. 2012; Wang and Gerdes 2015; Bukoreshtliev et al. 2009). TNTs have also been referred to in the literature as membrane nanotubes, intercellular bridges, epithelial bridges, or cytoplasmic extensions (Lou, Fujisawa, Barlas, et al. 2012). They have been found to extensively form in many cancers (Lou, Fujisawa, Barlas, et al. 2012; Lou, Fujisawa, Morozov, et al. 2012). The potential importance of tunneling nanotubes in cell fusion can be seen with the osteoclasts, which are multinucleated cells formed by the cellular fusion of hematopoietic stem cell derived osteoclast precursors; but only after the formation of abundant amounts of TNTs (Kukita et al. 2015).

This makes the formation of TNTs a viable mechanism for how membrane fusion or fusion pores occur before complete cell fusion. This is corroborated by how

constitutively active Drac, which controls actin polymerization, or loss of function of Kette, which regulates actin dynamics and F-actin organization (processes that both regulate TNT formation), each block the late stage formation of fusion pores during myoblast fusion (Chen and Olson 2005; Bogdan and Klambt 2003). Furthermore, virus-induced cell-cell fusion has been blocked by perturbation of the actin cytoskeleton by expression of dominant negative Rac GTPase (Chen and Olson 2005; Pontow et al. 2004).

TNTs may be the main contributor or first step in the cell fusion process, while also providing a route for the transfer of mitochondria, DNA, and protein when there is dysfunction, damage, or deficiency. This is a very unsettling as it could potentially mean that substances can be transferred to neoplasms that could make them more resistant to the drugs used against it. This was explicitly seen in a study that found TNTs to be a novel means of transferring drug resistance via the functional intercellular transfer of P-glycoprotein, ATP Binding Cassette Subfamily B Member 1 (ABCB1), also known as multidrug resistance protein 1 (MDR1) (Ambudkar et al. 2005). The signals received may also invoke complete repair of the cell via nuclear fusion. However, this leaves the question of why nuclear fusion and not apoptosis with subsequent replacement? This may be that localized apoptosis would result in tissue instability/function or that the fusion process may be necessary to reconstitute the tissue stem cell population. What is also interesting is that 41% of malignant melanomas and 21% of lung cancers (50% being of small cell carcinoma origin) metastasize to the brain and that those metastatic

cell populations express macrophage-specific antigens (Ruff and Pert 1984; Pawelek 2007). A combination of the previously mentioned CD markers, cytokines, chemokines, and fusogens with these TNTs would drastically enhance the facilitation of cell fusion. They are also potential contributors to the specific niches that cancer cells preferentially metastasize to or invade.

This means that TNTs, filopodia, and lamellipodia must be collectively considered when talking about cancer stem cell fusion, invasion, and metastasis. A study by Nickolay *et al* back in 2009 corroborated this when he found that selective elimination of filopodia from PC12 cells blocked TNT formation with only weak effects on the stability of already existing TNTs (Bukoreshtliev et al. 2009). This would seem to imply that either the processes regulating filopodia also regulate the formation of TNTs or that there is a complex relationship between the two. I suggest that the TNTs provide the network for travel or the communication of where the cells should travel while the filopodia and lamellipodia allow for invasion and locomotion. The real importance of the study presented by Nickolay *et al* is that elimination of the filopodia by the CytoB did not cause a statistical difference in the phagocytic uptake of cellular debris, demonstrating that filopodia are not a sole cause (Bukoreshtliev et al. 2009). Jay *et al.* showed that the formation of the previously mentioned foreign body giant cells are preceded by lamellipodia formation, where Rac activation controlled not only lamellipodial formation but the fusion process as well (Jay et al. 2007). However, inhibitors of Rac activation also only prevent cell fusion, not phagocytosis (Jay et al. 2007).

1.1.11. Hypoxia

Continuing with fusogens and tunneling nanotubes we should also consider hypoxia. Not much research has been successfully made into why the hypoxic regions are occurring besides the fact that proliferation may induce stress that causes the vasculature to collapse. The problems this author has with these theories are that they don't explain how cysts and other growths, such as moles, can undergo active proliferation with increased blood flow instead of hypoxia. However, activation of HIF-1 α is a general phenomenon associated the hypoxic regions of neoplasms, while also being induced by lipopolysaccharides or other compounds produced by bacteria (Werth et al. 2010). This is because HIF-1 α is associated with the host's innate immune functions to help the specialized phagocytic cells function in the hypoxic microenvironments of infected tissues (Zinkernagel, Johnson, and Nizet 2007).

Since another consequence of induced HIF-1 α is increased metastasis and invasion, the degree of fusogenic (expression of fusogens and facilitation of fusion)/phagocytotic (cell engulfment but predominantly for degradation) ability of CSCs would be directly proportional to invasiveness along with survival (Jing et al. 2012; Lu and Kang 2011). To emphasize these two phenomena and their complex interplay, macrophages will undergo cell fusion when they are unable to phagocytize, resulting in foreign body giant cell formation (Jay et al. 2010). This process has been shown to require matrix metalloproteinase (MMP)-9, a highly expressed substance in a variety of cancers that is also believed to contribute significantly to invasion (MacLauchlan et al. 2009; Chen et

al. 2013; Duffy et al. 2000). Considering the pro-survival responses of many cancer cells and the high prevalence of macrophage antigens on cancer stem cells this leaves a very concerning dilemma. Could the body's own immune system be contributing to cancer formation via cell fusion and as such can immune cells transfer invasion properties and survival mechanisms to hypoxic environments?

As previously mentioned, the expression of both SDF1 and CXCR4 are actually increased with increasing tumor grade as well as angiogenesis in human glioblastoma (Rempel et al. 2000). HIF-1 α actually enhances expression of SDF1, which then increases the adhesion, migration, and homing of circulating CXCR4 positive progenitor cells to ischemic tissues (Ceradini et al. 2004).

Apoptosis has also been shown to be a contributor to cancer cell fusion and breast cancer metastasis (Noubissi et al. 2015). This was corroborated with astrocytes requiring p53 activations to induce TNT development (Wang, Cui, et al. 2011). Even more interestingly, hypoxia was what was shown to induce the apoptosis that enhanced the fusion of breast cancer cell lines with mesenchymal stem cells (MSCs), resulting in hybrids with an enhanced migratory capacity (Noubissi et al. 2015). Considering that Fas has been shown to stimulate the formation of nanotubes between T lymphocytes during extrinsic apoptotic death, this would seem to also suggest a link between hypoxia and TNT formation (Arkwright et al. 2010; Luchetti et al. 2012). The hybrid cells or those that underwent cell fusion, were shown to have the motility representative of the

MSCs but the T47D breast cancer cell lines themselves did not (Noubissi et al. 2015). As such, this is especially troublesome as these breast cancer cells in question were non-metastatic until fusion occurred with the MSCs (Noubissi et al. 2015). Cell fusion has found to more predominately occur in hypoxic regions rather than normoxic regions; this can be explicitly shown by how the adhesion protein found to promote the fusion of hematopoietic progenitor cells with cardiomyocytes, vascular cell adhesion molecule (VCAM-1) is up-regulated in hypoxic environments (Noubissi et al. 2015).

Therefore, hypoxia seems to be either a very beneficial or detrimental situation depending on the outcome. Either hypoxia occurs and the body can control the growth of the tumor and fused cells become stable or conversely hypoxia results in cell fusion leading to some combination of increased metastatic ability, invasiveness, or stem-ness in an area that is about to up-regulate blood flow due to unchecked angiogenic gene expressions in response to the hypoxia. By increasing our understanding of this phenomenon, we can then begin to develop treatments that use stem cells to cause differentiation in a tissue by making them without invasive genes and with proper signals for cell death.

1.1.12. Reactive Oxygen Species and Aldehydes

The indirect reactions of ionizing radiation interacting with water have the ability to produce (ROS) in biological systems (Riley 1994). A common characteristic of these reactions is that the body responds to ROS by perceiving it as a threat and causing more

inflammation, often due to the mitochondria or senescence-associated secretory phenotype (SASP), in the affected tissues (Azzam, de Toledo, and Little 2003; Leach et al. 2001; Yamamori et al. 2012). This increase is believed to be the foundation of why the bystander effect occurs after radiation treatments at a single tumor site (Shao et al. 2003; Chen, Zhao, et al. 2009).

The propagation of these radiation-induced, mitochondria-dependent responses by the cells, and the immune system could propagate into a hazardous situation where a large concentration of ROS, reactive nitrogen oxide species (RNOS), and aldehydes are situated within a localized area. Even though acute amounts of ROS are used every day for beneficial activities such as inducing stem cell differentiation, chronic exposures to ROS have never been associated with a beneficial outcome. This phenomenon is referred to as the ROS paradox in which ROS is an essential biomolecule utilized in the regulation of cellular functions and as toxic by-products of metabolism (Thannickal and Fanburg 2000). The only difference appears to be in the ROS concentrations, where the ROS occur, and what by-products are formed by the ROS (Thannickal and Fanburg 2000).

The downstream effects of oxidative stressors and their mutagenic capacities need to be taken into consideration as well. The primary targets of oxidative stressors are DNA, proteins, and lipids. Free radicals also have a tendency of directly attacking polyunsaturated fatty acids in the membrane and resulting in a process known as lipid

peroxidation (Cabisco, Tamarit, and Ros 2000). The most chemoresistant cancer cells have already been linked to mitochondrial uncoupling and preferential oxidation of fatty acids (Samudio, Fiegl, and Andreeff 2009). A primary effect of lipid peroxidation is a decrease in the cell's membrane fluidity, which alters the cell's membrane properties and bound proteins (Samudio, Fiegl, and Andreeff 2009). As a result, the cell's ability to receive paracrine signals becomes limited. This effect acts as an amplifier to free radical production and lipid peroxidation that will result in larger concentrations of aldehyde by-products (Samudio, Fiegl, and Andreeff 2009).

Aldehydes are extremely reactive, have long lives (~9 minutes), and can diffuse out from their site of origin and preferentially attack distant sites with high lipid and DNA specificity (Cabisco, Tamarit, and Ros 2000). The lifespan of ROS in the cytoplasm may explain why they don't cause much damage when induced in the cytoplasm. However, their ability to produce aldehydes via lipid peroxidation could explain why there is a need for processes to prevent them from reacting with the cell membrane or organelle membranes. In contrast to ROS, the aldehydes can induce a significant amount of cluster damage, SSBs, and DSBs (Cabisco, Tamarit, and Ros 2000). The most intensively researched aldehydes such as melonaldehyde and 4-hydroxyalkenals will produce SSBs and DSBs in the DNA backbone, adducts of base and sugar groups, cross-linkage to other molecules, and lesions that block replication (Cabisco, Tamarit, and Ros 2000).

These lesions that block replication are what I believe are truly important in controlling tumors, as they result in replicative senescence. Senescent cells are characterized by the irreversible proliferative arrest accompanied by characteristic changes in gene expression, metabolism, and cell morphology. Recently, aldehydes have been proposed to play the key role in the induction of radiation-induced senescence as aldehyde-scavenging compounds can prevent senescence induction (Flor, Doshi, and Kron 2016). Interestingly, almost every CSC and CTC that has been isolated and analyzed has also been shown to have up-regulated expressions of aldehyde dehydrogenases (Chen, Chen, et al. 2009; Charafe-Jauffret et al. 2010; Ucar et al. 2009; Marcato, Dean, Pan, et al. 2011; Marcato, Dean, Giacomantonio, et al. 2011). The daughter cells of these CSCs will either die or survive based on their continued expression of these enzymes.

1.1.13. Summary

An outline of effects after radiation exposure and the role of cell fusion and ROS is presented in figure 1. First radiation, as previously mentioned radiation first deposits energy creating excitations and Ionizations causing direct effects such as DNA damage or indirect effects such as free radical production. Those free radicals can then further interact with DNA or interact with lipids in lipid peroxidation to cause aldehydes which can further interact with the DNA to cause ssb, dsbs, and cluster damage. Aldehydes can also interfere with methylation processes and effect genetic expressions leading to cancer as well. Depending on the degree of DNA damage their can be cell repair. Sometimes cell fusion is the repair process but cell fusion can be unstable and result in

the transfer of pluripotency markers and genetic mutations that lead to cancer.

Otherwise, DNA damage and genetic mutations can lead to cell death in the form of apoptosis or necrosis.

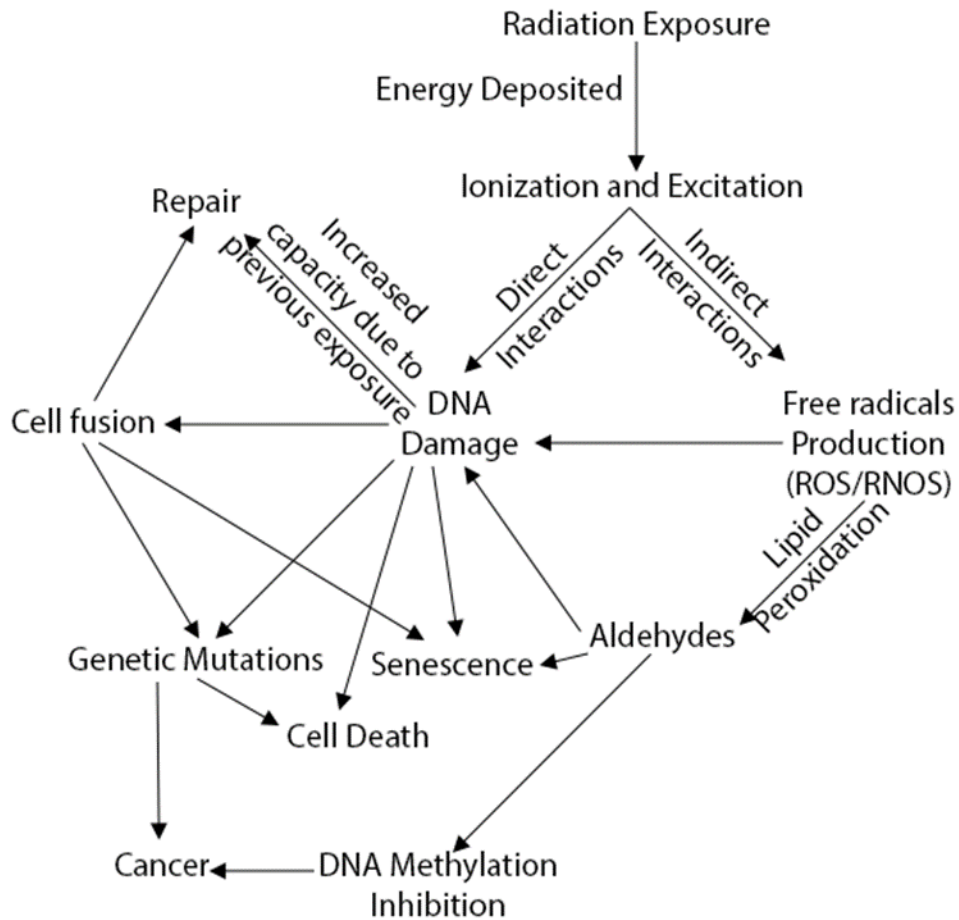


Figure 1. Summary of radiation, oxidative stress, cell fusion, and cancer. Adapted with permission (Clanton et al. 2015).

Based on all of the previously identified cancer etiologies it can be seen that inflammation, mitochondrial dysfunction, radiation, cancer stem cells, cell fusion, and

even immune responses are all potential contributors to oncogenesis. They are also not mutually exclusive to each other. Due to the overlap of all of these paradigms it is suggested that if genetic damage and mutations are the matches that light the fire in cancer development, then inflammation may be the fuel that feeds the flame. From this information, we decided that targeting mitochondrial dysfunction would be a good pursuit.

1.2. Paradigm of Radiation Therapy

The fact that radiation can cause the production of ROS and direct DNA damage makes it a dual edge sword, capable of both causing and treating cancer. Therefore, the intent of radiation therapy is to use ionizing radiation to kill cancer cells by damaging their DNA and inducing cell death or senescence, thereby stopping these cells from continuing to grow and divide. However, the selective bio-delivery of cytotoxic agents to target cancer cells with minimal adverse effects on healthy tissues remains a challenge when developing therapeutics (Emami et al. 1991; Stone et al. 2003). The most practical method of exposing cancer patients to radiation is through external-beam radiotherapy. With this approach, only a limited region of the body is irradiated with multiple beams of high-energy x-rays, which concentrate the absorbed dose to the tumor tissue and minimize the dose to normal surrounding tissues. On the other hand, molecular radiotherapy (MR) uses a molecular structure, such as a monoclonal antibody, that attaches to antigens or receptors located only on the surface of tumor cells or extracellular components unique to tumor tissue. This molecule is labeled with a

radionuclide to deliver a cytotoxic level of radiation to disseminated disease sites scattered around the body. Unlike tumor-directed drugs and toxins, which kill only the targeted cells that the compounds enter, an exclusive feature of radionuclides is that their radiative emissions (Auger electrons, beta and alpha particles) can exert a “crossfire” effect, potentially destroying adjacent tumor cells even if they do not over-express the specific tumor-associated antigen or receptor. Furthermore, molecular radiotherapeutics have the potential to eliminate both the primary tumor site and tumor cells that have spread throughout the body (metastases), including malignant cell populations that are undetectable by radiographic imaging, commonly referred to as minimal residual disease provided some means of making them specific and selective is found.

Molecular radiotherapy has been used with increasing frequency as new targeting modalities are created. Generally, the radiotherapeutic agent has two components: a radionuclide and a carrier that specifically targets to tumor tissue. Examples of molecular carriers are peptides, which seek and attach to their corresponding cell-surface receptors, and monoclonal antibodies, which attach to antigens that are also expressed on the surface of tumor cells. A radionuclide can be selected for its specific radiological characteristics, such as decay scheme, physical half-life, type of emitted radiation (e.g., alpha, beta particle and gamma emitter), and radiation range in tissue. It is this modularity, where the components can be varied like interlocking building blocks, which allows us to match the spatiotemporal pathophysiology specific to a tumor.

Clinically, the radionuclide ^{131}I (NaI) has been used for decades for the treatment of papillary differentiated thyroid carcinoma and for the treatment of progressive medullary thyroid carcinoma using pre-targeting strategies with anti-carcinoembryonic monoclonal antibodies followed by ^{131}I -labeled haptens (Salaun et al. 2012; Wong et al. 2000). For the case of Non-Hodgkin's lymphoma, ^{131}I -labeled anti-CD20 tositumomab monoclonal antibody (mAb) and ^{90}Y -labeled rituximab mAb have been used with great success extending the progression-free and overall median survival of patients (Martinez et al. 2017; Olney et al. 2014). Recently, the alpha-particle emitting $^{223}\text{RaCl}_2$ (Xofygo®) has been approved by the FDA for the treatment of metastatic castration-resistance prostate cancer showing positive results by increasing the progression-free survival of patients (Nilsson 2016; Pandit-Taskar, Larson, and Carrasquillo 2014). In all the above strategies, the combination of lethal or sub-lethal doses of radiation and the immunotherapeutic effects of the monoclonal antibody has resulted in positive clinical results.

The effectiveness of molecular radiotherapy depends on multiple factors, such as molecular parameters and pathophysiological barriers, including stability of the radiolabeled compound in serum and the unlabeled mAbs (IgG isotypes and fragments), plasma half-life, organ distribution or absorption, distribution, metabolism, and elimination (ADME), tumor affinity, penetration, uptake and internalization (Jain 1999; Ackerman, Pawlowski, and Wittrup 2008; Akabani, Kennel, and Zalutsky 2003). These limitations in molecular radiotherapy are exemplified in the literature (Ackerman,

Pawlowski, and Wittrup 2008) (Akabani, Kennel, and Zalutsky 2003). Figure 2 shows the limited penetration of an intact mAb using *in vitro* tumor spheroids, which elucidate the high interstitial tumor pressure encountered even in small tumor foci (Ackerman, Pawlowski, and Wittrup 2008). The *in vivo* limited distribution in tumor tissue of ^{125}I -labeled 210B mAb in a model of epithelial-to-mesenchymal transition (EMT)-tumor bearing mice of metastatic lung cancer has also been shown (Akabani, Kennel, and Zalutsky 2003). These examples demonstrate that molecular radiotherapy has significant limitations in the treatment of large solid tumors that need to be further addressed (Jain 1999). Most strategies are based on a binary system where a radionuclide is attached to a compound, with a very low labeling efficiency, typically between 2 and 5%. Radionuclide-compound dissociation via radiolysis continues to be a significant problem that needs to be addressed (Chong et al. 2008; Milenic, Brady, and Brechbiel 2004).

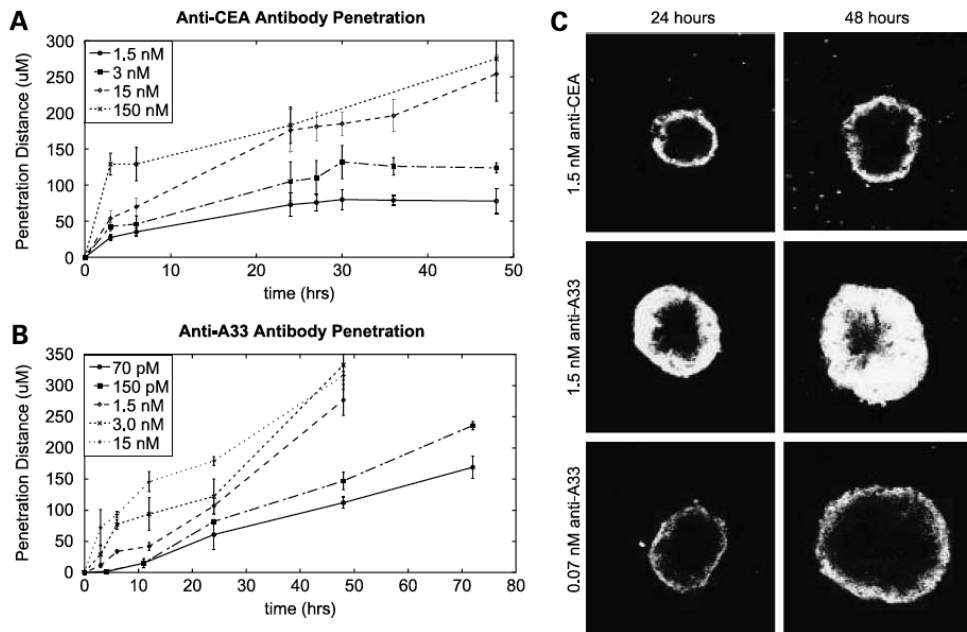


Figure 2. In vitro studies using tumor spheroids showing that internalization of antigen reaches a steady state with diffusion, which limits penetration and thus therapy effectiveness. Depending on antigen concentration, antigen plateaus at different depths within the spheroid. Reprinted with permission (Ackerman, Pawlowski, and Wittrup 2008).

The prospect of using molecular radiotherapy for the treatment of minimal residual and micro-metastatic disease however has gained significant attention within the paradigm of cancer stem cells (Mehlen and Puisieux 2006). As previously mentioned, there lies a sub-population of tumor cells with stem cell-like properties and significant ability for self-renewal (Lin et al. 2016). The niche, as it is commonly referred to in the open literature, is a cluster of tumor cells where cancer stem cells reside, and it can produce florid microvascular proliferation and fulminant progression. Even though the metastatic process is highly ineffective, it is estimated that about 90% of all cancer deaths are due to metastases (Mehlen and Puisieux 2006). Many research groups,

including ours, are tackling this paradigm by using high-linear energy transfer (LET) particle emitting radionuclides, such as I-125, Au-198, Ra-223, At-211, and Ac-225, with the help of nuclear nanotechnologies (Ceder and Elgqvist 2016; Alessio et al. 2017; Akabani et al. 2002).

This is because certain studies have elucidated that external beam radiotherapy has the potential to enhance angiogenesis, proliferation and thus speed up the process of metastases (Sofia Vala et al. 2010; Madani, De Neve, and Mareel 2008; Agemy et al. 2008; Lee et al. 2017). Recent studies have shown how radiation impacts the different compartments of the tumor microenvironment (Leroi et al. 2016). Our group, in collaboration with others, used mutant mouse embryonic stem cells (mESC) as surrogates of cancer stem cells, where we carried out a study to elucidate the effects of radiation dose fraction by screening genes involved in proliferation and invasiveness. Our findings indicated that a total of 13 genes were involved, seven of them previously implicated and six new genes that had not been implicated prior to our study (Loesch et al. 2015). Our results indicated a dose-dependent gene over-expression at 2 Gy per fraction or lower (hyper-fractionation) followed by a steady decline afterwards up to 14.5 Gy per fraction (hypo-fractionation, see Fig. 3). Destrin (Dstn) is an essential actin regulatory protein belonging to the actin-depolymerizing factor (ADF)/cofilin family, which are believed to control the actin-based cell motility (Carlier et al. 1997). A major property of ADF is its ability to enhance the *in-vitro* turnover rate called treadmilling of actin filaments to a value comparable to that seen *in-vivo* in motile lamellipodia, which

is due to ADF's ability to use ATP hydrolysis in actin assembly to enhance filament dynamics (Carlier et al. 1997). Dstn appears to be a direct contributor to stem cell-like and *Listeria monocytogenes*-like motility (Bamburg, McGough, and Ono 1999; Carlier et al. 1997). This small actin-binding protein is also considered to be one of the key regulators of actin remodeling of the cytoskeleton, which is a crucial part of cytokinesis, cell migration, and polarized cell growth along with cancer cell migration and invasion (Klose et al. 2012). They have been linked to poor prognosis in cancer patients (Klose et al. 2012; Estornes et al. 2007; Wang et al. 2004; Wang, Eddy, and Condeelis 2007). IQ-domain GTPase-activating protein-1 (Iqgap1) has been shown to have significant expression upon the invasive front of tumors (Dong et al. 2006; Miyamoto et al. 2000; Nabeshima et al. 2002). It binds type 2 fibroblast growth factor (FGF2) to the cognate receptor called Fibroblast growth factor receptor 1, on the actin filaments which provides the force for the previously mentioned lamellipodial protrusion (Benseñor et al. 2007). Versican (Vcan) is a proteoglycan with diverse roles in role in cell adhesion, proliferation, migration, and angiogenesis which are all components of invasion and metastasis (Rahmani et al. 2006). Has anti-adhesive properties (Sakko et al. 2003). Elevated levels of Vcan have been reported in most malignancies to date (Karamanos et al. 2012). Dynein Light Chain Roadblock-Type 1 (Dynlrb1 or Km23-1) is known as a motor protein that transports cargo within the cell but Km23-1 is also involved in the movement or migration of cells. Plays important role in TGF-beta signal transduction, most specifically Ras activation (Jin, Ding, and Mulder 2012). Knockdown has been

shown to decrease RhoA activation and inhibit human colon carcinoma cell invasion in wound healing assays (Jin et al. 2012).

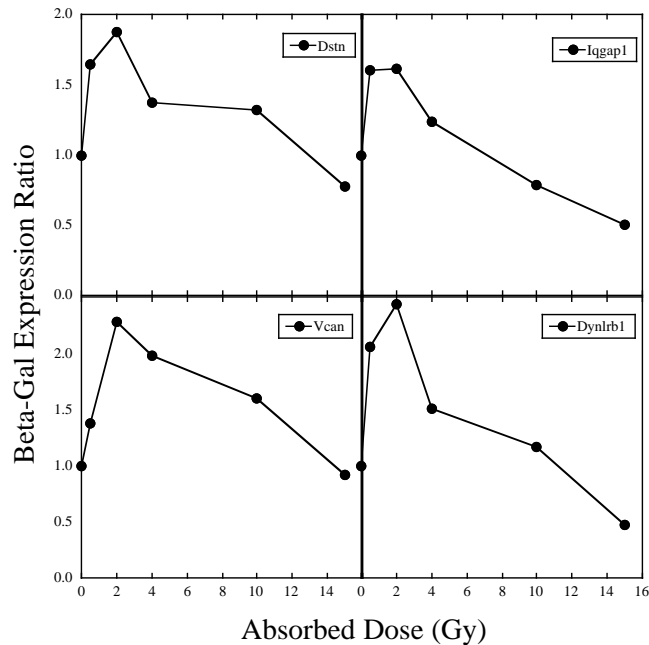


Figure 3. Beta-gal expression of invasion-related genes after various single radiation doses showing an enhancement at doses below 2 Gy and subsequent reduction afterwards. The genes involved were Dstn, Iqgap1, Vcan, and Dynlrb1. These four genes are involved in cell proliferation, angiogenesis, invasion and migration adapted from data obtained in previous study (Loesch et al. 2015).

The significance of this study indicates that radiation dose (dose per fraction) is potentially a powerful contributor to angiogenesis, proliferation and thus metastases, which is corroborated by multiple recent studies (Gu et al. 2015; Li et al. 2013; Grabham and Sharma 2013). Therefore, it has a significant impact in tumor control probability (TCP). Molecular radiotherapy, on the other hand, delivers radiation to target tissues stochastically at a low effective dose rate but very highly localized absorbed dose;

therefore, it is postulated that molecular radiotherapy would be more effective in treating minimal residual disease, small tumor foci and metastases, without enhancing the genes found to be involved in angiogenesis, proliferation and invasiveness. This is especially true if the radiation is high-LET, which has been shown to reduce metastasis and angiogenesis in contrast to x-rays (Bruland et al. 2008; Grabham and Sharma 2013). This is probably again related to the ability of high-LET radiation to produce significantly more aldehydes and thus senescence of the cancer cells (Zhang et al. 2016). Using senescence-associated β -galactosidase (SA- β -Gal) as a marker of senescence, data has shown that it takes 10 Gy X-rays (LET 4 keV/ μ m), 5 Gy Carbon (LET 80 keV/ μ m), and only 3 Gy for ^{56}Fe to begin to plateau in their ability to cause a percentage of 92-100 cells to express SA- β -Gal (Zhang et al. 2016). ^{56}Fe also plateaued around 100% of the cells while X-rays and carbons only plateaued around 60% of the cells showing expression (Zhang et al. 2016).

Our laboratory has produced radioactive nanoparticles using ^{211}At , ^{125}I and ^{198}Au functionalized with multiple agents, including cell-penetrating peptides, showed the cytotoxic capacity of these probes against cancer cells. Two of these, ^{211}At and ^{125}I , are high-LET radiation meaning they may be capable of reducing invasion and inducing senescence more effectively than X-rays as discussed previously. These nanoparticles will be the ones used in this dissertation research. We studied the microdosimetry characteristics of the nanoparticles (Hamoui 2015; Pulley 2015). The major benefit of having multiple radioactive atoms per nanoparticle is based on the capacity to deliver

multiple “hits” of highly focused energy deposition to a single cell structure, such as the cell nucleus or mitochondria of the same cell, thus increasing the probability of cell death. Therefore, nuclear nanotechnologies are considered a promising strategy in molecular radiotherapy.

1.3. Enhanced Permeability and Retention

Gold nanoparticles (AuNPs) offer unique opportunities in the delivery of biologically relevant compounds (e.g., radionuclides) due to the enhanced permeability and retention (EPR) in neoplasms (Ghosh et al. 2008; Peer et al. 2007). Yet, the mechanism of EPR, beyond the enhanced permeability of the tumor vasculature aiding the effect, hasn't been fully explained in the current literature. Once the AuNPs are within the neoplasm, it is believed they can enter cells via macropinocytosis or some other form of specialized endocytosis, with or without involvement of surface receptors. I suggest that the enhanced retention of AuNPs in cancer cells may also be caused, in part, by the interaction of AuNPs with the mitochondria because of mitochondrial dysfunction induced changes in electrostatic potential (See Fig. 4). As previously mentioned from Warburg's observations (Warburg 1924), the main evidence of mitochondrial dysfunction was the switch from aerobic to anaerobic respiration, which results in a significant increase in reactive oxygen species (ROS) in neoplastic cells (Wallace 2005b). Mitochondrial dysfunction has also been characterized by increases in mitochondrial fission, resulting in either an excess of long chain or clustered mitochondrial fragments frequently seen in neoplastic cells (Zhao et al. 2013; Alirol and

Martinou 2006; Wallace 2005a). More recently, studies have also found that the vitiation of ATP synthesis due to mitochondrial uncoupling in response to disruptions of the mitochondria's membrane potential, can promote the Warburg effect, potentially contributing to the chemoresistance of leukemia cells (Samudio, Fiegl, and Andreeff 2009). Therefore, to elaborate further we suggest that mitochondrial dysfunction leads to differences in mitochondrial membrane and/or surface potentials, which potentially enhance the EPR effect via electrostatic attraction.

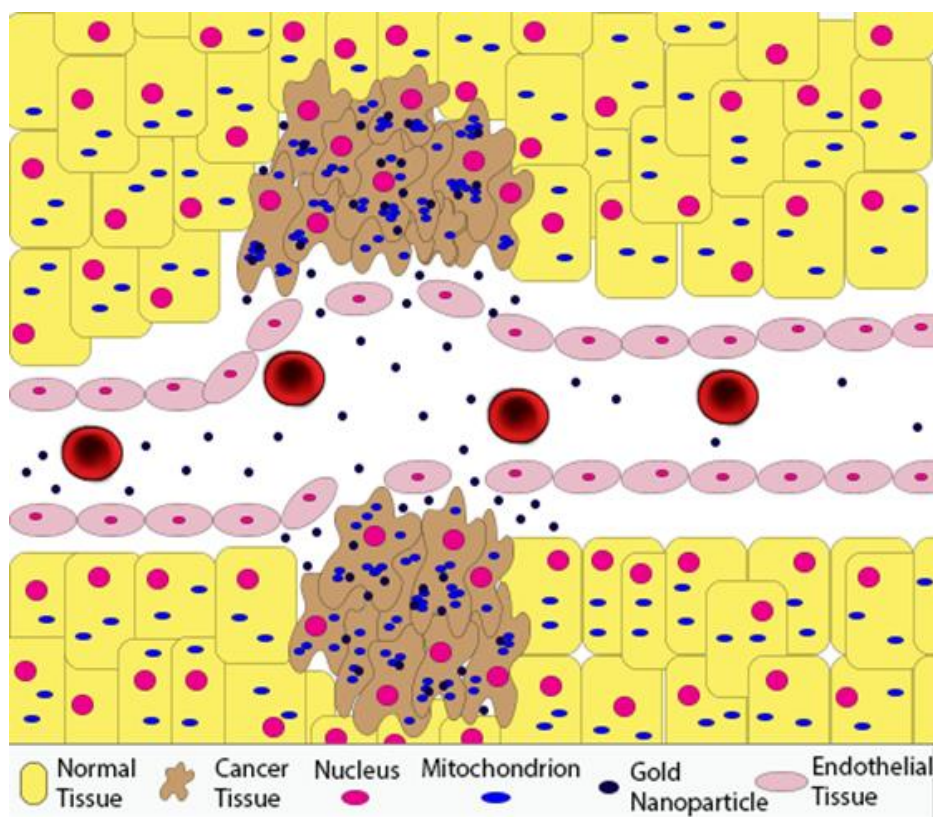


Figure 4. Gold nanoparticles (AuNPs) offer unique opportunities as carriers in the delivery of theranostically relevant compounds to the tumor via the enhanced permeability and retention effect (EPR).

To give credence to membrane and surface potentials enhancing the EPR effect, various studies have shown considerable internalization of AuNPs by cancer cells followed by their interaction with the mitochondria (internalization or adherence to membrane); in some instances, this mechanism was even used to try and induce apoptosis or radiosensitization of cancer cells (Mkandawire et al. 2015; Taggart et al. 2014; Yang et al. 2015). Other studies validated this assessment by showing that the mitochondrial surface potential has considerable influence on the uptake and even the potential cytotoxicity of gold nanoparticles (Zhao et al. 2012; Frohlich 2012). Varying the surface charges of the nanoparticles could therefore be the key to targeting the cancer stem cell sub-populations. For example, Liu et al. demonstrated the size and surface charge effects of gold nanoparticles on interactions with phagocytic and nonphagocytic cells, RAW 264.7 and HepG2 cells, respectively (Liu et al. 2013). Due to the phagocytic nature of cancer stem cells, the use of negatively charged nanoparticles may promote a cancer stem cell's uptake of nanoparticles preferentially over the non-phagocytic cells of healthy tissue. This is also seen with the metastatic and highly-invasive B16F10 melanoma populations, which take up nanoparticles readily and distributes them into their golgi apparatus and endoplasmic reticulum (Chang et al. 2008).

1.4. PEGylation for Stabilization, Labeling, and Targeting

Bare gold nanoparticles are unsuitable for *in vitro* and *in vivo* use, as they aggregate in the biological environment, resulting in negligible circulation and uptake by the tumor (Ting et al. 2010). We have found (unpublished results) that citrate-encapsulated gold

nanoparticles are unsuitable to nebulize due to aggregation. It is therefore necessary to provide a surface protectant to limit aggregation, as well as to provide targeting or aerosolizing properties. One method is to provide a biologically inert coating of polyethylene glycol (PEG) in a so-called “corona” (Ishii et al. 2004). In this case, 2-5 kDa PEG chains, labeled with a thiol group on one end, are put in solution with the gold nanoparticles at a ratio of 1000:1. The sulfur in the thiol compound covalently bonds to the gold nanoparticle surface, leaving the inert PEG corona to protect the nanoparticle, in a process known as PEGylation. In practice, variations in these PEG chains are included to tailor the chemical properties of the nanoparticles. Here, 2 kDa methoxy-PEG-thiol ($\text{CH}_3\text{O}-(\text{CH}_2\text{CH}_2\text{O})_n-\text{CH}_2\text{CH}_2\text{SH}$), with the chemically inert methoxy group, is mixed in a ratio of 98:2 with 5 kDa carboxymethyl-PEG-thiol ($\text{CH}_2\text{COOH}-(\text{CH}_2\text{CH}_2\text{O})_n-\text{CH}_2\text{CH}_2\text{SH}$). The carboxymethyl-PEG-thiol is roughly twice as long, leaving the carboxymethyl- group exposed on the PEGylated nanoparticle surface. The carboxymethyl- group is activated for conjugation to targeting ligands (de Mol and Fischer 2010). In a common technique, repeated here, *N*-hydroxysuccinimide (NHS) is used with (*N*-(3-dimethylaminopropyl)-*N*'-ethylcarbodiimide hydrochloride) (EDC) and several buffers to link proteins, such as monoclonal antibodies, to other molecules (Reist et al. 1999; Lewis et al. 2001; de Mol and Fischer 2010; Bartczak and Kanaras 2011).

PEG, which is also one of the main coating agents used during gold nanoparticle synthesis, has been shown to induce mitochondrial fusion by reducing the mitochondria's membrane potential (Wojcieszyn 1983; Robinson et al. 1979). The

importance of fusing mitochondrial fragments in cancer progression is emphasized by studies showing that the induced fusion of fragmented mitochondria results in cell cycle arrest in lung cancer (Rehman et al. 2012). PEG-AuNPs reduce the surface potential of the fragmented mitochondria, causing fusion around the AuNPs; therefore, PEG properties may also be some of the key reasons why PEG-AuNPs have enhanced retention in neoplastic cells. This enhanced retention is corroborated by a study where PEG-AuNPs were shown to be able to reduce the surface potential of fragmented mitochondria, induce fusion, arrest cell cycle, and then induce apoptosis in chronic myeloid leukemia cells (Huang et al. 2014). Reducing the surface potentials of the fragmented mitochondria would potentially result in either a situation where the mitochondria regains its metabolic activity or depletes its capacity of supplying ATP at the quantities required by the neoplasm, which would explain PEG's dramatic ability to induce apoptosis in some colon cancer cell lines (Roy et al. 2001).

1.5. The Radiochemical/biological Properties of ^{198}Au

The radiological properties of ^{198}Au grains covered in platinum made this radioisotope popular on permanent implants for head and neck cancers, replacing the previously employed radon seeds (Hoskin and Coyle 2011). ^{198}Au is a beta emitter produced from the neutron activation of stable ^{197}Au . It has a half-life of approximately 2.7 days and decays to an isotope of mercury (Hoskin and Coyle 2011). Production of ^{198}Au can effectively be carried out utilizing a nuclear reactor and performing (n, γ) activation due

to the reasonable thermal neutron cross section of ^{197}Au ($\sigma=98.65$ b) (Goswami et al. 2016).

The radionuclide emits a 0.412 MeV gamma photon and a β_{max} of approximately 0.96 MeV. β particles are low LET radiation and generally can only travel a few micrometers to centimeters in soft tissues, which makes ^{198}Au great for targeting the tumor and reducing damage to normal, healthy tissues surrounding the tumor. The gamma radiation emitted by ^{198}Au can also be used for SPECT (not optimal due to necessary collimation of high energy gammas) or Cerenkov imaging (Black et al. 2014).

1.6. The Radiochemical/biological Properties of ^{125}I

The radiological properties of ^{125}I have facilitated its extensive use in brachytherapy for the treatment of skin, prostate, lung, and brain tumors, while also being used in certain situations for thyroid imaging (anatomic and physiologic function) and as a label in radioimmunoassays (Al Mahmoud et al. 2008; Garretson, Robertson, and Earle 1987; Gutin et al. 1984; Chen et al. 1999; Beydoun, Bucci, and Malouf 2014; Prince, Zu'bi, and Haag 1979; Corrie, Ratcliffe, and Macpherson 1981; Goddard et al. 1986; Harper et al. 1961). It has also been used with moderate success in the treatment of multiple recurrent solid tumors (Gaspar et al. 1999; Ling 1992).

The half-life of ^{125}I is 60.14 days and decays by electron capture (EC) to the excited state of ^{125}Te , which immediately emits a 35.5 keV gamma ray (Friedlander and Orr 1951).

This is followed by the emission of short-range, highly localized, low-energy conversion and Auger electrons. Conversion electrons are ejected with a maximum energy of 35 keV while the 21 typical Auger electrons produced per decay possess energies ranging from 0.07 to 30.1 keV (Silberstein 2012). Auger-electron emissions have also been found very effective for therapy and diagnostics (Stepanek, Larsson, and Weinreich 1996; Wieland et al. 1981).

The Auger effect is the primary process by which ^{125}I decays and produces cellular damage (Kassis 2004; Hofer et al. 1992; Hofer 1996). When ^{125}I decays it produces an energy deposition of approximately 106 cGy, in a 2-nm radius spherical volume surrounding the point of decay (Humm, Howell, and Rao 1995; Balagurumoorthy et al. 2012). Based on the energies of the electrons produced by ^{125}I , the electrons will approximately travel 100 nm in water and only 10 nm in gold (Vaughan 1986; Piotr et al. 2013). This range will limit the effective diameters of the AuNPs to 20 nm so that radiative emissions from ^{125}I , potentially at the core of the AuNPs, will be able to reach outside the AuNP (Dulkeith et al. 2004; Hangleiter and Hacker 1990; Zhang and Yates Jr 2010).

While Auger electrons possess relatively low-energies, their cytotoxic potential parallels that of high-LET radiation (e.g. alpha particles) when their decay occurs near DNA molecules (Bradley, Chan, and Adelstein 1975; Hofer 2000; Hofer and Hughes 1971). As a result, the electron decay of ^{125}I produces DNA double strand breaks and cluster

damage, detectable up to 70 angstroms from the decay site, making it a very potent therapeutic if near the nucleus or organelles (Martin and Haseltine 1981; Balagurumoorthy et al. 2012). Moreover, the Auger electron cascade in gold serves as a key benefit to the synthesis of ^{125}I -AuNPs, as the effect potentially enhances the radionuclide's cytotoxicity (Rahman et al. 2009). Auger cascades and the highly localized deposition of energy around the AuNPs are key features of how AuNPs influence the mitochondria and radiosensitization (Taggart et al. 2014). The potential for these ^{125}I -AuNPs to attach to lipid membranes is also a key component as the ROS produced by the Auger electrons may induce lipid peroxidation and aldehyde production, inducing senescence, which seems to be potentially corroborated by a recent study showing that the interactions of Auger electrons on the cell membranes could be cytotoxic (Paillas et al. 2016).

1.7. The Radiochemical/biological Properties of ^{211}At

Out of the many alpha emitters known only a handful of them are suitable for use in targeted, clinical therapies (^{211}At , ^{212}Bi , ^{213}Bi , ^{223}Ra , ^{225}Ac , and ^{227}Th) (Guerard, Gestin, and Brechbiel 2013). Alpha-emitters are therapeutically suitable for sites of minimal residual disease (MRD), or tiny clusters and micrometastases, because like Auger electrons alpha particles are high-LET and travel very short ranges (Imam 2001b). The radionuclide, ^{211}At , is considered an ideal candidate for alpha-emitter TRT strategies due to its relatively short half-life (7.214 h) and desirable decay chain (Zalutsky et al. 1989). Astatine-211 decays by electron capture to ^{211}Po (branching ratio = 0.582), which in turn

decays by alpha-particle emission. Following electron capture ^{211}At can alternatively decay by alpha-particle emission to ^{207}Bi . While ^{211}Po is available in the metastable state as $^{211\text{m}}\text{Po}$ from other production methods, it is not fed by ^{211}At decay due to high nuclear spin and associated low decay probability (Groppi et al. 2005). The alpha emitted from the decay of ^{211}At can travel a mean path length in tissue of approximately 55-80 μm (Imam 2001a). During decay, several x-rays in the 77-92 keV range are emitted additionally. Like I^{125} this would potentially allow *in vivo* imaging and estimation of internal dose distributions utilizing SPECT (Zalutsky and Pruszynski 2011; Turkington et al. 1993).

Compared to the other alpha-emitters, ^{211}At has the most clinically useful half-life since half-lives any shorter than a few hours prove difficult to manufacture, transport, and administer without significant decay. Unlike routinely produced radionuclides with short half-lives used in positron emission tomography (^{18}F), the processing and labeling procedures for therapeutic drugs have not been automated to the same degree. Half-lives longer than a day or two introduce issues with specific activity, labeling efficiency, and committed doses. At first, the significant energy yield of alpha-particles associated with the heavier radionuclides would seem beneficial. However, due to the multiple decays involved, it is likely that daughters will have dissociated from the targeting molecule and transported away from the tumor site, such that further emissions are ineffective (Palm et al. 2004; Guerard, Gestin, and Brechbiel 2013). This is especially true when targeting micro-metastases and cell clusters (Aurlien et al. 2000).

The biological effects of ^{211}At alpha-emissions are fundamental to its clinical efficacy. Alpha-particles like the Auger electrons produced from ^{125}I are high-LET radiation. Alpha-particles are often produced with kinetic energies 5-20 times the kinetic energies of beta particles (like those emitted by ^{198}Au). While both high-LET and low-LET radiation deposit energy via electronic interactions, the high-LET radiation will deposit a high density of ionizations surrounding the track or path it takes through a medium. The number of ionizations and distance between ionizations along a particles path plays an integral part in the amount of energy transferred per unit path length. As such the probability of creating substantial damage is substantially higher and results in more cell death per unit dose delivered. Alpha-particles have a higher LET by 2-3 orders of magnitude, resulting in much higher cytotoxicity and relative biological effectiveness (See Fig. 5) (Chen et al. 2012, Hauck et al. 1998). The higher density of ionizations results in a higher concentration of double-strand breaks and other densely manifested lesions produced by alpha-particles traversing the cell nucleus. The result is a significantly reduced cellular repair ability (Raju et al. 1991, Dadachova 2010, Chen et al. 2012).

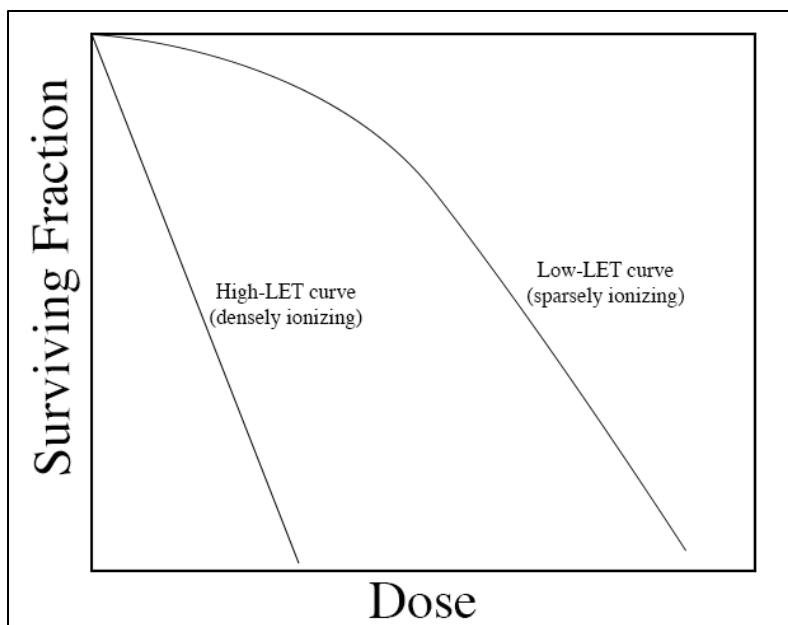


Figure 5. A relative comparison of radiobiological characteristics of various radiations as a function of absorbed dose, showing the relatively superior effectiveness of high-LET radiation, such as alpha-particles and auger electrons. X-rays and beta particles would be on the low-LET curve.

As previously mentioned, high-LET has been shown to reduce metastasis and angiogenesis in contrast to x-rays (Bruland et al. 2008; Grabham and Sharma 2013).

This is potentially again related to the ability of high-LET radiation to produce significantly more aldehydes and thus the senescence of cancer cells but other pathways still need to be investigated (Zhang et al. 2016). Using SA- β -Gal as a marker of senescence, data has shown that it takes 10 Gy X-rays (LET 4 keV/ μ m), 5 Gy Carbon (LET 80 keV/ μ m), and only 3 Gy for ^{56}Fe to begin to plateau in their ability to cause a percentage of 92-1 cells to express SA- β -Gal (Zhang et al. 2016). The effect of ^{56}Fe also plateaued with induced senescence around 100% of the cells while X-rays and carbons only plateaued around 60% of the cells going into senescence (expressing SA- β -Gal)

(Zhang et al. 2016). However, this is by external beams and potentially cannot be used to describe high-LET radiation from nanoparticles on the cell membranes or mitochondria of cancer cells, especially those that are phagocytic. Furthermore, the average number of particle traversals to result in a certain survival fraction is very dependent upon the distribution of the emission source, the concentration of the source within the cell, and the cell cycle phase (Sgouros 2008).

1.8. Combining AuNPs with Radionuclides

Besides ^{198}Au , a major impediment to the use of ^{125}I or ^{211}At in their free states, like all other isotopes of iodine or astatine, is that it has very little affinity for tissue other than the thyroid, even in the presence of a tumor (Lundh et al. 2006). Therefore, seeds and various other carriers are utilized to mitigate this issue and allow for targeting specific areas of interest. Utilizing AuNPs would potentially increase the efficacy of these radionuclides not only as a therapeutic agent in tumors of the thyroid, but for other primary and secondary neoplasms all over the body. Gold is preferred construct in the production of nanoparticles for biomedical applications as it is toxicologically inert and relatively easy to functionalize (Khan 2011). This is a property that other therapies such as seed brachytherapy does not have the ability to perform; it may target specific tumors after surgical intervention but since it does not circulate in the blood there is no means of targeting CTCs or sites of metastasis besides potential immune responses (i.e., bystander effects).

We hypothesized that radionuclide integrated AuNPs could potentially harness the targeting and delivery potential of AuNPs with the therapeutic potential of radionuclides. The potential of utilizing PEGylated radionuclide-AuNPs is supported by the observation of the cellular ultrastructure obtained from transmission electron microscopy (TEM) images that reveal the internalization of AuNPs, which were distributed throughout cytoplasmic vacuoles and damaged mitochondria, which subsequently accumulated in areas surrounding the nuclear membrane (Huang et al. 2014). Wang et al. observed the accumulation of gold nanorods in the mitochondria of tumor cells while normal cells with normal mitochondria were spared (Wang, Liu, et al. 2011). In addition, Hainfeld et al. observed a 19:1 *in-vivo* accumulation of intravenously injected AuNPs in glioma-tumor bearing mice versus normal brain tissue (Hainfeld et al. 2013). AuNPs are now also being routinely used to target the mitochondria (Wang, Liu, et al. 2011; Kirkby and Ghasroddashti 2015; Karatas et al. 2009), and if concentrations are high enough can provide favorable characteristics as a contrast agent in CT imaging at least for one time use (Hainfeld et al. 2006). Further studies would need to be performed to investigate complications with repeated administration. As an example, the combination of ^{125}I with AuNPs would give us the potential to increase targeting of subcellular components with Auger electrons, a key component of ^{125}I radiotoxicity (Narra et al. 1992). This includes targeting the nuclear DNA of the cell and even the mitochondrial DNA, increasing the treatment efficacy. Even interactions with the lipids of the cellular membranes, causing aldehyde production via lipid peroxidation, may increase the incidence of radiation-induced senescence (Flor, Doshi, and Kron 2016). This would be a benefit of using high-

LET radiation like the Auger electrons and alpha particles emitted from ^{125}I and ^{211}At , respectively. These are all items that seed brachytherapy does not have the potential to accomplish, seeing how ^{125}I seeds are encased in titanium, which block the Auger electron emissions.

1.9. Synthesis of $^{125}\text{I}/^{211}\text{At}$ -AuNPs

Even though the combination of these two modalities is intriguing, the synthesis of gold nanoparticles (AuNPs) containing halides (Iodide or Astatide) has been arduous. My research focused on ^{125}I -AuNPs synthesis. Routinely, it has been found that the addition of iodine during nanoparticle synthesis results in the aggregation of gold nanoparticles, mainly due to a destabilization of the surface potentials of partially formed nanoparticles via displacement of the stabilizing citrate groups (Cheng, Dong, and Wang 2003; Daniel and Astruc 2004). However, after synthesis, AuNPs have been coated with ^{125}I , which was added simultaneously with PEGylating “capping” agents. Capping the iodine coated AuNPs with PEGylating agents was found to provide effective enhancement of x-ray/CT imaging while also increasing the biological half-life of the radionuclide in target tissues (Kim et al. 2012).

Gold and iodine atoms have very interesting interactions, there is a process called chemisorption, referring to the way in which halide ions and organic compounds absorb onto the surfaces of transition-metals through mutual interactions (Pyykkö 2005). Within this dissertation, iodine was added during synthesis of AuNPs, at reflux, to generate

polyiodides or polyiodines, which are hypervalent and show exceptional electrical conductivity (potentially contributing to free radical production) integrated into the structure of the AuNP.

Polyiodides are a fascinating concept in structural chemistry, with established structural characterizations ranging from I_2^- to I_{29}^{3-} (Svensson and Kloo 2003). Even though the anionic forms are the most established and researched, the relatively stable cationic forms (polyiodines) are possible as well (Merryman, Corbett, and Edwards 1975). To our synthesis, the cationic formation was the most relevant because they are already known to readily occur in metal chloride solutions in the presence of reducing agents (Merryman, Corbett, and Edwards 1975). The nature of polyiodide and polyiodine bonding is not explained by conventional covalent bonding models and have thus been the object of much experimental and theoretical speculation (Svensson and Kloo 2003). Neutral iodine and gold have n-1 valence electron configuration while each of their ionic forms have closed valence shells (Svensson and Kloo 2003).

The most important correlation between the gold and iodine is that their electronegativities are almost identical, gold having a 2.4, while iodine has a 2.5 (Svensson and Kloo 2003). As such, iodine has been demonstrated to exhibit metal-like behavior (Tang et al. 2014). Additionally, considerable evidence has shown gold to behave chemically like halogens (Greenwood and Earnshaw 1984; Svensson and Kloo 2003). As a result, many gold-iodine complexes have almost identical bond angles along

with very similar bond lengths to those of polyiodides: (i.e., AuI_4^- and I_5^-) (Svensson and Kloo 2003). This also means that the I-I interactions in binary gold are most appropriately described as being analogous to those observed in polyiodides and polyiodines (Svensson and Kloo 2003). Because of this, it was found reasonable to hypothesize that polyiodides and polyiodines can be incorporated directly into the structure of gold nanoparticles. If successful, this would lead to the synthesis of highly cytotoxic ^{125}I -AuNPs, readily capable of being functionalized using PEG and tumor-targeting biomolecules (e.g., cell-penetrating peptides) (Floren, Mager, and Langel 2011; Hallbrink et al. 2001; Zorko and Langel 2005). Therefore, below we describe our early experimental results in the synthesis of ^{125}I integrated gold nanoparticles that are for now PEGylated, but due to stability during synthesis, can potentially be functionalized with any other coating agent of AuNPs. A similar procedure was performed for ^{211}At as well.

1.10. Synthesis of Fluorescent AuNPs Probes

The highly sensitive nature of fluorescent probes for assays and detection techniques makes them among the most popular biological option for many researchers. However, to combine fluorescent probes with AuNPs is a rather arduous task. This is because AuNPs show the highest quenching (decrease in fluorescence intensity) ability of any compound tested, up to 99% (Swierczewska, Lee, and Chen 2011). Even for AuNPs of approximately 1 nm radius there is significant fluorescence quenching of lissamine dye molecules, not only because of increases in the nonradiative decay rate but reductions in the dyes radiative decay rate as well (Dulkeith et al. 2002). Similar probes have shown

that decreases in the excited state lifetime and fluorescence quantum yield observed upon binding to AuNPs could be traced back to the previously mentioned decrease in nonradiative rate or in other word the increase in nonradiative deactivation rate (Cannone et al. 2006). However, the degree of quenching appears to be length dependent and as such fluorescent-PEG-thiol compounds may be advantageous. However, there is a caveat to using these nanoparticles with long-chain PEGs to image cancer cells, the longer the PEG chain the lower the uptake (Cruje and Chithrani 2014). Therefore, a combination of 2kDa methyl-PEG-thiol and 5kDa Cy5.5-PEG-thiol was used together to prevent the Cy5.5 from getting too close to the AuNPs surface to entirely quench the fluorescent signal.

1.11. Delivery of Theranostics to the Lungs

A main advantage of utilizing these radionuclides (I-125, Au-198, and As-211) is that they are theranostics; capable of being used therapeutically and diagnostically (imaging). *In vivo* imaging is an important tool for preclinical studies with particular interest on lung function and disease. This is because lung cancer is the leading cause of cancer-related deaths for both men and women throughout the developed world (Purandare and Rangarajan 2015). The widespread availability of multimodal animal imaging systems and the rapid improvement of diagnostic contrast agents available have allowed researchers to noninvasively study lung function and pulmonary disorders (van der Schee et al. 2015). There are several imaging modalities used in molecular imaging such as planar radiography, computerized tomography (CT), single photon emission

tomography (SPECT), positron emission tomography (PET/CT), magnetic resonance imaging (MRI), Cherenkov luminescence imaging (CLI), PET/MRI, and bioluminescence (Auletta et al. 2017; Kiessling et al. 2014; Martinez-Rodriguez and Banzo 2017). Each one of these imaging modalities has their own set of advantages and limitations. Using the above imaging modalities makes it possible to diagnose, track, and quantify biological processes over time. A combination of modalities also offers great insight into tumor progression and treatment efficacy. Bioluminescence, fluorescence, planar x-ray, CT, MRI, and nuclear imaging modalities (PET and SPECT) for the study of lung function and pulmonary disorders have been employed in the preclinical setting (Shaw, Kirsch, and Jacks 2005). However, in humans the diagnosis and therapy of lung diseases continue to be problematic (Garrastazu Pereira et al. 2016; Hussain 2016; Anchordoquy et al. 2017; Landesman-Milo, Ramishetti, and Peer 2015; Shete et al. 2014). Even with tremendous effort to treat, the overall 5-year survival for all stages of lung cancer are dismally low at only 15% because most patients often present at advanced stages when no curative treatment is still an option (Mountain 1997). The direct delivery of drugs to the lungs is a difficult task that requires the merging of engineering principles in aerosol sciences and molecular imaging, including the sustained drug release after inhalation (Iyer, Hsia, and Nguyen 2015; Muralidharan et al. 2015; Mortensen and Hickey 2014; Loira-Pastoriza, Todoroff, and Vanbever 2014; Darquenne et al. 2016).

1.12. The Merit of Nebulizers in Drug Delivery to the Lungs and Therapy

The treatment of lung diseases has drastically improved alongside nebulizer development and research enabling the production of quasi-monodisperse aerosols capable of penetrating the deepest regions of the lung (Darquenne et al. 2016). However, due to inconsistent reporting and nebulizer variations many studies have been irreproducible. Therefore, the standardization of these systems, including the devices and techniques or procedures could provide researchers the capacity to reproduce studies and one day duplicate the consistent delivery of aerosols to patients (Jacob, O'Driscoll, and Dennis 2003). Furthermore, the advent of active biological nanoparticles as drugs is spurring the research to characterize aerosol delivery, pharmacokinetics, pharmacodynamics, and overall safety (Mitchell, Suggett, and Nagel 2016; Dyawanapelly, Kumar, and Chourasia 2017). This includes not only radionuclide-integrated metal nanoparticles but also chemotherapeutics modified into nanoparticles. These nanoparticle-based drug nebulization studies will require preclinical animal models to assess the safety and efficacy of these nanoparticles under FDA guidelines. The FDA maintains a product-focused, science-based regulatory policy and has regulated nanotechnology-based products under pre-existing statutory authorities (Food and Drug Administration 2014). The current framework for safety assessment could be considered sufficiently robust for this application and flexible enough to be appropriate for a variety of materials such as nanomaterials. As an example, CytImmune Sciences, Inc produced Aurimmune (CYT-6091), a colloidal gold approved for Phase II Preclinical studies for solid tumors utilizing a TNF- α targeting mechanism (Libutti et al. 2010;

Paciotti et al. 2004). The developed nebulization system could be used to help develop translational physiologically based pharmacokinetic models of radiolabeled, functionalized gold nanoparticle aerosols inhaled by animal models of disease. This will in turn help develop therapeutic strategies for those aerosols in humans.

1.13. The Vibrating Mesh Atomizer

The nebulizer system developed in this dissertation consists of an annular piezoelectric element or crystal that surrounds/contacts a mesh. This mesh consists of thousands of tiny laser-drilled holes, each possessing a conical structure. To bias nebulization in one direction, the larger cross-section of these conical structures all face the fluidic drug reservoir. As the piezoelectric element activates, it vibrates the mesh at high frequencies (typically 1-3 MHz). This deforms the fluid supply and thus ejects a population of fluid particles on the opposite side of where the fluid reservoir was (Watts, McConville, and Williams 2008). This provides the name of these devices, vibrating mesh nebulizers, versus jet nebulizers. Mesh nebulizers have an almost silent operation, high output efficiency, and have minimal residual volume (most effective at delivering aerosol throughout lungs) (Ari 2014). Furthermore, mesh nebulizers can nebulize low drug volumes. The size of the pores or laser drilled holes, the reservoir, the aerosol chamber, and the output rate of mesh nebulizers, can be adjusted for different drugs to optimize aerosol drug delivery to patients. Although human studies with mesh nebulizers are limited, in vitro studies demonstrated approximately 2-3 times higher lung deposition with mesh nebulizers when compared to jet nebulizers (Farkhani et al. 2014; Lluís and

Cosma 2010; Ari and Fink 2012; Rau, Ari, and Restrepo 2004). It is important to note that aerosol output and the actual inhaled fraction will be largely influenced by drug formulations. This is because the performance of these vibrating mesh nebulizers could be hindered by suspensions with a high surface tension or those that could crystallize upon drying as reports exist regarding the blockage of the mesh perforations (Dhand 2002; Ari 2014). This was particularly true for our studies as we found citrate encapsulated gold nanoparticles accumulated or aggregated in the nebulizer while PEGylated gold nanoparticles did not. In fact, the larger the ratio of PEG to AuNPs utilized for the experiment the faster the nanoparticles were aerosolized thus it was significantly reducing the surface tension of the nanoparticles.

1.14. Aerosol Characterization

Several characterization techniques and attributes exist for a thorough depiction of an aerosol and its predicted behavior. One of the key characteristics is the aerodynamic diameter. It is defined as the equivalent diameter of a unit density having the same settling velocity due to gravity as the particle under scrutiny or interest of whatever shape and density. It is advantageous to formulate these attributes so that one can account for the particle aspect ratio, potentially shape, and size of an individual particle. Since aerosols are the sum combination of a large population of particles, the population can be described in multiple ways such as number median aerodynamic diameter (NMAD), volume median aerodynamic diameter (VMAD), mass median aerodynamic diameter (MMAD), and surface median aerodynamic diameter (SMAD). These values

are also often provided with a geometric standard deviation, which will allow you to correlate between each one of them using the Hatch and Choate Relation.

1.15. Comparison of Human and Mouse Lungs

The route of entry for internalization of airborne nanoparticles is most significantly inhalation (Yang, Peters, and Williams 2008). In mammals, the respiratory system is typically partitioned as the extra thoracic/nasopharyngeal region (nose, mouth, pharynx, larynx), tracheobronchial region (trachea to terminal bronchioles: main bronchus, lobar bronchus, segmental bronchus, sub-segmental bronchus, conducting bronchiole), and the pulmonary/alveolar region (respiratory bronchiole, alveolar duct, alveolar sac, alveolus). Several trends can be observed as you go deeper into the lungs such as an increase in branching, the total cross-sectional area, and the residence time in the airway. In other words, the relationship exists that as the length/diameter decreases and branching number increases, there is a reduction in velocity and thus an increase in residence time. These trends can be used to distinctly characterize each airway in the lungs, thus aerosol particle deposition and subsequent deposition mechanisms should be considered distinct per location in the lung.

There are many important considerations regarding the differences between human and murine lungs (Mendez, Gookin, and Phalen 2010; Irvin and Bates 2003; Bennett and Tenney 1982). For one thing, mice are obligate nose breathers and as such the contribution of the upper airways must be taken into consideration with un restrained

mice when doing measurements of respiratory function. Mice have a total lung capacity (TLC) of approximately 1 ml while humans are roughly around 6,000 ml (Irvin and Bates 2003). Both humans and mice have 5 lobes distributed between both lungs however the left lung in mice is composed of a single lobe (see Fig 6). 18% of the mouse lungs is occupied by parenchyma while only 12% of the human lungs is occupied by parenchyma (Irvin and Bates 2003). The mouse lung alveoli are significantly smaller as well with a mean linear intercept of 80 μm compared to that of 210 μm in humans (Irvin and Bates 2003). The blood-gas barrier thickness, which would potentially have important implications in nanoparticle translocation, gas exchange, and parenchymal lung mechanics, is 0.32 μm in mice and 0.62 μm in humans (Irvin and Bates 2003). The number of respiratory bronchioles and airway generations are significantly fewer as well with only 13–17 compared to the more numerous 17–21 generations observed in a human lung (Irvin and Bates 2003).

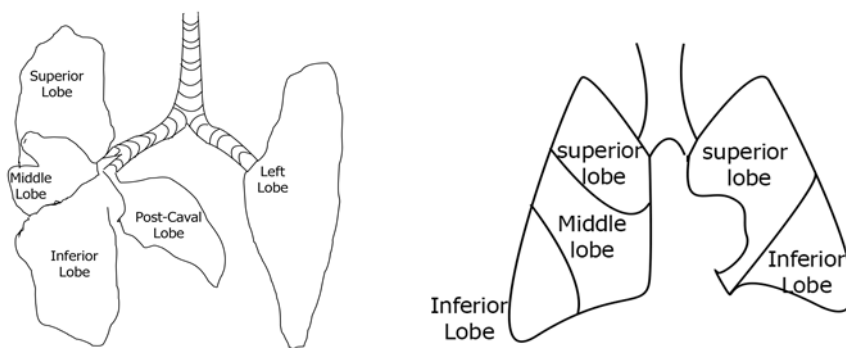


Figure 6. Comparison of the human (right) and mice (left) lung.

The lungs of each species also differ in symmetry: a monopodial branching pattern for mice in contrast to a dichotomous branching pattern for humans. Mice also possess a relatively large airway lumen compared to humans (Gomes and Bates 2002). These geometrical differences and some physiological differences will affect the deposition of aerosols in the lungs of each species. In addition to the existence of geometrical differences between human and murine lungs, there are also distinct differences in the pathology, physiology, and histology. The symmetry and size of the branching in the lungs account for most of the geometrical differences. The relatively large size of the lumen in mice is likely in place to accommodate air resistivity induced by the rapid respiratory rate (250 – 350 bpm) required to maintain body temperature (Bennett and Tenney 1982). The distribution of submucosal glands is different than that seen in humans, present only in the trachea (Innes and Dorin 2001). Lastly, mice tend to have significantly higher numbers of Clara cells, a morphologically distinct population of cells that have been identified for their importance in anatomical fortification against environmental exposures (Reynolds and Malkinson 2010; Irvin and Bates 2003).

The more complex pathological, physiological, and histological differences will affect the nature of tumor formation and response to aerosolized nanoparticles in both species, which may be an important consideration for therapeutic treatment. With xenografting, genetic lesions of human lung cancer have been introduced into murine pulmonary tissue to yield lung tumors with similar characteristics to those found in humans. In addition, transgenic models have allowed for the assessment of oncogenes in tumor origination

and development by focusing their expression in a subset of lung epithelial cells (Meuwissen and Berns 2005; Shaw, Kirsch, and Jacks 2005). The superiority of animal models with grafts of tumor material (xenogeneic or syngeneic) over spontaneous tumor models is debatable; however, the use of these models has provided some significant advancements in preclinical studies, especially those of childhood cancer treatments, despite the lack of reliability or prediction of effect in clinical cancers (Kellar, Egan, and Morris 2015; Morton and Houghton 2007). Murine models altogether possess many advantages to other models such as human genome similarity, proven efficacy in the validation of drug targets and dosage schemes, cost-effectiveness and reproducibility, and large-scale phenotyping (Vandamme 2014).

1.16. Particle Deposition Mechanisms

The treatment efficacy of aerosolized drugs is dependent on the dose deposited beyond the oropharyngeal region at the region of interest or targeted tissue, as well as the distribution of the drug in the lungs (uniform or not) (Fernandez Tena and Casan Clara 2012). The deposition of particles in the small airways gets maximum attention from pharmaceutical companies (Fernandez Tena and Casan Clara 2012). Deposition of aerosols in the airways can occur via inertial impaction, gravitational sedimentation, or Brownian motion (diffusion) (See Fig. 7) (Dhanani et al. 2016). The modality of deposition is dependent upon many factors including size of the particles, speed, and turbulence. For example, at the alveolar level the minimal air velocity means there will

be no deposition by impaction and otherwise deposition will occur by sedimentation and diffusion (Lourenço 1982).

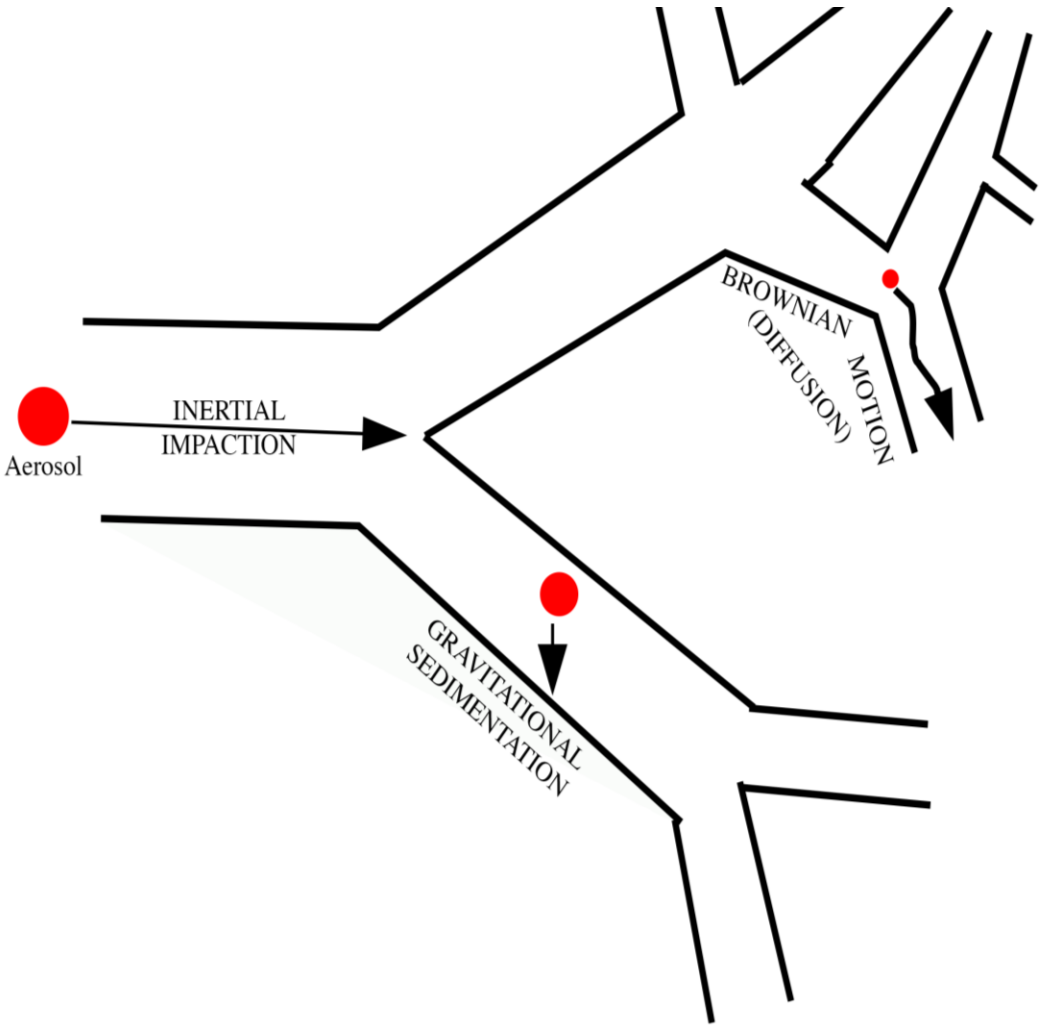


Figure 7. Mechanisms of particle deposition in the airways. Depending on the diameter and velocity of the particle the mechanisms are inertial impaction, gravitational sedimentation, and diffusion.

1.17. Clearance Mechanisms

Once particles are deposited in the lungs, the presence of particles results in two pathways, retention and clearance. Retention is the tendency of particles to remain in pulmonary airways. Retention is dependent upon the physiochemical properties of the particles in the aerosol, the regional deposition of the particles in the lungs, and even the clearance mechanism involved. This is the same context as retention in the tumor, which is why clearance of nanoparticles may be a good thing, to prevent damage of normal lung tissues if retention of the nanoparticles is biased toward the tumor. Contrary to retention, clearance is the anatomical tendency to remove undesirable particles from the lungs of which there are multiple mechanisms. The efficient elimination of soluble and insoluble particulates inhaled and deposited in the respiratory tract is necessary to keep the mucosal surfaces clean and functionally intact (Isawa et al. 1984). Clearance mechanisms are important to mention because it may explain the translocation behavior of the nanoparticles following the aerosol deposition in the lungs.

1.17.1. Clearance via the Mucociliary Escalator

The first line of defense for the respiratory system and the dominant clearance mechanism of the tracheobronchial region or the conducting zone is mucociliary clearance (Isawa 1994). The mucociliary escalator, as this clearance mechanism is termed, consists of continuous, rhythmic coordinated beating of cilia on the bronchial wall epithelium moving two fluid layers, periciliary fluid and a mucus “gel” layer towards the larynx where it can be swallowed (Oberdörster 1988). There are close to 200

fully functional and developed cilia grow on each airway epithelial surface from the trachea down to the terminal bronchioles (Isawa 1994). These cilia are roughly 6-7 μm with a 1- μm diameter and coordinated their rate of motion at 1000 beats per minute or 10-15 Hz (Isawa 1994; Joseph, Puttaswamy, and Krovvidi 2013). This motion transports contaminant particles upon viscous capture sustained by the mucus composed of the gel and periciliary layers produced by goblet cells that lines the tracheobronchial region. The duration of obligatory removal of particles using this clearance mechanism is on the order of hours (2-3), even less if the particles are administered at a low dosage and prove to be irritants, and possibly more if administered in high dosages.

1.17.2. Pulmonary Alveolar Macrophages

In the alveolar lung regions, the clearance mechanism of particulates has been shown to involve pulmonary alveolar macrophages (PAMs). PAMs have also been shown engulf particles and translocate them to the mucociliary escalator, lymphatic or venous/circulatory system for removal (Joseph, Puttaswamy, and Krovvidi 2013). The destination of translocation is determined by the solubility of captured particles. Soluble substances can permeate the alveolar membrane where they are translocated via the venous system. It is hypothesized that nanoparticles will qualify as soluble particle and will thus appear in the venous system. For one such reason, PAMs have shown the capability to increase dissolution of metal oxides, potentially due to the low pH of their phagolysosomes (Lundborg, Lind, and Camner 1984). Insoluble substances are likely to

be transferred to the lymphatic system and the duration of obligatory removal of these particles is on the order of months to years.

1.17.3. Particle Translocation

20 nm iridium nanoparticles were reported to translocate from the lung surface into pulmonary tissue such that they could be subject to lymphatic drainage and venous incidence resulting in migration to secondary organs. This is because phagocytes may also transport the particles from the lungs to the lymph nodes for presentation to T lymphocytes (Lehnert, Valdez, and Stewart 1986). This would explain why healthy patients treated with conjugated-PEG agents also have been shown to potentially form antibodies against PEG as well (Garay et al. 2012). Even though relatively small amounts, some particulate translocation resulting in presence in the vein was also reported in studies using TiO₂ nanoparticles (Semmler et al. 2004; Semmler-Behnke et al. 2007). However, lymphatic drainage was not assessed during these studies (Semmler et al. 2004; Semmler-Behnke et al. 2007). While 10% of the iridium nanoparticles administered were shown to translocate across the secondary organs, skeleton, and soft tissue (Semmler-Behnke et al. 2007)), it could be argued that delivery technique and how the nanoparticles were functionalized would affect this translocation significantly. The functionalization technique, if any, used for the iridium particles is not known (Geiser and Kreyling 2010). Translocation while potentially important in drug delivery studies is not necessary when imaging the lung tissues. The delivery method proposed here utilizes suspended AuNPs in a fluid solution that is the delivery agent to be

aerosolized.

1.18. Models

Several models based on experimental results have been developed to model deposition. These include the Human Respiratory Tract Model from the International Commission on Radiological Protection (ICRP) and the National Council on Radiation Protection and Measurement (NCRP). These models are typically very similar in their deposition curves except for discrepancies found in the ultrafine particle range $< 1\text{-}2\text{ }\mu\text{m}$ [63]. A java-based application known as Multiple-Path Particle Dosimetry Model (MPPD) performs calculations to yield an extensive amount of information regarding deposition influenced by parameters discussed previously using the human respiratory tract models (HRTM) as well as characterized murine models [64].

To determine the efficacy of these nano-therapies, a well-characterized human orthotopic model of osteosarcoma lung metastasis has been developed to carry out *in vivo* evaluations with a focus on evaluating the mechanisms by which the nanoparticles improve the efficacy of cancer therapy as compared with the current formulations used clinically. Due to the complexity of cancer metastasis and unknown biodistribution and pharmacokinetics of these nanotherapeutics when dosed to the lung, an *in vivo* model is necessary to explore the processes that affect chemotherapeutic efficacy. Mice are the smallest generally accepted model for cancer biology that can be infected with human cancer cells and demonstrate metastases.

NOD/SCID IL-2-Receptor-gamma deficient $-/-$ (NSG) mice will be used for this study, which are among the most immunodeficient mice available. Their severe combined immune deficiency mutation (SCID) and IL-2 receptor gamma chain deficiency yields a high success rate for xenograft implantation and metastasis. These animals have a retail price of approximately \$100 and often are subject to shortages that severely limit experimental planning. Thus, to reduce costs overall and to retain better control over animal availability, all animals were obtained from mouse colonies already established by Dr. Wooley at TAMU, which produced up to 40 mice per month, including frequent “refreshing” of the colony with new, young breeders, since NSG mice are less fecund than conventional animals. Every effort was made to limit the breeding of experimental animals only to those needed for the study.

CHAPTER II

MATERIALS AND METHODS

2.1. Production of Radioactive ^{198}Au Gold Nanoparticles

Production of ^{198}Au was carried out at the Texas A&M University Nuclear Science Center (NSC) in collaboration with Zaher Hamoui (Hamoui 2015). Briefly, 10 mg of high-purity gold (III) chloride trihydrate (HAuCl_4) (Sigma Aldrich, St. Louis, Mo) in solid form was irradiated at the NSC for a minimum period of 4 h. Neutron activation of ^{197}Au resulted in the production of ^{198}Au *via* the reaction $^{197}\text{Au}(n,\gamma)^{198}\text{Au}$. The thermal neutron cross-section is approximately 4916 barns. The activated solid sample was transported to our labs using a compact shipment system for radioactive material (Model 001-724, Biodex Medical Systems, Shirley, New York). Upon receipt of the sample, a high-purity germanium (HPGe) detector (Canberra Industries, Meridian, CT) was used to assess the purity of ^{198}Au and the presence of potential radioactive impurities or contaminants. A dose calibrator (ATOMLAB 500 Dose Calibrator, Biodex Medical Systems, Shirley, NY) was used to assess the net activity of the radioactive sample. The activity levels of ^{198}Au received varied considerably, depending on irradiation time and elapsed time for delivery. The radionuclide ^{198}Au decays via beta particle emission and has a physical half-life of 2.6947 days with an average beta particle energy is 0.311 MeV.

Radioactive AuNPs were produced using the Turkevich method (Kimling et al. 2006) as described by Kumar, *et. al.* (Kumar, Aaron, and Sokolov 2008) and Frens *et. al.* (Frens 1973). Briefly, 1 ml of a 12.7 mM ^{198}Au chloroauric acid solution was added to 49 ml of deionized ultra-filtered (DIUF) H_2O in a clean 100 ml three-neck round-bottom flask fitted with a stir bar and reflux condenser (See Fig. 8). To this solution under reflux was added 0.94 ml of 38.8 mM trisodium citrate. The solution turned cherry red in *ca.* 2-3 min, after which refluxing was continued for 10 min, producing 50 ml of highly spherical, mono-disperse gold nanoparticles between 15 to 30 nm in diameter, depending on chloroauric acid concentration. Particles were characterized by TEM and UV-Vis spectroscopy. Alteration of the nanoparticle size can be performed by manipulating the timing of trisodium citrate addition to the flask (Frens 1973). Nanoparticles were found to be stable for several months if stored at 4°C . The total activity per unit volume ($\mu\text{Ci}/\text{ml}$) was estimated using a dose calibrator (AtomLab 500, Biodex, Inc.).

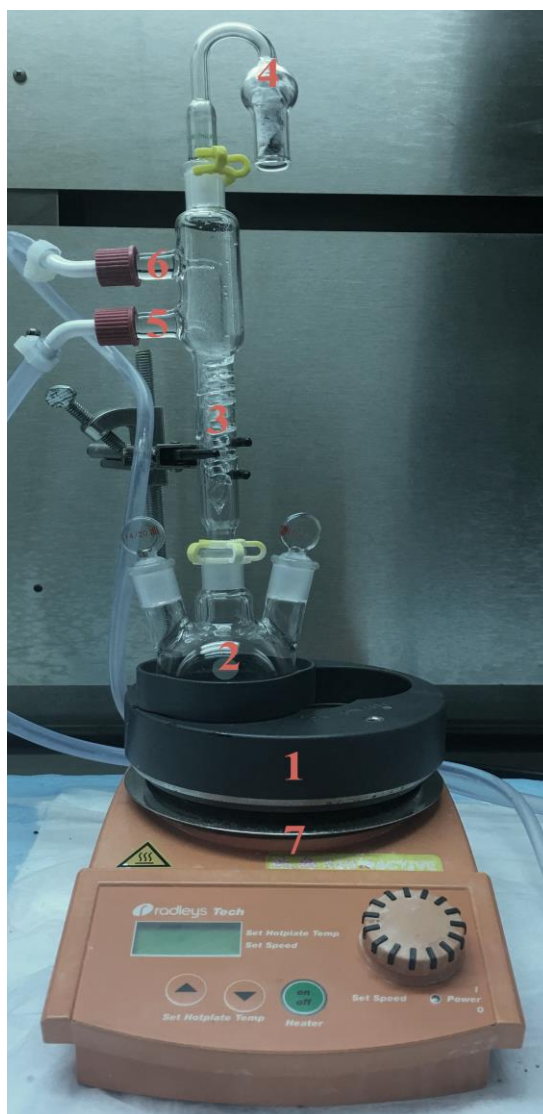


Figure 8. Experimental apparatus to produce gold nanoparticles: (1) heat block with round bottom insert for heat transfer purposes; (2) 100 ml round bottom flask (3-neck), containing stir bar and reactants; (3) reflux column; (4) charcoal in cotton to act as a filter; (5) cold water inlet for reflux column; (6) reflux water outlet; (7) hot plate.

Functionalization of the AuNPs was also carried out. PEG modification, or PEGylation, is one of the most commonly used surface modification methods for gold nanoparticles.

The PEG coating decreases the reduction of protein absorption and increases the stability of the AuNPs. It is important to note that PEGylation and/or protein conjugation to the

nanoparticles will cause a 3-5 nm red shift in the UV VIS spectra as the added layer of material affects the surface refractive properties (Kumar, Aaron, and Sokolov 2008). The PEG modification was carried out in our laboratory using the methods described by Cytodiagnostic (Tech Note #105). Briefly, 1 ml (0.25 nmol) of AuNPs coated with citrate (1.5×10^{14} particles/mL) was PEGylated by simple ligand exchange of citrate with a 1000-fold molar excess of carboxy-PEG5000-thiol (CM-PEG500-SH, Laysan Bio) in deionized water for 15 min. PEGylated carboxyl-terminal AuNPs (198AuNP-PEG-COOH) were collected by centrifugal filtration at 5000 x g using 10 kDa MWCO Amicon Ultra-15 centrifugal filter units (Millipore) to remove excess unreacted PEG reagents, repeatedly washed with deionized water, and reconstituted in 0.5 ml MES buffer for addition of the immunoconjugate.

Functionalization peptide of PEGylated radioactive gold nanoparticles with the cell penetrating was carried out using the method described by Cytodiagnostic. Briefly, 30 mg of 1-Ethyl-3-carbodiimide hydrochloride (EDC) (Sigma, Cat# E1769) and 36 mg of N-hydroxysulfosuccinimide (Sufo-NHS) (Sigma, Cat# 56485) was mixed in 1 ml of MES buffer (Sigma, Cat# M5287) to form the EDC/NHS solution. Conde *et al.*, has described in detail the above functionalization method. The advantage of EDC coupling is that it increases water solubility of PEG-AuNPs, which allows for direct bio-conjugation without the prior use of an organic solvent to increase the stability of an active ester, such as N-hydroxysulfoxuccinimide (sulfo-NHS). The addition of sulfo-NHS also stabilizes the amine-reactive intermediate by converting it to an amine-

reactive sulfo-NHS ester; therefore, it increases the efficiency of EDC-mediated coupling reactions (Conde et al. 2012). We first prepared a fresh EDC/NHS mix solution, as described before, in MES buffer at a concentration of 30 mg/mL and 36 mg/mL, respectively. We then used 10- μ L of PEGylated radioactive AuNPs and mixed with 10 μ L of the EDC/NHS solution. The new solution was then incubated for 30 minutes at room temperature. One milliliter of PBS Tween (PBST) was added and vortexed subsequently. The solution was centrifuged at 6,500 g for 30 minutes and supernatant removed. 10 μ l of human immunodeficiency virus type 1 trans-activating regulatory protein (HIV-1 Tat) (1 mg/mL in 1X PBS) was then added and solution sonicated in a water bath for 10 seconds. The mixture was then incubated for 2 to 4 hours at room temperature with continuous mixing. 1 ml of PBST was added and again vortexed thoroughly. Subsequently, the solution was spun down by centrifugation at 3,500 g for 30 minutes and supernatant removed. 50 μ l PBS with 1% BSA was then added, followed by storage at 4 degrees until ready to use. Once radioactive and non-radioactive AuNP were functionalized with HIV-1 Tat, they were ready to be used as later described with the real-time cell analyzer (RTCA) system.

2.2. Production of Radioactive ^{125}I Integrated Gold Nanoparticles

In addition to previous materials, mPEG-Thiol 2000 MW was purchased from Lysan Bio (Arab, AL, USA). Milli-Q water (18.2 M Ω) was used in all preparations. 2 mCi of Sodium Iodide-125 (Na^{125}I) in 1×10^{-5} M NaOH solution, no carrier added, was obtained from Perkin Elmer Life Science, Inc. (Boston, MA, USA).

A stock preparation of gold solution was made by adding 55.5 mg of HAuCl_4 to 500 ml of deionized water. A sodium citrate solution was made by adding 1.012 g of sodium citrate to 100 ml of deionized water (1% solution). The citric acid solution was diluted to 1×10^{-5} M by taking 1 ml of initial solution and adding 9 ml of deionized water, and repeating the process four times. This technique was also used for the dilution of mPEG to 1×10^{-5} M as well.

For synthesis of I-125 integrated AuNPs, 10 ml of the stock HAuCl_4 solution was heated for approximately 10 minutes until reflux (visible boiling) while under continuous, vigorous stirring using a hot plate, aluminum reaction block, 3-neck round bottom flask, and reflux condenser. Then, the addition of 0.35 ml of the 1% sodium citrate solution was added to the mixture. Approximately 50 seconds after the addition of sodium citrate, 10 μl of 1×10^{-5} M citric acid mixed with 10 μl of Na^{125}I in 1×10^{-5} M NaOH , which equated to 100 μCi in the first obtained batch and 302 μCi the second obtained batch), was added to forming AuNPs. The activity of the ^{125}I -AuNPs was measured using a dose calibrator (Biodex Medical Systems, NY). Once the ^{125}I -AuNPs were PEGylated by addition of 50 μl 1×10^{-5} M mPEG-Thiol, they were shaken for 20 minutes using a vortex mixer. Then, three Eppendorf® centrifuge tubes containing nanopore filters, Nanosep 10k Omega (Pall Corporation, Ann Arbor, MI) were filled with approximately 0.5 ml of the final product. Samples containing 0.5 ml of the gold nanoparticle solution were centrifuged at 1400 rpm for 10 minutes. Filters containing nanoparticles were separated

from the solvent, washed, and counted for radioactivity using a proportional counter. The solvent was also counted for radioactivity separately.

2.3. Non-radioactive Iodine Nanoparticle Synthesis

To characterize the nanoparticles and perform TEM Imaging, non-radioactive iodine nanoparticles (Au-I-NPs) were made as well. First, 10 ml of the stock Au (III) chloride tri-hydrate solution was heated for approximately 10 minutes until reflux (visible boiling) while under continuous, vigorous stirring using a hot plate, aluminum reaction block, 3-neck round bottom flask, and reflux condenser. Then, 0.35 ml of the 1% sodium citrate solution was added to the mixture. This was followed by 0.25 ml of 1×10^{-5} M non-radioactive sodium iodine solution in 1×10^{-5} M NaOH solution and 0.25 ml 1×10^{-5} M citric acid as a homogenous mixture, at various independent time intervals ranging from 0 to 180 seconds each time the gold nanoparticles with iodine were synthesized. The mixture was refluxed further for 5 minutes and allowed to cool off the hotplate.

A mimetic of the ^{125}I using the nonradioactive nanoparticles was also used for the animal imaging. First, 10 ml of the stock Au (III) chloride tri-hydrate solution was heated for approximately 10 minutes until reflux (visible boiling) while under continuous, vigorous stirring using a hot plate, aluminum reaction block, 3-neck round bottom flask, and reflux condenser. Then, 0.35 ml of the 1% sodium citrate solution was added to the mixture. This was followed by 0.25 ml of 1×10^{-5} M non-radioactive sodium iodine solution in 1×10^{-5} M NaOH solution and 0.25 ml 1×10^{-5} M citric acid as a homogenous

mixture at 50 seconds. For animal imaging the non-PEGylated gold nanoparticles were then centrifuged, the supernatant removed, and the precipitate resuspended in 100 μ l of 1×10^{-5} M mPEG-Thiol and 400 μ l of 1×10^{-5} M Cy5.5-PEG-Thiol (Biochempeg Scientific INC., Watertown, MA, USA). They were then shaken for 20 minutes using a vortex mixer.

2.4. Production of Radioactive ^{211}At Integrated Gold Nanoparticles

For the final radionuclide integrated AuNP synthesis, ^{211}At from Michael Martin's Ph.D. experiment was then obtained and incorporated into colloidal gold nanoparticles.

Initially, all glassware was washed with Aqua Regia (3 parts 5 N HCl, 1 part 6 N HNO₃) and then rinsed with twice-deionized water. Then, 10 ml of deionized water was brought to a boil in round bottom flask, which was followed by the addition of 0.2 ml of 12.7 mM HAuCl₄. After recovery from a capillary tube by using a 38.8 mM sodium tricitrate solution, an aliquot of 35 μ Ci (approximately 100 μ l after decay) was prepared. This solution was added in the nanoparticle formation process described by the ^{125}I experiment, however sodium citrate and the ^{211}At were added together without the gap in time between the two. Following production, the nanoparticles were centrifuged at 11,540 G for 10 minutes. The supernatant was removed, and the nanoparticles were re-suspended and washed with fresh sodium citrate. The sample was spun again, and the nanoparticles were re-suspended in 100 μ l of sodium citrate.

2.5. Nanoparticle Characterization

The nanoparticles produced for this research were compared with commercially available standards obtained from CytoDiagnostics, Inc., which came with a certificate for nanoparticle size and concentration. To find the size of the gold nanoparticles, each sample was measured using the Thermo Scientific NanoDrop 2000C spectrophotometer (See Fig. 9A). From each sample, 1 ml was pipetted into a cuvette and measured to produce absorbance spectra as a function of wavelengths. The wavelength for each sample was compared to the standard and showed strong correlation. The absorbance peaks were recorded for the calculation of the sample concentration. The correlation between peak absorbance and nanoparticle size was plotted and fitted to a quadratic equation (See Fig. 9B). In this manner, it was possible to assess the average particle size from any of our experiments producing radioactive gold nanoparticles.

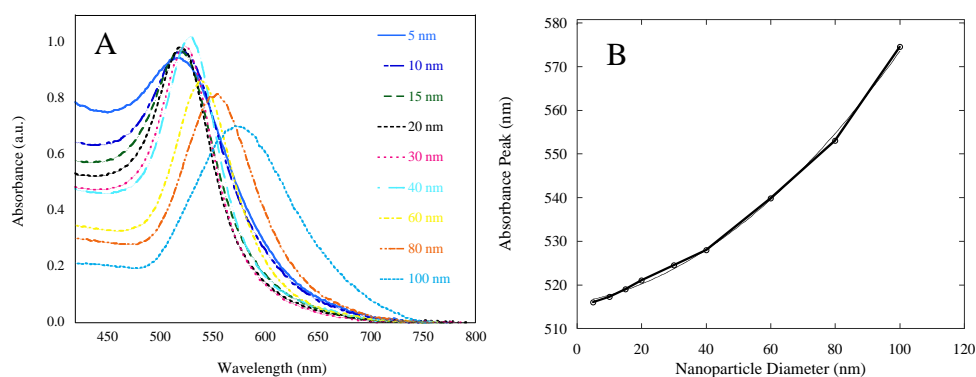


Figure 9. (A) UV-Vis absorbance as a function wavelength (nm) for different AuNP standards of 5, 10, 15, 20, 30, 40, 60, 80 and 100 nm in diameter obtained using a spectrophotometer (NanoDrop 2000C, Thermo Scientific, Inc.). (B) Absorbance peak as a function nanoparticle diameter obtained using different AuNP standards of 5, 10, 15, 20, 30, 40, 60, 80 and 100 nm. The relationship found was $A = 5.1602 \times 10^2 + 1.1918 \times 10^{-1} \times D + 4.5615 \times 10^{-3} \times D^2$ with a correlation coefficient of $R = 0.99905$. Adapted with permission (Hamoui 2015).

The concentration of gold nanoparticles was calculated using the Beer-Lambert law expressed as:

$$A = \varepsilon \cdot b \cdot C \quad (1)$$

where ε represents the extinction coefficients ($\text{M}^{-1} \text{cm}^{-1}$), b that is the path length (cm), and C is the concentration in the sample expressed in molar concentration (M), and A is the absorbance peak. The extinction coefficients, ε , were determined previously in the literature using UV-Vis spectroscopy of nanoparticles of different sizes and surface ligands (see Fig. 10A) (Liu et al. 2007). With consideration that the surface ligand was trisodium citrate and the path length of our spectrophotometer we can set $b = 1$ cm. The nanoparticle concentrations from our produced results were calculated using Eq. (1). The nanoparticle concentrations were then compared to standards supplied by CytoDiagnostics, INC (see Fig. 10B).

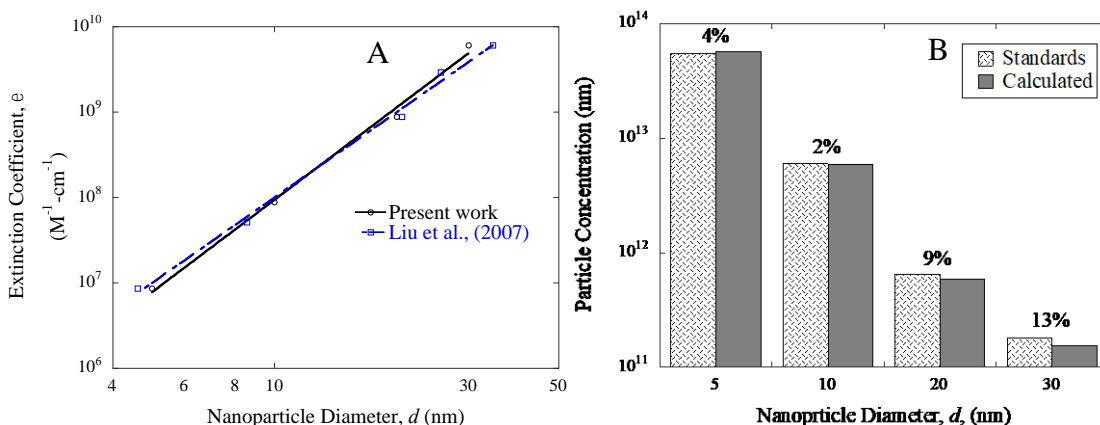


Figure 10. (A) The extinction coefficient, ϵ , as a function of nanoparticle diameter, d , was previously estimated by Liu et al., (Liu et al. 2007). Therefore, this estimation was compared with those calculated using the standards supplied by CytoDiagnostics, Inc. (B) Then a comparison between gold nanoparticle concentrations obtained from standards versus those calculated using the extinction coefficient, ϵ , given by the equation established from Liu et al., (Liu et al. 2007). The difference between our standards and those calculated were within reasonable range of each other. Adapted with permission (Hamoui 2015).

Further size characterization and image acquisition of the gold nanoparticles was performed utilizing TEM. TEM was performed using an H-7650 (Hitachi, Tokyo, Japan) FEI Tecnai G2 F20 Super-Twin. The H-7650 is a 200 keV model with a ZrO_2/W (100) Schottky Field emitter and an S-Twin objective lens. AuNP samples were prepared by dropping 10- μ l of solution on a copper TEM grid (Cat. N0. 71150, Electron Microscopy Science). Images were acquired using an automatic calibration of the microscope and a Charge-Coupled Device (CCD) (2k \times 2k CCD camera).

Furthermore, characterization of the stability of ^{125}I gold nanoparticles were tested by taking three 0.9 ml samples and allowing them to open air dry under a radiological fume hood for 4 days and examining loss of activity over time. Second, the non-radioactive

(10, 250, and 500 μl of 1×10^{-5} M sodium iodine solution in 1×10^{-5} M NaOH solution) and radioactive samples were characterized for their agglomeration in fetal bovine serum (FBS) from VWR (Pro. NO. 1400-100, Radnor, PA) and phosphate buffered saline from Lonza (Walkersville, MD).

2.6. Nebulizer System Design:

The mouse nebulizer system requires certain key attributes for its efficacy. To ensure distribution throughout the functional pulmonary parenchyma of mouse lungs, a large fraction of the aerosol needs to be less than 1 micron in diameter. This is accomplished via collaboration with AeroGen, Inc. using a mesh nebulizer specifically designed for mice. The mesh nebulizer used had a mass median aerodynamic diameter (MMAD) of 2.171 with a geometric standard deviation (GSD) of 2.037. A cylindrical mouse bed has been designed to hold the nebulizer, which fits at the top where the flow is biased towards the mouse nose and mouth. This was accomplished by making the nebulizer holder cone-shaped and pushing isoflurane into the system via independent ports in the back and removing flow from the system via slits near the mouth of the mouse to be used for removal of excess aerosol buildup and preventing condensation. Vacuum is also used to prevent contamination of the area around the mouse body. There was a thin latex sheet with a slit near the front of the nebulizer system so that the mouse nose and throat tightly fit into the system. The mouse nebulizer system will be used as an attachment to the micro-PET/CT so that delivery and uptake could be imaged in real time. Modeling was performed in Solidworks CAD software and exported as a stereolithography file (STL).

2.7. Manufacturing

The exported STL file was then sent to the engineering innovation center at Texas A&M University. The 3D printer chosen was the Stratasys EDEN 260V, which has a build volume of 255 x 252 x 200 mm (10.0 x 9.9 x 7.9 in.) with a 16-micron layer accuracy and 7-micron dimensional accuracy. The materials chosen were a soluble support material, which could be removed with ultrasonic bath and/or water-jet, along with Objet VeroWhite, which is a rigid opaque material with 1.1-1.5% water absorption. Figure 11 shows a rendering of the device to be used in the present studies. The device is made entirely from 3D printed VeroWhite Polyjet material. This material offers great resistance to fluid permeation and offers some of the highest resolution/surface finish of other 3D printing materials.

These features are important considering this device is used with radioactive fluids and the device must not harbor any residual contamination after use. Another key feature of the device is the internalization of the airway channels for both the vacuum and anesthesia systems. This is a feature of both function and convenience. By internalizing the channels, the anesthesia can be more effectively directed to the mixing chamber to mix with the aerosolized nanoparticle solution. The device also features two cap inserts that can be removed to more effectively clean the exhaust channels. There are three exhaust channels, two that connect to the mixing chamber near the mouth and one connected to a charcoal filter typically utilized for isoflurane. There is also one that

connects out to the bed where the mouse lays that should be connected to a vacuum pump with a charcoal filter as will be discussed in a later section.

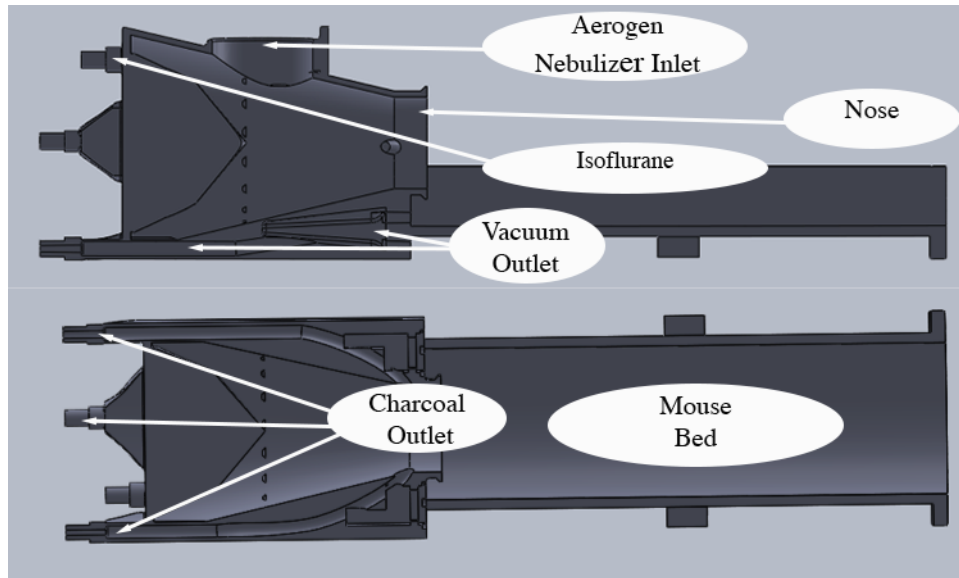


Figure 11. Preliminary design of the mouse nebulizer (cross-sections) to be implemented with the micro-PET/CT. The AeroGen, Inc. nebulizer inlet is located on top the system and the anesthesia gas mixture inlet are on the back. A vacuum outlet allows for the clearance of the cavity to prevent condensation.

2.8. Atomizer and Particle Distribution

There is a wide variety of methods used to produce aerosols. The proposed design for this research utilizes a piezoelectric mesh atomizer, which qualifies as a vibrating mesh small-volume nebulizer. The nose-only nebulization system features an AeroGen nebulizer, which contains a vibrating palladium mesh. There is a 5 mm diameter central aperture plate perforated with 1000 precision formed holes, vibrating at 128,000 vibration per second, producing the particle sizes optimal for deep lung penetration.

AeroGen claims a MMAD of 1-5 μm for this device. The AeroGen Pro for example was calibrated by AeroGen to have a MMAD of 3.7 μm . The deposition efficiency comparison between the AeroGen Pro and traditional small volume nebulizers (SVN) has been examined and reviewed (Ari, Areabi, and Fink 2010). It can be seen from the graphics in some papers using the AeroGen Pro that the deposition in the lung is more ubiquitous and penetrates deeper for the AeroGen Pro than for that of traditional SVNs. AeroGen claims that it is capable of producing lung deposition of 17% compared to a standard SVN with 3% lung deposition. The distribution of particle sizes produced from mouse nebulizer from AeroGen, that is repackaged by Aeroneb, INC., and sold at Harvard apparatus is presented in figure 12 alongside the deposition fraction per particle diameter as calculated from the previously discussed MPPD (Anjilvel and Asgharian 1995; National Institute for Public Health and the Environment (RIVM) 2002).

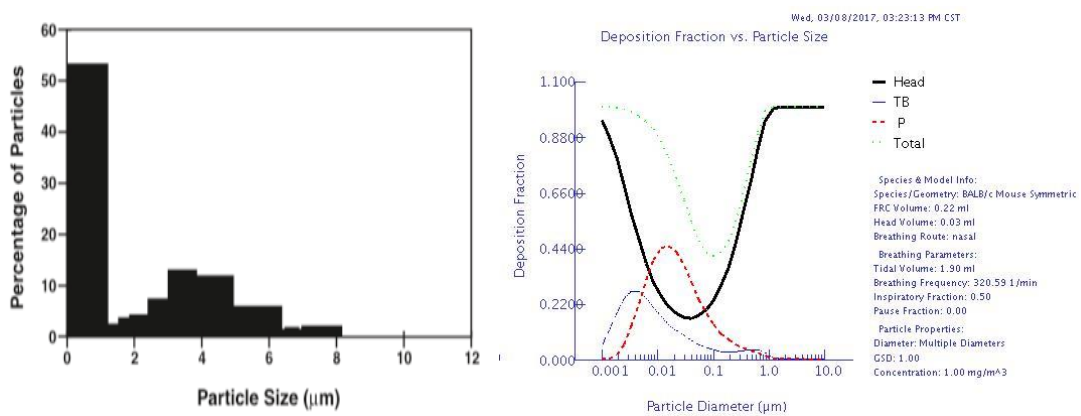


Figure 12. On the left is the particle-size distribution of aerosols produced by an AeroGen/Aeroneb, Inc. mesh nebulizer sold by Harvard Apparatus (Apparatus 2017). On the right is the aerosol deposition fraction vs particle size in mice obtained via simulations with Multiple-Path Particle Dosimetry Model (MPPD) software (Anjilvel and Asgharian 1995; National Institute for Public Health and the Environment (RIVM) 2002). Head: animal head; TB: tracheobronchial tree; P: parenchyma.

2.9. In-vivo/Ex-vivo Imaging Equipment

The Bruker AlbiraSi® is a high performance, Full Field of View multimodal PET, SPECT, CT system. A diagram of the AlbiraSi® is provided in figure 13.

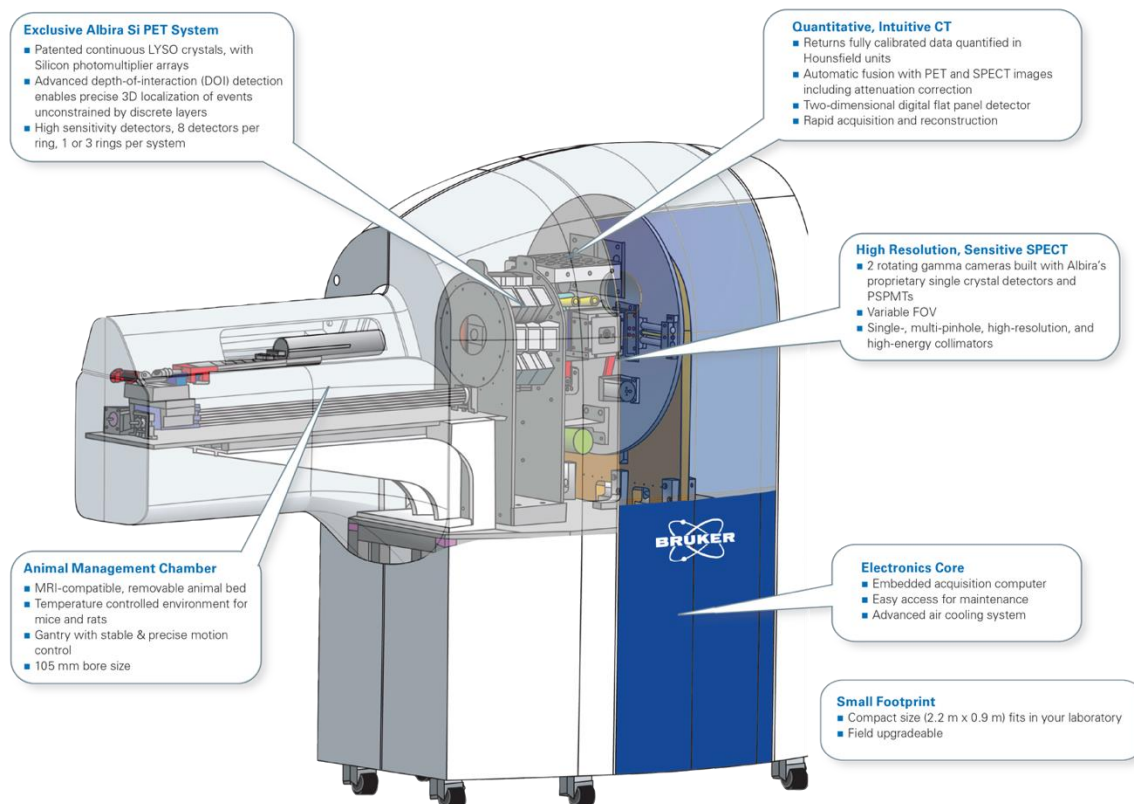


Figure 13. Detailed diagram of the AlbiraSi®, images supplied by courtesy of Bruker PCI with permission.

Some of the applications that the Albira system can provide are a deep insight into in terms of the underlying mechanisms of diseases and the effectiveness of new therapeutics are pharmacokinetics, pharmacodynamics, ADME, protein/gene expression, metabolic studies, toxicology, and perfusion studies. While, PET, SPECT, and CT imaging were the original purposes of the nose-only aerosol delivery system there is also

potential for its use in optical imaging. This potential is also stronger than its potential use with radionuclides as near-infrared (IR) and Far-IR probes can be used for significantly longer periods of time and build up a signal overtime when typical imaging radionuclides would have already decayed. The optical imaging equipment utilized for these experiments was the Bruker In Vivo Xtreme® (See Fig. 14), which has four built in imaging modalities (fluorescence, luminescence, radioisotopic, and X-ray). NSG mice engrafted with bioluminescent detectable human osteosarcoma xenografts into their left tibia were used. These cells were also modified to express green fluorescent proteins and as such the lung metastases were capable of being imaged using bioluminescence. These compounds don't require any excitation and are expressed in significantly higher quantities than what can potentially be delivered by injection, let alone nebulization. Therefore, optical imaging is the preclinical gold standard when imaging cancer metastases as no other modality can image them effectively at early stages.

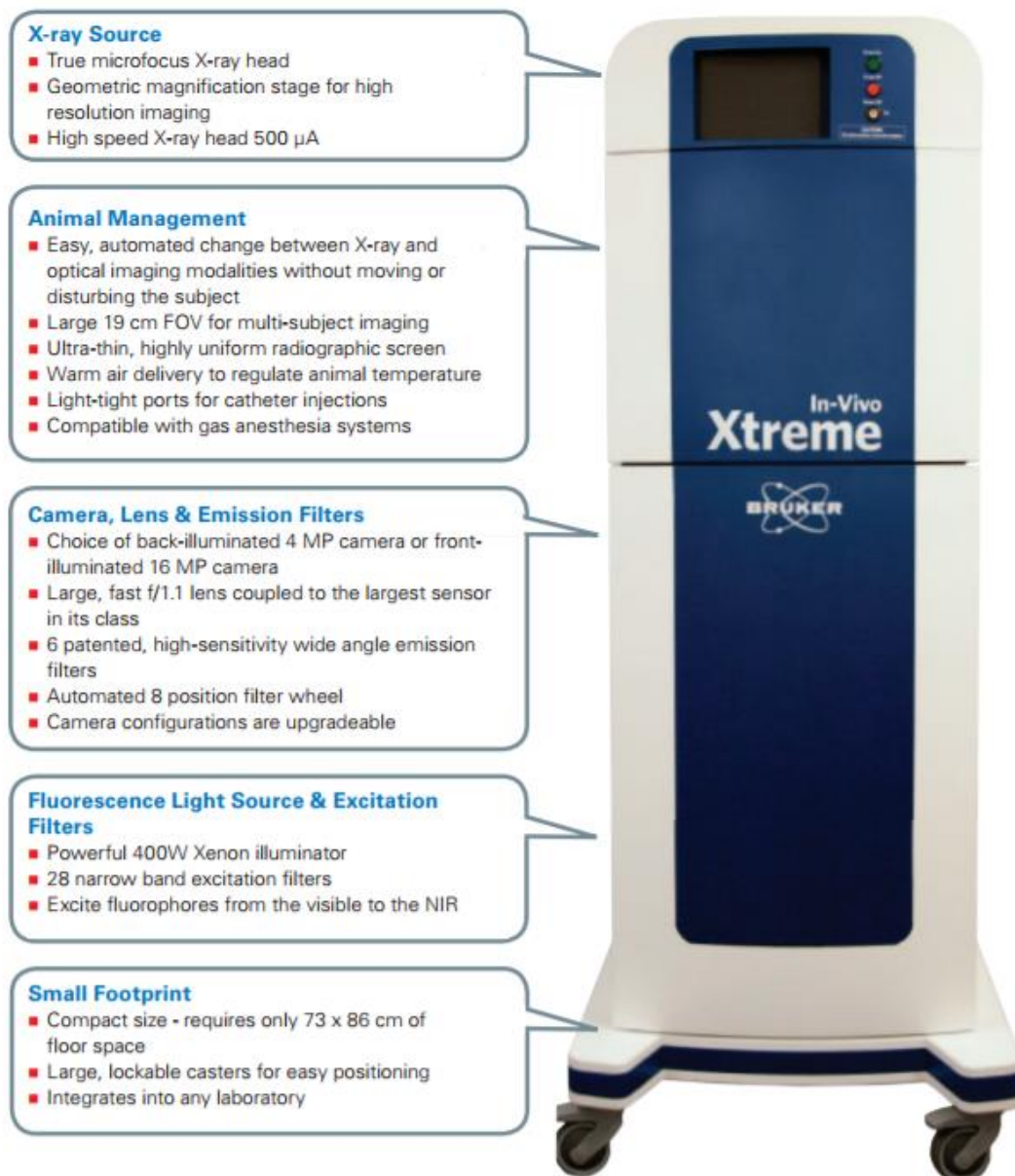


Figure 14. Detailed diagram of the Bruker In-vivo Xtreme®, images supplied by courtesy of Bruker PCI with permission.

Fluorescent probes are also frequently utilized for confocal imaging. Like the fluorescent modality of the Bruker In Vivo Xtreme®, Confocal microscopy utilizes a laser to image thin slices of tissues or any sample material you are looking at.

2.10. Integration

Figure 15 illustrates the integration of the system with the complete assembly in the Albira Si®. While this was the original plan for the nebulizer system, the device can be used as a standalone inside of a fume hood with connections to anesthesia and outlet towards charcoal filter. A Fume hood was utilized for the optical imaging studies.



Figure 15. The assembly of the device with vacuum and anesthesia lines connected in the rear and the AeroGen nebulizer mounted on top and integrated into the Albira Si.

2.11. Anesthesia System

The device features an anesthesia supply connected via the two input leads on the rear end of the device. This supply features a variable isoflurane-oxygen mixture. The isoflurane mixture served as a mechanism to push the aerosol toward the nose of the specimen and to the vacuum. An interesting feature of the design is that utilizing the funnel design we used the anesthesia supply to spin the aerosol in the chamber toward the mouse nose keeping it from touching the walls or creating gaps of aerosol in the chamber.

2.12. Mixing Chamber

The mixing chamber of the device required significant consideration in the design of the geometry. Intuition mandated a funnel design that would attempt to reduce deposition, due to geometrically induced turbulence, of the aerosol on the walls of the mixing chamber. The origin of this turbulence would stem from the “hard-edge” geometry of a straight cylinder. The anesthesia system features two ports at the rear end of the device designed to “push” the aerosol through to the other end of the mixing chamber.

Originally, these two ports consisted of an entire annulus with integrated blades intended to focus the aerosol to the other end of the mixing chamber. However, due to complications with the 3D printing process due to removal of soluble supports, the blades were abandoned and the annulus width shortened, allowing for soluble support removal. Even at distances relatively close to the atomizer, there is homogeneity in terms of mist velocity and spatial particle distribution. In addition, the generated particles seem

to be less prone to coalescence and the consequent polydispersity, which contrasts with jet nebulizers.

2.13. Exhaust/Aerosol Removal System

The device features a vacuum exhaust system that removes the excess aerosol from the surrounding environment in case there is leakage from the nose (See Fig. 16).

Originally, there was a vacuum exhaust which regulated the flow of the aerosol to consistently pass in front of the nose of the rodent for sustained dosage. However, it was found that suction removed the aerosol to a degree that it was not breathed. It was also found that when the mouse's nose was snugly fit into the nose piece, pressure would push the aerosol down the lines to the charcoal filter without the need for vacuum.

Therefore, only one outlet, which is used for air outside the aerosol compartment was used for this vacuum system. This feature is a key element in maintaining isolation of the specimen from radioactive contamination. In the event the aerosol leaks to the housing chamber with the rodent bed, the vacuum system will remove the impurities from this region through the outlets.



Figure 16. The vacuum system used during experimentation. This vacuum system would remove any potential leakage of fluorescent probe or radionuclide from the mouse housing portion of the nebulizer system.

2.14. Physiological Monitoring

The BIOPAC® physiological monitoring system is a feature of the Albira Si. This feature played a large role in characterizing the breathing pattern of the rodent specimens. It consists of an air-filled, foam-like device that can expand and contract under the pressure of the body of the mouse (See Fig. 17). The pressure changes inside the device provided readings that can be represented graphically. We were not able to use this throughout these preliminary experiments but it will be incorporated into future models for respiratory gating.



Figure 17. This figure portrays the BIOPAC respiratory gating detector. This detector will allow monitoring of the mouse breathing and how much aerosol is being delivered based on the breathing pattern.

2.15. Containment & Isolation System

The containment/isolation system of the therapeutic device consists of a cylindrical acrylic exterior which should be airtight and capable of displacing all radioactive aerosols from the region. Failure to maintain isolation would result in contamination of the region surrounding the rodent specimen thereby rendering imaging by the Albira Si ineffective and potentially useless. One key component is that when the bed system is sealed properly the vacuum system will pull the air from around the mouse and simulate a negative pressure system. When the mouse's nose is secured properly the internal chamber acts like a positive pressure system to remove excess aerosol as well, so one can observe fluid going towards the charcoal filter.

2.16. Cytotoxicity

A label-free RTCA was used to assess cell growth and cell-mediated toxicity of cytotoxic agents to attached cells. The xCELLigence RTCA DP analyzer (ACEA Bioscience, Inc. San Diego, CA) uses impedance measurement to assess the real-time response of attached cells to x-ray radiation, chemotherapeutics, and ^{198}Au NPs on SKBr-3 cells. The system has three plates and each plate has 16 wells that are continuously monitored by the system, providing a real-time cell index response as a function of time. The cell index (CI) response has arbitrary units. Using experimental controls, the response of a cytotoxic agent can be estimated as a function of time. This system supersedes the use of the commonly used clonogenic assay (Franken et al. 2006), which only determines the potential for proliferation of cell *in vivo* as a function of absorbed dose or molar concentration.

The RTCA system requires the determination of an optimal number of cells for seeding (per well) as to allow such cells to proliferate for a period time before treatment with a cytotoxic agent. To assess the optimal seeding per well, an initial experiment was carried out using various seeding numbers (3300, 5500, 10000, and 25000 cells per well). Once the optimal seeding number was established for SKBr-3 ^{198}Au gold nanoparticles were tested for their cytotoxicity.

2.17. Mouse Imaging and Nebulizer System Characterization

To establish an orthotopic xenograft mouse model of osteosarcoma, NOD/SCID IL2-R-gamma -/- mice (The Jackson Laboratory) aged 4-6 weeks (males and females) were injected in their left tibias while under isoflurane anesthesia (1-2% v/v in pure O₂) with a 10 μ l PBS suspension of SJSA-1 cells (ATCC) constitutively labeled via lentiviral transfection with firefly luciferase and GFP, for tracking the tumor progression in vivo and location for histology *ex vivo*. For the AuNP and micelle studies the injection dose of SJSA-1 cells was 50,000 cells.

For this procedure, a 27 Ga syringe needle is drilled into the proximal epiphysis of the tibia and guided down the tibia about mid-way to the diaphysis, where the suspension is injected. Five days following engraftment, the mice were given intraperitoneal injections of 0.15 ml of 30 mg/ml D-luciferin potassium salt (Bioworld) and imaged for optical signal 15 minutes later using a small-animal optical imaging cabinet (Xtreme In Vivo, Bruker). X-ray images of the mice were also taken to provide anatomical reference. Baseline metastatic burdens in the lungs were then determined by measuring the signal intensity in the chest region of each mouse. The mice were then assigned to one of three groups, determined randomly but matching for similar average baseline lung signals among groups.

For the AuNP studies mice were nebulized with 2 ml of nonradioactive iodine AuNP or non-iodinated AuNP suspensions under isoflurane anesthesia lasting no more than 20

minutes on Days 22, 23, and 24 from the time of tumor engraftment (See Table 1). For the micelles mice were nebulized on Days 6, 7,8,9,10, 12,14, and 17 with 1 ml of either PBS only, 0.18 mg/ml dimerized paclitaxel prodrug dissolved in PBS with 5% DMSO, or 0.18 mg/ml dimerized paclitaxel loaded in Near IR-labeled PEG-b-PGC micelles in PBS. Only images were obtained from the micelles to characterize the nebulization system and PBS was used for both controls. Isoflurane anesthesia was maintained throughout nebulization at a low level (0.5 - 1% v/v in pure O₂) to prevent the mice from moving too much during the procedure and getting exposed to the mist on their eyes or skin. Directly following nebulization, the mice were imaged again to obtain the fluorescence signal from the nanoparticles (excitation 760 nm / emission 820 nm for micelles and excitation 690 nm / 750 nm emission for AuNPs) in the lungs. Nebulization was performed for three consecutive days and then re-imaged for fluorescence signal.

Table 1. The mice were split into two groups either having the AuNPs or the Au-I-NPs and are categorized below.

	AuNPs	Au-I-NPs
ANIMAL IDENTIFICATION	170907A	170907B
	170907F	170907D
	170907K	170907E
	170907I	170907J

On Day 19 for the micelles and Day 28 for the AuNPs the mice were euthanized via CO₂ asphyxiation and dissected to recover the lungs and other organs. The lungs were then

inflation fixed by intratracheal instillation 4% formalin in neutral buffered saline for 30 minutes. This was followed by immersion in 15% sucrose/PBS mixture for 30 minutes, and then 30% sucrose/PBS mixture for another 30 minutes. The lung tissue was then split into 5 distinct lobes, placed in cryomolds with a drop of optimal cutting temperature (OCT) media (Tissue-Tek®, Sakura® Finetek). The distinct lobes were the superior lobe (SL1), middle lobe (ML2), inferior lobe (IL3), post-caval lobe (PCL4), and left lung (LL5). They were then imaged *ex vivo* with optical imaging at the previously mentioned laser levels (See Fig. 18). Then the lobes will be submersed in OCT and snap frozen in dry-ice/ 100% ethanol slurry for cutting and imaging using confocal microscopy.

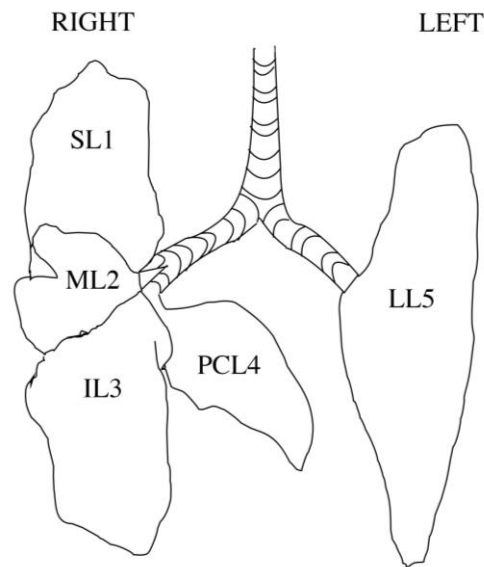


Figure 18. This figure depicts how each lobe of the mouse lungs was characterized before being split up for imaging.

For microscopic analysis, the frozen tissue was sliced into 20 micron sections using a cryostat (Cryotome®, ThermoFisher Scientific) at -15 °C. The sections were mounted

onto slides and cover-slipped with optical medium (Fluoromount-G, ThermoFisher Scientific). Confocal-microscope imaging (Fluoview FV1000, Olympus) was performed to evaluate the distribution of nanoparticles within the lung tissue with reference to the GFP-labeled tumors. Images were acquired using a 10x air objective with laser excitations at 488 nm (GFP) and 635 nm (NIR) along with a transmission light detection unit and Nomarski DIC to visualize the lung structures in high detail. Imaging of the entire lung slices was achieved with a motorized XY stage (Prior Scientific) and the Olympus FV10 software. A multiarea time lapse protocol in the Olympus Fluoview® software was used for drawing regions around each lobe of the mouse lungs and imaging with an aspect ratio of 640 by 640. Mosaic stitches of the entire lung sections were analyzed for intensity using ImageJ.

CHAPTER III

RESULTS

3.1. SKBr-3 RTCA cell seeding experiments

A cell seeding experiment was carried out to determine the optimal conditions for SKBr-3 growth over an observation period to prevent the need to change the growth medium too early during a study (See Fig. 19). The RTCA system was thus seeded with densities of 3300, 5500, 10000, and 25000 cells per well. Figure 19 illustrates the cell index (CI) response as a function of time for a period of more than 190 h. The maximum CI achieved by these cells was estimated at 3.0 without exchanging the cell growth media.

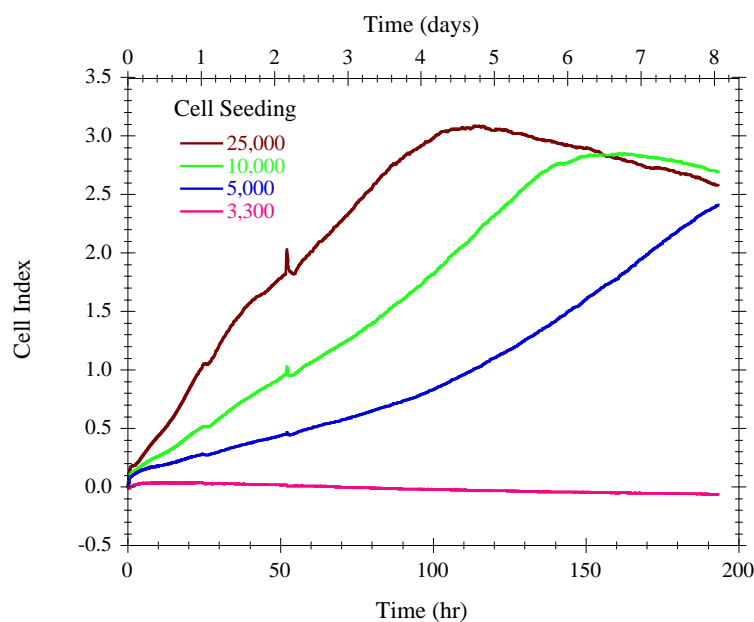


Figure 19. RTCA cell Index (CI) response as a function of time for seeding per well of 3,300 (pink), 5,000 (blue), 10,000 (green) and 25,000 (red) per well. The optimal seeding was determined at 10,000 cells per well within a time lapse of less than 196 h. Reprinted from (Hamoui 2015).

The optimal seeding concentration was chosen to be approximately 10,000 cells per well. This would cause the CI to reach a value of 1.5 within 84 hours, thus allowing the assessment of potential cytotoxic response for $CI < 1.5$ or re-growth response for $CI > 1.5$ past 84 hours without concern of well saturation or need to replace media less than three days after administration of the compound of interest. This concentration also offered the most consistent results suggesting some leeway in administration of cell concentration without significantly altering growth. Based on these results, future experiments were carried out at a seeding of 10,000 cells per well.

3.2. Estimation of number of ^{198}Au radioactive atoms per nanoparticle

Once radioactive nanoparticles were generated using the previously mentioned Turkichev method, the total activity per unit volume ($\mu\text{Ci/ml}$) was estimated using a dose calibrator (AtomLab 500, Biodex, Inc.). When a sample of solid chloroauric acid is activated via the $^{197}\text{Au}(n,\gamma)^{198}\text{Au}$ reaction, only a fraction of the ^{197}Au gold atoms are transformed into ^{198}Au . Overall, the fraction of atoms that are transformed into radioactive gold is very small when compared to the total number of atoms of gold in the sample. This fraction heavily depends on neutron irradiation conditions, such as neutron flux ($\text{n cm}^{-2} \text{s}^{-1}$), irradiation time, and decay (*e.g.*, due to delay in shipment). The nominal neutron flux used to irradiate our samples at the Nuclear Science Center was approximately $1 \times 10^{13} \text{ n cm}^{-2} \text{ s}^{-1}$. The specific activity of a radioactive sample was estimated using an HPGe detector. Specific activity is the total activity per unit mass of a compound (*i.e.* HAuCl_4) and it is commonly expressed in MBq per mg.

The number of radioactive gold atoms (^{198}Au) per nanoparticle follows the Poisson distribution and depends on the average nanoparticle size or average diameter of nanoparticles along with the specific activity. As a result, large particles may contain more radioactive atoms than small particles, and *vice versa*. The distribution of AuNP diameters obtained from TEM images (See Fig. 20) was used to carry out these calculations and convoluted with the Poisson distribution.

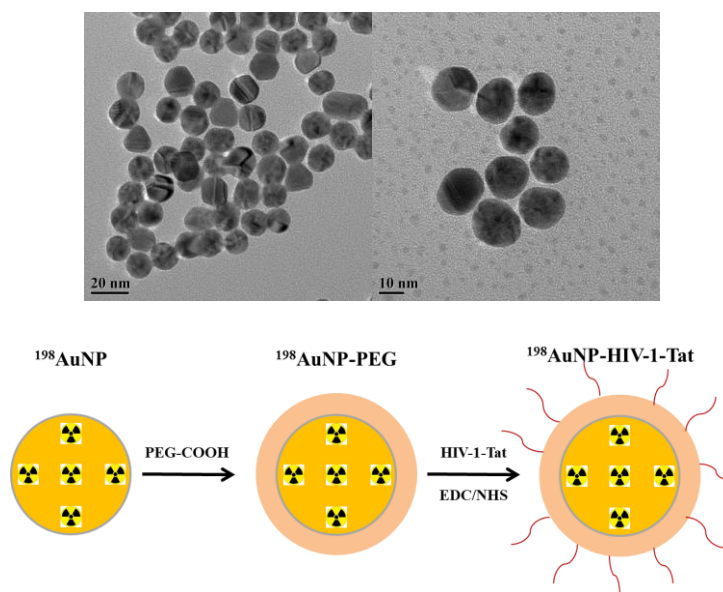


Figure 20. TEM figures of in-house produced AuNPs and schematic representation showing the functionalization of a radioactive AuNP using PEGylation methods and attachment of the cell penetrating peptide HIV-1-Tat. Reprinted with permission (Hamoui 2015).

The average activity (Bq) per nanoparticle, A_{NP} , is the product of the nanoparticles mass multiplied by the specific activity, SA :

$$A_{NP} = V_{NP} \cdot \rho \cdot SA = \frac{4}{3}\pi r_{NP}^3 \cdot \rho \cdot SA \quad (2)$$

where r_{NP} is the radius of a nanoparticle. The average number of radioactive atoms per nanoparticle, N_{NP} , is then given by:

$$N_{NP} = \frac{A_{NP}}{\lambda} \quad (3)$$

where $\lambda = 2.98 \times 10^{-6} \text{ s}^{-1}$ is the decay constant of ^{198}Au . Thus, the average number of radioactive atoms increases with specific activity SA . The probability of number of radioactive atoms per nanoparticles with a specific radius is given by:

$$P(x) = \frac{\mu^x e^{-\mu}}{x!} \quad (4)$$

where $m = N_{NP}$ is the average number of radioactive atoms in a nanoparticle. Thus, the fraction of radioactive atoms as a function of SA for a nominal nanoparticle diameter of 15.9, based on diameter averages of TEM images obtained using similar synthesis procedures, is given in Figure 21.

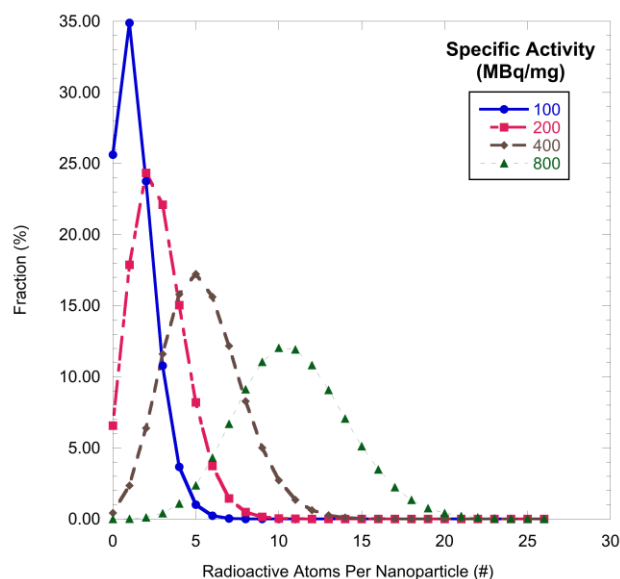


Figure 21. Depicted is a poisson distribution for the fraction or probability of having a certain number of radioactive atoms of ^{198}Au per nanoparticle as a function of SA (MBq mg^{-1}). The potential fraction of nanoparticle that will have zero radioactive atoms decreases exponentially as a function of SA. The nominal diameter for the nanoparticles used in these calculations was 15.9 nm. Adapted with permission (Hamoui 2015).

Once radioactive nanoparticles were produced, it was then possible to assess the distribution of radioactive atoms per nanoparticle in each solution using an estimate of the average diameter, nanoparticle concentration (nanoparticles per milliliter), and activity concentration per unit volume of the sample. The average diameter can be calculated using the UV-Vis method; the concentration of nanoparticles can be estimated using the optical absorption, and the activity concentration (not specific activity) using a dose calibrator. Therefore, we can write:

$$\mu = \frac{1}{\lambda (s^{-1})} \frac{\text{Activity Concentration}, A (Bq ml^{-1})}{\text{Nanoparticle Concentration}, NP (NPs ml^{-1})} \quad (5)$$

and based on the Poisson distribution, the fraction of nanoparticles with zero radioactivity atoms is given by $P(0) = e^{-\mu}$, similar estimates can be made for one radioactive and multiple radioactive atoms per nanoparticle.

These calculations were required to assess how many radioactive atoms and corresponding decays would occur per nanoparticle. Each radioactive decay will emit certain characteristic radiative emissions based on the decay scheme of ^{198}Au . For a given nanoparticle, each radiative emission will occur in the same cell when the nanoparticle is entrapped in the cell surface or internalized in the cytoplasm, yielding a higher dose per tumor cell.

3.3. Characterization of ^{198}Au NPs

To characterize the produced radioactive gold nanoparticles, 1 ml of the resulting solution was used to assess the surface plasmon resonance using the NanoDrop 2000C spectrophotometer. Figure 22A shows the UV-Vis spectrum as a function of photon wavelength. The absorbance peak was measured at 525 nm, which corresponded to particle size of 32.9 nm. The measured absorbance peak at 525 nm was 1.34 resulting in a concentration of 2.29×10^{11} (NP/ml). Using the dose calibrator, the measured activity of the 1 ml sample was 480 ($\mu\text{Ci/ml}$). The estimated number of ^{198}Au atoms per nanoparticle was 25.9, which resulted in a negligible zero-fraction ($P(X = 0) = e^{-25.9}$).

TEM was used to characterize the shape, size, and particle number of non-radioactive AuNP. Reproducible synthesis of AuNP was confirmed by TEM analysis. Image analysis for nanoparticle diameter was carried out using the software program ImageJ (Schneider, Rasband, and Eliceiri 2012). A narrow distribution for AuNP was obtained with a range between 11.6 and 23.5 nm and an average diameter of 15.9 nm (Fig. 22B)

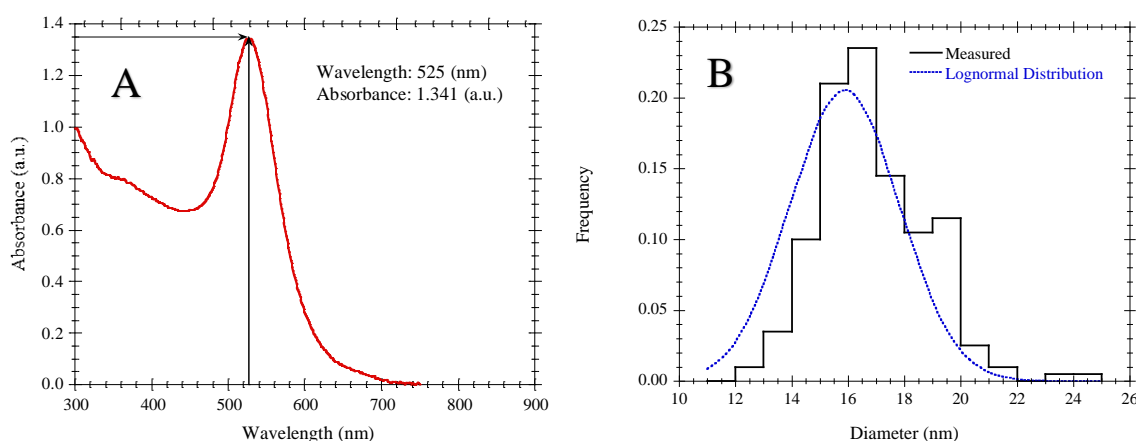


Figure 22. In this figure (A) is the UV-Vis spectrum of radioactive gold nanoparticles, and (B) is TEM image analysis, which demonstrated a narrow particle size distribution, with a size range between 11.6 and 23.5 nm and an average diameter of 15.9 nm. The surface plasmon resonance had a maximum peak observed around 525 nm with an absorbance of 1.341 corresponding to a gold nanoparticle diameter of 32.9 nm at a concentration of 2.29×10^{11} NP/ml. A lognormal distribution was fitted to the data which depicted a negative skew of the measured distribution towards larger size nanoparticles. In collaboration with Hamoui with permission (Hamoui 2015).

3.4. Cytotoxicity of $^{198}\text{AuNPs}$ and $^{198}\text{AuNPs-HIV-1 Tat}$

The cytotoxicity of radioactive $^{198}\text{AuNPs}$ was assessed using the RTCA system to examine the effect on SKBr-3. We seeded 10500 tumor cells per well and after 30 hours of incubation, HIV1-Tat functionalized and non-functionalized $^{198}\text{AuNP}$ with different activities were added into the wells in quadruplicates. The activities used were 50, 100,

500, 1000, and 1500 kBq. The experimental arrangement was as follow; 1) SKBr-3 cells used as a control, 2) SKBr-3 cells treated with AuNPs (non-radioactive), 3) SKBr-3 cells treated with AuNP HIV-1 Tat (non-radioactive), 4) SKBr-3 cells treated with $^{198}\text{AuNPs}$, 5) SKBr-3 cells treated with $^{198}\text{AuNP HIV-1 Tat}$.

Figure 23 presents the cell growth response as a function of time for the different experimental arrangements as described above. The incubation period was for 12 hours and after that the medium was exchanged and cells were washed once to remove any non-internalized nanoparticles. However, it is important to mention that we were not able to determine the fraction of activity that was retained in the wells after washing them with PBS. We expected that internalization of $^{198}\text{AuNPs-HIV-1 Tat}$ will have a significant impact in cell growth; however, as observed in figure 23A, the growth profile of $^{198}\text{AuNPs}$ and $^{198}\text{AuNPs-HIV-1 Tat}$ was similar with a minimal reduction in CI by those treated with $^{198}\text{AuNPs-HIV-1 Tat}$. The cell response to non-radioactive AuNPs-HIV-1 Tat was like that of controls; this indicates that the non-radioactive AuNPs-HIV-1 Tat had no effect on the SKBr-3 cells growth, which corroborates many studies that AuNPs have little cytotoxic capability on their own (Connor et al. 2005; Shukla et al. 2005; Villiers et al. 2010).

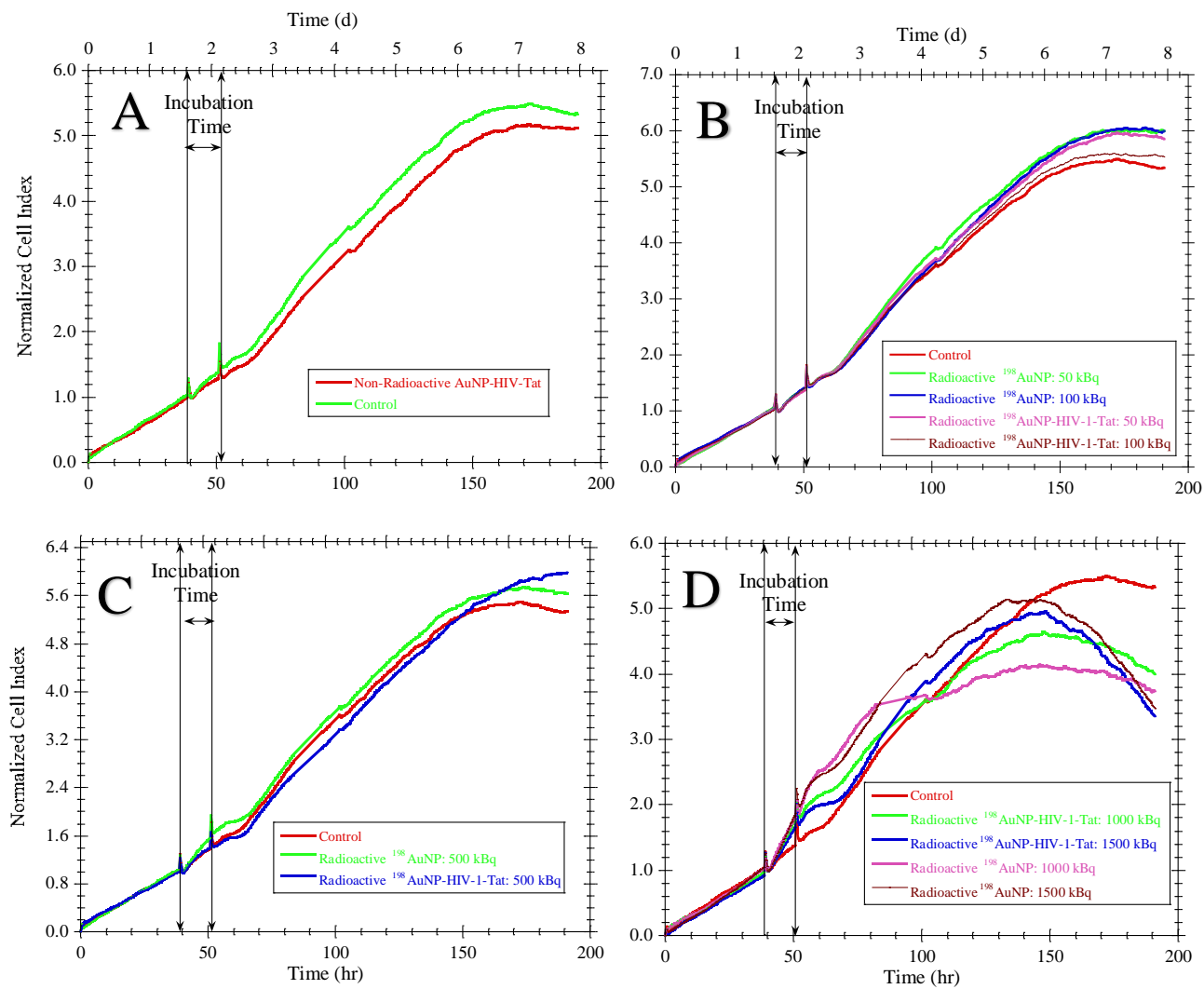


Figure 23. (A) Normalized Cell Index as a function of time for SKBr-3 cells exposed to nonradioactive AuNP (green line) and control (red line). (B) Normalized Cell Index as a function of time for SKBr-3 cells exposed to $^{198}\text{AuNPs-HIV-1 Tat}$ with an activity of 50 kBq (green line) and 100 kBq (blue line), $^{198}\text{AuNPs}$ with an activity of 50 kBq (pink line) and 100 kBq (brown line), and control (red line). (C) Normalized Cell Index as a function of time for SKBr-3 cells exposed to $^{198}\text{AuNPs-HIV-1 Tat}$ (green line) and $^{198}\text{AuNPs}$ (blue line) with an activity of 500 kBq and control (red line). (D) Normalized Cell Index as a function of time for SKBr-3 cells exposed to $^{198}\text{AuNPs-HIV-1 Tat}$ with an activity of 1000 kBq (green line) and 1500 kBq (blue line), $^{198}\text{AuNPs}$ with an activity of 1000 kBq (pink line) and 1500 kBq (brown line), and control (red line). The solid black lines represent the incubation time between the addition of the AuNP and the time when the medium was replaced. In collaboration with Hamoui with permission (Hamoui 2015).

In terms of activity, the cell growth response to 50, 100, and 500 kBq of $^{198}\text{AuNPs}$ and $^{198}\text{AuNPs-HIV-1 Tat}$ was not significant as shown in Figure 23 (B and C); the cell growth response was comparable to controls. Interestingly, 50 kBq and 100 kBq may show a promotion of cellular growth adding strength to theories that at low doses there is competition between death, repair, and defense mechanisms. However, the cell death response to 1000 and 1500 kBq of $^{198}\text{AuNPs}$ and $^{198}\text{AuNPs-HIV-1 Tat}$ was observed distinctly. This shows that doses below 1000 kBq were too low to yield a cell death response.

The cell response to $^{198}\text{AuNPs-HIV-1 Tat}$ and $^{198}\text{AuNPs}$ with activities of 1000 and 1500 kBq was initially observed in the slope of the spectrum. Following the exchange of the medium inside the wells, a decrease in the slope was observed. This showed that the cells duplication rate was slowed as a function of time. The major observable effects of radioactive AuNP were seen after 150 h (~ 6 d), where the CI of the treated cells started declining with a very fast rate resulting in observed cell death afterwards, while the trend of the controls kept growing until reaching a plateau at 175 h (~ 7 d).

3.5. Determining Influence of Time on Iodine Addition

We investigated the influence of time and stability of nanoparticles during their synthesis with the addition of non-radioactive NaI. Timing was found to be critical as it controlled the size distribution of nanoparticles and their aggregation. The diameters of the resulting I-AuNP at various time intervals were measured using UV-Vis, resulting in

a broad range of sizes. Figure 24 shows that AuNPs were partially size-stabilized at approximately 50 seconds after the addition of sodium citrate. Therefore, this was used as a threshold at which ^{125}I can be added without a drastic destabilization of the surface charges of AuNPs leading to rapid aggregation.

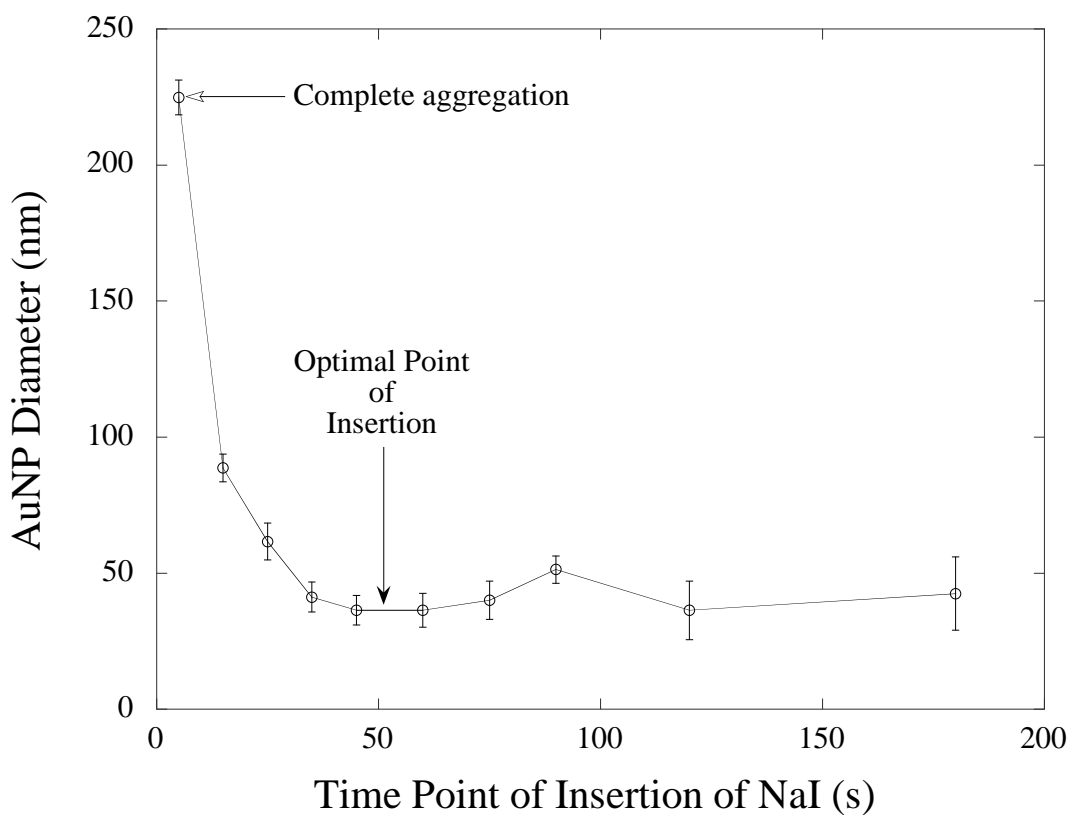


Figure 24. Estimated diameter of AuNPs using UV-Vis obtained with nonradioactive sodium iodine (NaI) added at different time points following after addition of sodium citrate during AuNP synthesis. Reprinted with permission (Clanton et al. 2017).

3.6. Characterization of Iodine Integrated AuNPs

Based on the injection threshold of 50 seconds after the addition of sodium citrate ($\text{Na}_3\text{C}_6\text{H}_5\text{O}_7$), non-radioactive iodine was replaced with Na^{125}I (no carrier added).

Following synthesis several 0.9 ml AuNP samples with approximately 11.5 μCi each of activity were taken from the reaction vial and allowed to dry under air in a radiochemical fume hood over a period of 4 days. Over the 4-day period, we found negligible loss of $^{125}\text{I}_2$ activity resulting from oxidation and sublimation. The same was observed from the dry nanoparticles obtained from nanopore filter paper insert after centrifugation in an Eppendorf tube. The ^{125}I was found to be associated with the nanoparticles on the nanopore filter paper and negligible radioactivity close to the background radiation was found in the supernatant.

Solutions of control (no iodine added), 10 μl NaI, 250 μl NaI, 500 μl NaI, and 302 μCi Na^{125}I were used to test the stability of our synthesized gold nanoparticles in fetal bovine serum and phosphate buffer saline (See Fig. 25). It appears that iodine has the capability of increasing the stability of gold nanoparticles in solutions of phosphate buffer saline. Phosphate buffer saline has previously been corroborated to induce aggregation of gold nanoparticles (Du et al. 2012). None of the nanoparticles seemed to aggregate in the presence of fetal bovine serum and no hindrance in stability was observed. No changes have been observed to this date (~8 days later) in either solution mixtures past 48 hours besides the 500 μl NaI solution beginning to settle at the bottom of tube. However, once agitated the sediment resuspended. In terms of Na^{125}I nanoparticles the fetal bovine serum had no activity in the solution but there was activity in the phosphate buffered saline. However, it can be noted from figure 25 that there is an apparent alteration in the nanoparticles denoting aggregation. Future studies may need to look at adding non-

radioactive iodine in conjunction with radioactive to increase the stability of nanoparticles in phosphate buffered saline. Just 10 μl of 10^{-5} M NaI in 10^{-5} M NaOH solution can prevent aggregation in phosphate buffered saline, which adds to the evidence that if iodine is added at the proper moment of AuNP synthesis then the AuNPs will be more stable. An interesting observation was that after centrifugation AuNPs without iodine could be pipetted out of solution without issue but AuNPs with iodine would continue to leak back into the solution as the pipette was being taken out. This concept may be an important consideration in other nanoparticle studies that are finding it difficult to produce stable nanoparticles in phosphate buffer saline or fetal bovine serum.





















	Control	10 μl NaI	250 μl NaI	500 μl NaI	302 μCi
Fetal Bovine Serum (0 hours)					
Phosphate Buffer Saline (0 hours)					
Fetal Bovine Serum (48 hours)					
Phosphate Buffer Saline (48 hours)					

Figure 25. The solutions of the gold nanoparticle containing different quantities of iodine in fetal bovine serum and phosphate buffer saline are depicted. The larger the amount of iodine added the more stable the nanoparticles appear in phosphate buffer saline. Reprinted with permission from (Clanton et al. 2017).

TEM imaging was conducted at the Texas A&M Microscopy and Imaging Center. For safety considerations, TEM was performed on the gold nanoparticles integrated with non-radioactive iodine to prevent contamination of the TEM. TEM images revealed that the synthesized AuNPs were roughly spherical (see Fig. 26) with an average diameter of 20 nm. Unfortunately, Electron Diffraction Spectroscopy (EDS) and X-ray Diffraction

(XRD) were ineffective in assessing the iodine content in AuNPs as these modalities both have a detection limit of about *ca.* 1% in atomic content.

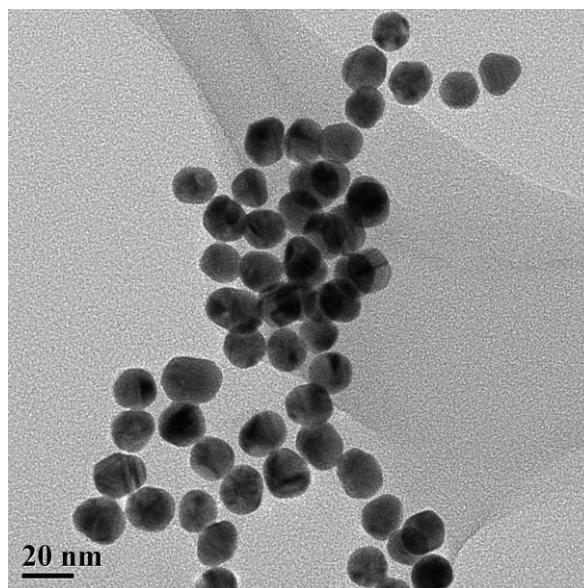


Figure 26. TEM image of AuNPs synthesized with non-radioactive iodine. The average diameter was 20 ± 5 nm (95% CI). Reprinted with permission from (Clanton et al. 2017).

3.7. Activity distribution of Iodine Integrated AuNPs

In our first experiment, we used a total net activity of 3.7 MBq (100 μ Ci) and 0.555 mg of pure gold. Using the previously mentioned Poisson equations for the number of radioactive atoms per nanoparticle, this resulted in a nominal $\mu = 2.77$ for 20 nm nanoparticles. In our second experiment, we repeated with 1.7 MBq (46.7 μ Ci) and 11.2 MBq (302 μ Ci) obtaining similar results. Figure 27 shows the Poisson distributions where the fraction of nanoparticles with no radioactive atoms was approximately 6% in the 100 μ Ci samples and 0% in 302 μ Ci samples.

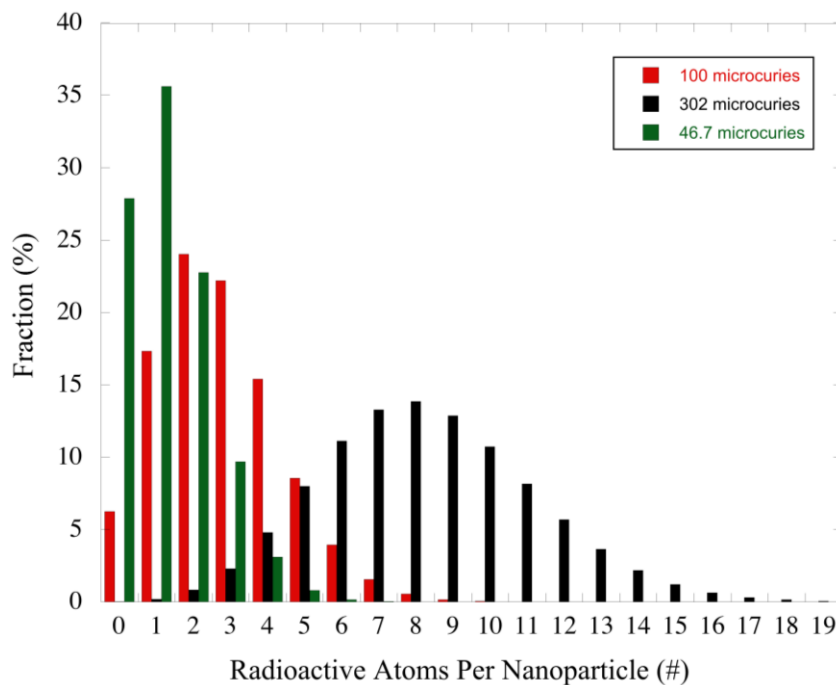


Figure 27. This figure presents Poisson distributions assessing the fraction of radioactive atoms per nanoparticle. The average diameter of an AuNP was 20 nm. Reprinted with permission from (Clanton et al. 2017).

The probability at time (t) that exactly a specified number of decays (d) per AuNP have occurred can be obtained by the binomial distribution:

$$P(d; t) = \frac{x!}{d!(x-d)!} (1 - e^{-\lambda t})^d (e^{-\lambda t})^{x-d} \quad (6)$$

where d is the number of radioactive atoms that decay, t is the time after synthesis, λ is the decay constant of the radioactive atom in question, x is the population size of radioactive atoms per AuNP (same as the previously obtained Poisson distribution).

When multiplied by the previously obtained Poisson distribution (independent probabilities), a probability density function can be obtained for a certain number of decays at a given time (t) for a certain number of radioactive atoms per AuNP (x).

$$P(x \cap d; t) = \frac{e^{-\mu} \mu^x}{d!(x-d)!} (1 - e^{-\lambda t})^d (e^{-\lambda t})^{x-d} \quad (7)$$

This density function provides the basis for the microdosimetry of radioactive nanoparticles near sensitivity targets, including DNA, as previously described (Balagurumorthy et al. 2012; Humm, Howell, and Rao 1995).

3.8. Astatine-211 Integrated Nanoparticles

For the ^{211}At integrated AuNPs, the supernatant and the samples were separated and measured utilizing the dose calibrator. The nanoparticles were found to have 28 μCi or approximately 80% retention of the initial activity. This established that the colloidal gold nanoparticles were successfully formed with radioactive ^{211}At . The final solution was then placed in a cuvette and diluted to a volume of 1 ml. Utilizing UV-Vis spectroscopy, the wavelength and absorbance peak were measured to assess the nominal nanoparticle size and concentration. The measured wavelength was 525 nm with an absorbance peak of 0.8 (a.u.). The nominal nanoparticle diameter was estimated at 35.1 nm, which is consistent with preliminary results with non-radioactive nanoparticles. The estimated extinction coefficient was $8.45 \times 10^9 \text{ M cm}^{-1}$. Based on the Beer-Lambert equation, the resulting nanoparticle concentration was estimated at $5.7 \times 10^{10} \text{ cm}^{-3}$. The total number of radioactive atoms in the nanoparticles was $3.88 \times 10^{10} \text{ cm}^{-3}$, which corresponds to a nominal μ of 1.47. The resulting distribution of radioactive atoms per nanoparticle is given in figure 28.

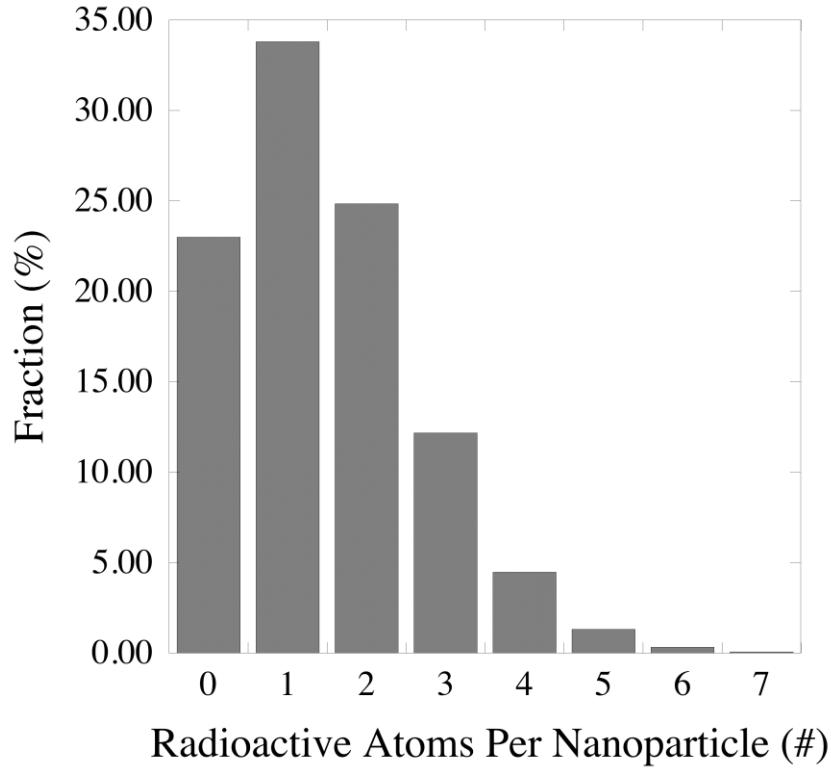


Figure 28. Distribution of radioactive atoms per nanoparticle based on a nominal mean of $\mu = 1.47$. The fraction of nanoparticles with no radioactive atoms was 0.23, and the fraction with one or more radioactive atoms was 0.77.

3.9. Characterization of Nebulizer

As previously mentioned, the mesh nebulizer used in this mouse nebulization system had a mass median aerodynamic diameter (MMAD) of 2.171 with a geometric standard deviation (GSD) of 2.037, which was obtained utilizing a next generation impactor (NGI). Therefore, using the Hatch and Choate Relations:

$$d_{median}^{(q)} = d_{median}^{(1)} \exp(q \ln^2 \sigma_g) \quad (8)$$

Where $d_{median}^{(q)}$ is the median diameter property distributed as, d^q , q is the power of the diameter, σ_g is our previous GSD, $d_{median}^{(1)}$ is the number-median aerodynamic diameter

(NMAD), $d_{median}^{(2)}$ would be the surface-median aerodynamic diameter (SMAD) if that is the variable we want, and $d_{median}^{(2)}$ would be our MMAD. As such we would find our NMAD to be 18.6 nm and our SMAD would be 4.9 nm.

3.10. Mouse Nebulization Studies

Three days after nebulizing the AuNPs and Au-I-NPs the lungs were removed from the mice utilizing the fixation techniques previously described. Then, the lobes were separated as previously described in figure 18. These lobes were then fluorescently imaged using the Bruker In Vivo Xtreme (see Fig. 29). From these images, the backgrounds were removed and regions of interest were drawn around the lobes of the lungs and the pico-watts per mm^2 of tissue was calculated (see Table 2 and Table 3).

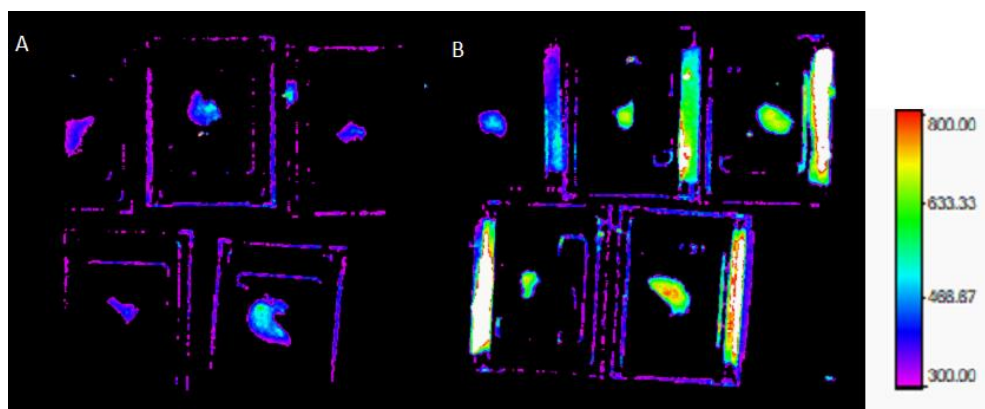


Figure 29. *Ex Vivo* imaging was performed on each lobe of the mouse lungs. In A and B, from top left to bottom right the lobes are arranged from superior lobe (SL1), middle lobe (ML2), inferior lobe (IL3), post-caval lobe (PCL4), and left lung (LL5). Signal of tape on right of each dish is reflectance. The settings were 690 nm for the excitation and 750 nm for emission. A is the control mouse and B is 170907F. These images were set to minimum intensity of 300 and a maximum intensity of 800.

Table 2. The distribution of signal in sum intensity or counts per square centimeter for each lobe of the lungs for each mouse examined in this study.

		SL1	ML2	IL3	PCL4	LL5
CONTROL		293922.6	405445.8	332659.0	286553.9	345523.0
AUNPS	170907A	397790.7	414527.9	415163.4	392458.5	581766.3
	170907F	278160.2	436514.5	461585.5	397083.4	482026.8
	170907K	275014.7	399729.6	440643.4	352617.8	464433.8
	170907I	316209.0	409341.6	381704.8	387199.4	515141.6
	Average	316793.7	415028.4	424774.3	382339.8	510842.1
	Standard Deviation	57151.5	15580.9	34420.1	20221.9	51745.4
AU-I-NPS	170907B	427237.6	538306.9	530122.7	420376.7	646817.7
	170907D	267803.0	406532.4	410993.1	355106.1	464449.3
	170907E	273900.4	405418.5	419299	385522.1	552831.0
	170907J	292009.8	396509.5	432024.3	385993.0	518675.7
	Average	315237.7	436691.8	448109.7	386749.5	545693.4
	Standard Deviation	75370.9	67891.7	55355.1	26671.8	76610.7

Table 3. The Sum of (Pico-Watts per square millimeter) signal normalized by the area in squared cm for each lobe, divided into AuNP or Au-I-NP delivery, of the lungs for each mouse examined in this study.

		SL1	ML2	IL3	PCL4	LL5
CONTROL		83.03988	114.5477	93.9838	80.95804	97.61817
AUNPS	170907A	112.385	117.1136	117.2932	110.8785	164.3623
	170907F	78.58665	123.3254	130.4085	112.1852	136.1836
	170907K	77.69798	112.9328	124.4919	99.62262	131.2132
	170907I	89.3363	115.6484	107.8404	109.3927	145.5393
	Average	89.50148	117.255	120.0085	108.0198	144.3246
	Standard Deviation	16.1466	4.40197	9.724484	5.713151	14.61927
AU-I-NPS	170907B	120.7044	152.084	149.7718	118.7661	182.7408
	170907D	75.6605	114.8547	116.115	100.3256	131.2176
	170907E	77.38314	114.54	118.4616	108.9188	156.1874
	170907J	82.49947	112.023	122.0568	109.0519	146.5378
	Average	89.06188	123.3754	126.6013	109.2656	154.1709
	Standard Deviation	21.29402	19.18097	15.6391	7.535422	21.6443

Table 2 and 3 seem to show that Cy5.5-PEG-Au-I-NPs and Cy5.5-PEG-AuNP had roughly the same signal. 170907B gave us the strongest signal intensity and best overall images for this mouse during confocal imaging, giving us the highest signal intensity as well. It is also apparent that some of the lobes like SL1 that some mice did not have measurable signals above the background (possibly due to attenuation). This was also apparent for SL1 for in figure 29.

After performing *ex vivo* imaging of the lung lobes they were frozen in OCT and sliced with the microtome. These slices were then placed on microscope slides and imaged with confocal microscopy. While signal was obtained from each of these slices, 2000 kilo counts per frame for the controls and 15000 to 30000 for the AuNPs and Au-I-NPs. It was not easy to discern the nanoparticles from the background in specific regions due to quenching of the signal intensity and the lifetime of the fluorescence, which seemed to be prolonged due to the presence of gold. As such, a multiarea time lapse was performed on the confocal imaging (See Fig. 30).

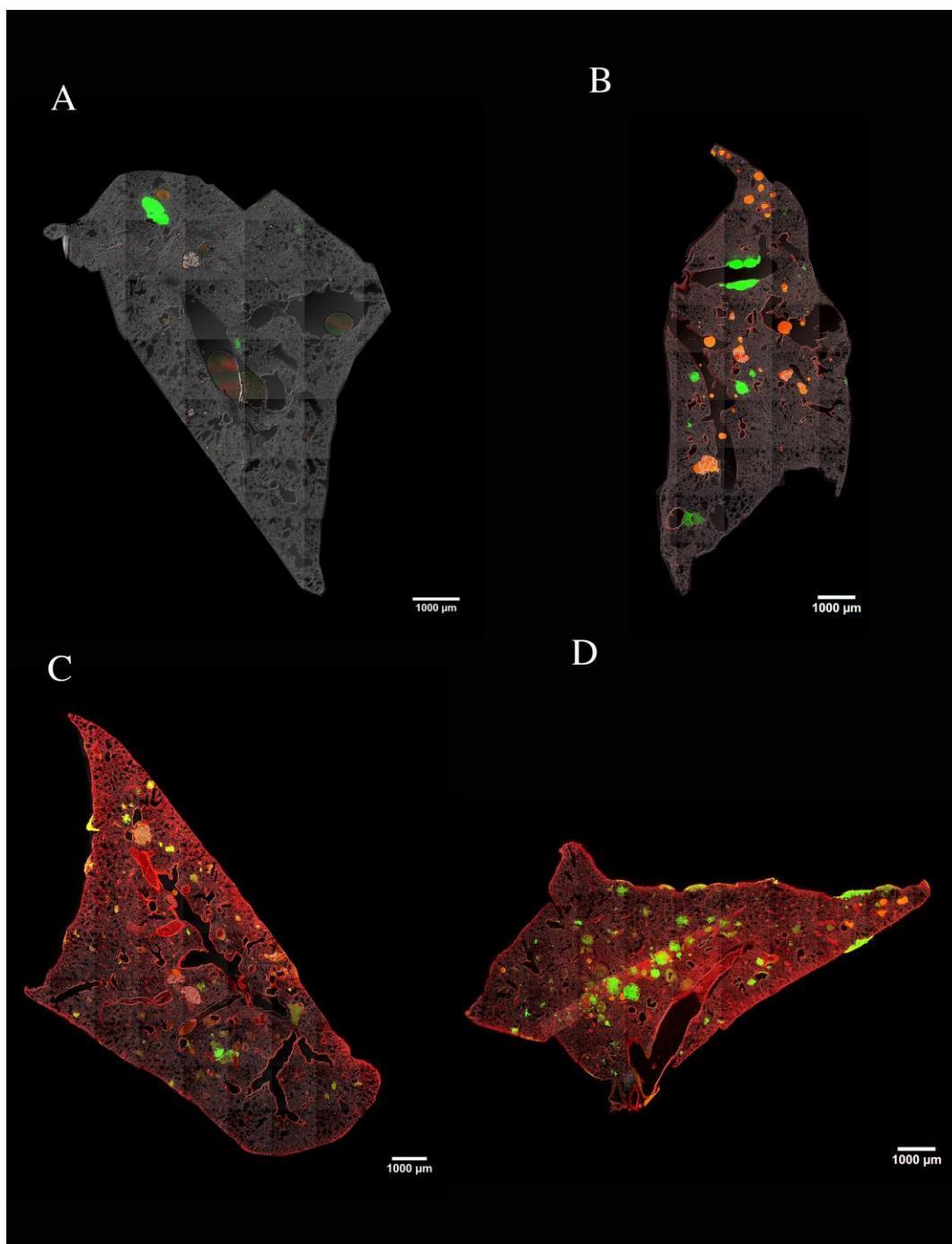


Figure 30. This figure depicts the multiarea time lapse of the left lung for (A) control with very low auto-fluorescence, (B) control with some auto-fluorescence/bubbles, (C) Cy5.5-PEG-Au-I-Nps, and (D) Cy5.5-PEG-AuNPs.

Figure 30 seems to indicate that Cy5.5 nanoparticles distribute throughout the entire left lung. The signal of the probe thus seems to contribute to an increased background signal everywhere and as such explains why regional deposits were not found. In each of these images the threshold counts for Cy5.5 fluorescence was set to a minimum of 200 and a maximum of 1300. As such, these images were obtained at the same settings. One key difference that was observed in these images is that there is a significant increase in signal along the periphery of the lungs, where not even auto-fluorescence was observed in the controls.

To further investigate and characterize the nebulizer system, micelles containing fluorescent probes were also imaged after nebulization and endotracheal delivery to show a divergence in regional intensity between the two. As such, we could characterize many features of the mouse nebulization system such as distribution in each lobe of the lungs (See Fig. 31) and even the previously utilized method (intratracheal delivery) versus nebulization delivery (See Fig. 32).

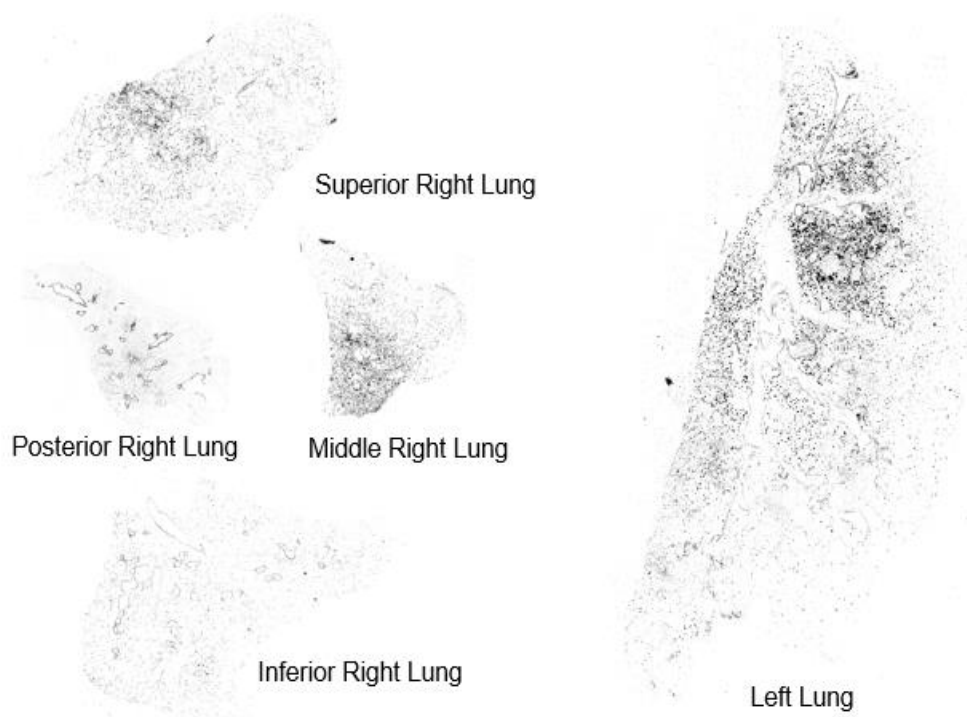


Figure 31. Confocal images of micelle dispersion in each of the 5 mouse lung lobes utilizing the mouse nebulizer system developed. As can be seen, the nebulizer system can deliver the micelles to every portion of the mouse lungs.



Figure 32. This is a side by side comparison of the mouse nebulization delivery technique compared to the previously performed method of intratracheal delivery. These are all the left lung and as can be observed results with the nebulization delivery were more repeatable and consistent than intratracheal delivery.

As can be seen from figure 31, the micelles were delivered to all 5 lobes of the mouse lungs. Figure 32 on the other hand shows that intratracheal delivery does not often deliver an even distribution and is often inconsistent, which would make it difficult to reach statistical significance in any chemotherapeutic efficacy study. Figure 32 is the left lung as well, which according to the AuNP study performed herein (see Table 2), often gets 1.5 to 2 times the dose per square centimeter as any other lobe of the mouse lungs.

CHAPTER IV

DISCUSSION AND FUTURE WORK

The goal of this dissertation was to develop nanoparticle based theranostic agents for the treatment and diagnosis of cancer. As such, we have developed three means of treating radiologically and imaging via SPECT. We have also developed a fourth technique that could be synthesized similarly to the previously utilized radionuclides but can be used for optical imaging instead. This is because optical imaging is one of the best techniques for imaging cancer metastases in mice. We were also able to develop a mouse nebulizer system capable of delivering nanoparticles to the mouse lungs, whether they be radionuclides or modified chemotherapeutics. As such, this should enhance preclinical studies and further enhance testing of new drugs with a superior delivery method to intratracheal delivery.

Regarding the AuNPs that were produced utilizing a modified Turkevich method. The RTCA system found that bare non-radioactive AuNPs have negligible or no cytotoxicity on SKBr-3 cells, in the short-term, as this study was only over a few days. A very high concentration of AuNPs were utilized and no noticeable difference in cell growth was detected among the different well cultures and controls.

It is important to mention that ^{198}Au NPs synthesized, along with the other nanoparticles synthesized, are considered protracted forms of irradiation and treatment like chemotherapeutics. The results from ^{198}Au NPs experiments showed that radioactive

nanoparticles may be used as a potential strategy for the treatment of metastatic cancer since a small response was observed at 1000 and 1500 kBq. Future studies would need to be carried out to determine the proper therapeutic doses to a tumor. Otherwise, we question the effective internalization of $^{198}\text{AuNPS-HIV-1 Tat}$ and further studies are required to assess if internalization was 1) limited by nanoparticle size, 2) by number of HIV-1 Tat cell penetrating peptide (CPP) per nanoparticle, 3) by radiation effects on cell cycle, or 4) lack of directionality of the HIV-1 Tat CPP against the cell surface. Other items to consider are the pharmacokinetics, clearance, and retention of nanoparticles via internalization into cells and whether the “cross-fire” effect mitigates the efficacy of using CPPs to bring radioisotopes closer to core components of the cell. One must also consider that AuNPs are believed to be internalized by some means of specialized endocytosis or micropinocytosis, so the degree of endocytosis at the concentration of HIV-1 TAT used may not be significant enough to cause significant differences.

Furthermore, it may be beneficial to have the radionuclides on the cell membranes as aldehydes produced via lipid peroxidation on the cell membrane may be playing a key role in the DNA damage and senescence. Both ROS and radiation damage correlate with the damage induced by aldehydes as well except that aldehydes have been shown to have a preference for other lipids (to produce even more aldehydes) and the DNA (Vaca, Wilhelm, and Harms-Ringdahl 1988). Aldehyde production has also been recently shown to be the potential key to radiation-induced senescence, which would be a major component in cancer treatment (Flor, Doshi, and Kron 2016). Nonetheless, we could

potentially observe a slight gain in cytotoxicity by the $^{198}\text{AuNPs-HIV-1 Tat}$ when compared with $^{198}\text{AuNPs}$ alone when pharmacokinetics and clearance are taken into consideration.

This dissertation also verified that the aggregation of gold by iodine occurs faster than the formation of stabilized gold nanoparticles if the iodine/iodide is added too early in the synthesis procedure (Cheng, Dong, and Wang 2003; Daniel and Astruc 2004; Kim et al. 2012). Iodine/iodide is faster than sodium citrate at reducing the surface potential of gold clusters. Therefore, the kinetics of iodine/iodide-induced AuNP aggregation by reducing the surface potentials was investigated as a potential avenue for determination of the rate-limiting step, in order to prevent the rapid aggregation of gold nanoparticles after the addition of iodine/iodide. The rate-limiting step was determined to occur between 35 and 55 seconds. A threshold of 50 s was utilized to produce aggregation free synthesis of ^{125}I -integrated AuNPs in our experiment. This was the time component for which iodine/iodide could be added without severely effecting the formation of the nanoparticles. The potential mechanisms of the synthesis and aggregation of AuNPs are presented in figure 33.

We suggest that at the time range selected (~50 seconds), the gold nanoparticles were approximately midway stabilized in terms of their surface potentials, and that the addition of iodine caused the aggregation of smaller nanoclusters around the iodine to form the ^{125}I integrated nanoparticle. This hypothesis is believed to be supported by a

distinct peak at approximately 95 seconds which could indicate that when gold nanoparticles are still undergoing the formation process, iodine could cause the aggregation of almost completely stabilized nanoclusters into larger than normal nanoparticles. Our results further indicated that at approximately 120 seconds the nanoparticles were completely formed, and thus iodine addition merely interacted with the surface of the nanoparticles, not significantly affecting the stabilization of the nanoparticles. This was substantiated by the color change in the solution to a wine-red color, which is characteristic of fully formed gold nanoparticles produced even in the absence of reducing iodide. In contrast, with the addition of iodine at any time after the addition of sodium citrate, the switch to a wine-red color was immediate, which would characterize rapid aggregation.

The ^{125}I integrated AuNPs were arduous to synthesize since instead of the concentration of iodide (I^-) being equal to the concentration of sodium (NaI) in 1×10^{-5} M NaOH as performed before to obtain stability variations over time, the radionuclide used in the second synthesis was iodine ($^{125}\text{I}_2$) gas bubbled through 1×10^{-5} M NaOH. Therefore, the ^{125}I integrated AuNP synthesis was significantly hindered by the limited amount of sodium, which is a potent stabilizing agent. The reduced quantity of Na, made the iodine injection at a time where the AuNPs were midway stabilized a key component in the prevention of iodine-induced aggregation (Polte et al. 2010). Another hypothesis is that the increased concentration of sodium prevents long chains or clusters of polyiodides or polyiodines from forming. This was supported by a second observation in which a 5 mCi

concentration of iodine in 1×10^{-5} M NaOH was utilized and found difficult to use even when readjusted to the concentrations used in the 2 mCi samples, potentially indicating that the clusters were already formed. Another item to consider is that the electronegativity of all isotopes of an element may not be the same; especially for a radioisotope that may have the propensity to increase or decrease its electronegativity to compensate for emissions during decay. Changes in electronegativity between isotopes have been observed using NMR and chemical reactions with carbon and hydrogen isotopes (Gombler 1982; Wolfsberg 2002). Under such conditions, it would thus seem plausible that ^{125}I has a different electronegativity from other iodine isotopes. When a particle is excited and about to decay it is assumed that the nucleus is in flux, therefore there is bound to be fluctuations in how the nucleus holds on to orbiting electrons as the localization of protons in the nucleus changes to counteract changes in the electron cloud.

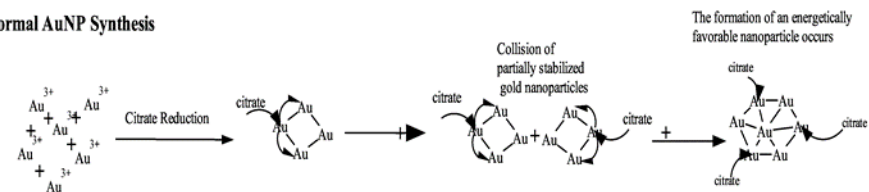
Making the iodine/iodide indistinguishable from background or noise brought about by the sheer quantity of other elements in the nanoparticles, proved to be difficult.

However, centrifugation with and without a nanopore filter showed that the iodine was indeed associated with the nanoparticles and not free in the solution. The relative stability at high temperatures and lack of noticeable aggregation with this protocol in contrast to addition of iodine in the beginning of synthesis or after synthesis would also seem to suggest different types of interactions, which are discussed in this paper and hypothesized in figure 33. However, this process will hopefully be further improved and

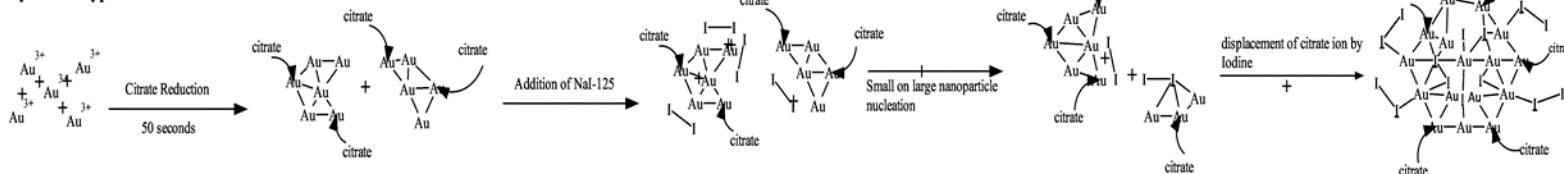
repeatability further enhanced with microcontrollers, which were being designed for

²¹¹At incorporation into AuNPs.

Normal AuNP Synthesis



Synthesis Hypothesis #1



Synthesis Hypothesis #2

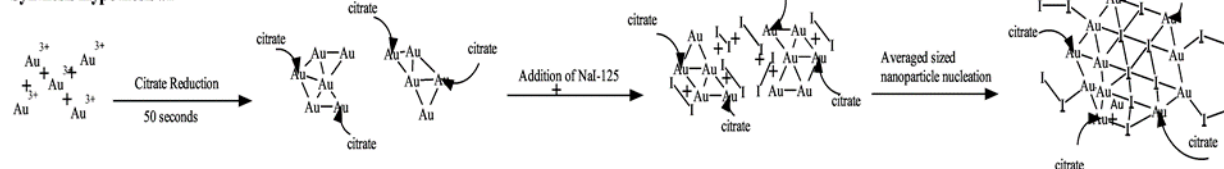


Figure 33. Proposed mechanisms of integration into gold nanoparticles occurring via collisions of iodine induced citrate displaced regions. Collisions could potentially occur between averaged sized nanoparticles or smaller nanoparticles on larger nanoparticles. The lines depict interactions with neighboring molecules. Reprinted with permission (Clanton et al. 2017).

The TEM images revealed clusters of aggregated AuNPs, possibly bonded together by iodine (see Fig. 26). Many of the nanoparticles were ovoid instead of spherical as well. This suggests the formation of gold nanoparticles to be a kinetics based situation with a threshold at which there is a small range of partially formed nanoparticles with a small variance in size. This data seems to suggest that those nanoparticles that are on the upper scale of that range could collide and create larger than average nanoparticles; this is especially true when iodine/iodide reduces the surface potentials of these nanoparticles, and as a result less energy is needed for collisions to occur. One of the most interesting aspects of figure 26 that could support this, is that the nanoparticles with the darkest cores at the center of the image, are the most aggregated or “attracted” to each other.

AuNPs have varying degrees of effectiveness in targeting tumors depending on their size. This phenomenon exists because there is a slow accumulation of the AuNPs in the tumor from circulating blood; this requires AuNPs to be small (~20 nm), given that they will be cleared more slowly from the blood than larger nanoparticles (~80 nm) which are more effectively cleared by the liver and spleen than the smaller nanoparticles (Zhang et al. 2009). Their biodistribution substantiates the previously discussed assessment that nanoparticles can target phagocytic cells since this uptake or clearance seems to stipulate that the reticuloendothelial system (also called the mononuclear phagocyte system or macrophage system) is involved (Mkandawire et al. 2015; Chang et al. 2008). With the mentioning of macrophages, the author would also like remind the readers of when Virchow first noticed the infiltration of inflammatory cells into tumors and that certain

subsets of cancer cells have been shown to express or present macrophage antigens as well (Lazova, Chakraborty, and Pawelek 2011; Powell et al. 2011; Shabo and Svanvik 2011). This presence of phagocytic cells in a tumor population just like those in the spleen and the liver would seem erroneous to ignore when it comes to AuNP retention within the neoplasm.

Furthermore, even though a small amount of the nanoparticles may go to the kidneys, conclusive evidence of cytotoxicity has not been shown in this organ or tissues, such as the liver. Even with low to moderate cytotoxicity being possible, excretion does occur slowly over time. Therefore, moderate inflammation and apoptosis should be rather short lived but further investigation would be prudent (You et al. 2014; Patra et al. 2007; Cho et al. 2009). Cytotoxicity would most likely be dependent on the size and the ability of nanoparticles to leave vesicles or interfere with transporters. Since the 20 nm AuNPs have longer retention times in the blood, they would be expected to show longer mean residence times, longer terminal elimination half-lives, and lower total body clearance, which should result in increased levels of accumulation in the tumor due to EPR (Zhang et al. 2009).

The actual concentrations retained in each tissue may fluctuate widely as the size increases from 1 nm to 80 nm diameters. For example, 50 nm, the size of spherical viruses with the highest transduction activities, has also been shown to be the diameter at which NPs are most highly up-taken by mammalian cells (Chithrani and Chan 2007).

Therefore, further assessment would need to include endocytosis, exocytosis, clearance from the blood, and uptake into target cells of interest to determine the appropriate therapeutic diameter for the nanoparticles. Although the nanoparticles in this experiment are less than the optimal size for cellular intake, based on the previously stated studies they should reside in the blood considerable longer (less uptake by spleen or liver and more leakage into the neoplasm), potentially increasing chances of targeting CTCs and sites of metastasis, which would be a more appropriate approach to avoid complications from treatment. Once these are taken into consideration and their values found, the ^{125}I integrated AuNPs can be assessed for the concentration needed to obtain similar therapeutic results to other treatments, or in other words its relative biological effectiveness.

While ^{125}I has been used routinely for seed brachytherapy, it is important to note that the radiotoxicity of ^{125}I and other Auger electron emitters have been shown to have a large dependence on their subcellular distribution and thus seeds are an inefficient means of utilizing these isotopes (Narra et al. 1992). Using centrifugation and redistribution, we have been able to accomplish 90-100 μCi within a 100 μl solution. This would equate to 3,700,000 Bq and if each decay equates to 106 cGy within a 2nm radius, as previously mentioned, then this would become 3,922,000 Gy potentially distributed within 7400 μm or 0.75 cm if uniformly dispersed. However, we know this is not true and nanoparticles will mostly be taken up by the more phagocytic cells. This contrasts with ^{125}I brachytherapy seeds, which are prescribed at 145-190 Gy over 150 seeds with

approximately 0.4 to 0.5 mCi of activity each. However, not all tumor treatments require 150 seeds to be implanted since. The activity and prescription of seeds would be determined to fit the clinical context. These seeds having a titanium coating blocking the Auger electrons and thus are only obtaining exposure from gamma rays. Another major difference between these liquid brachytherapy nanoparticles versus the typical seed brachytherapy is that these nanoparticles can be delivered at different intervals like chemotherapy and in conjunction with other treatments. Thus 600 injections of the nanoparticles may appear to be needed but this would be an erroneous comparison since the radiotoxicity of ^{125}I appears to be dependent on subcellular distribution and Auger electrons, which can't be accomplished with seeds as they are now. However, seeds do have an advantage in spatial positioning and non-dependence on a universal target, which to this date still hasn't been identified.

^{211}At was easily added at the very beginning of the synthesis, which is probably due to its lower electronegativity. Before, considerable cytotoxicity studies can be performed a means of automation to produce ^{211}At is needed. Then, long-term studies would need to be performed *in vivo* to ascertain whether the well-known effectiveness of targeted therapies using ^{211}At overcome any toxicity and long-term effects in the body, which have been poorly quantified.

Cy5.5-PEG-AuNPs and Cy5.5-PEG-Au-I-NPs both had fluorescent signals even though they were significantly quenched by the AuNPs. Since this quenching seems to depend

on distance, future studies would need to look at using different kDa sizes for the PEG chains. While not significant, it does appear that Au-I-NPs put off a stronger fluorescent signal, which is strange since iodine can also quench the fluorescent signal. One hypothesis that will need to be examined is that iodine may compete with the thiol groups on PEG in binding to AuNPs. As such, there may indeed be more quantities of free Cy5.5-PEG-thiol that is contributing to a higher signal intensity.

The mouse nose-only nebulization system was effective at delivering fluorescent probes to the lungs of the mice. Dr. Wooley's lab has been using the system for a couple months now and they have found that they get more of their chemotherapeutic drugs delivered to the lung metastases using this method and repeatedly have obtained more statistically significant results. Since their mice are immunosuppressed and very fragile they were previously losing one in four mice every time they used the previous intratracheal delivery. They have not lost a single mouse since incorporating my nebulization system. In the future, further development of the system will occur such as incorporation of a removal port to recollect some of the nebulized drugs that don't make it to the mouse lungs, replacing the anesthesia gas with an O₂/CO₂ mixture that will increase the breathing rate and instead using anesthesia injections, and enhancement of the enclosure system to further prevent leakage of drug or imaging probe nebulized.

Furthermore, the delivery of long-lived radionuclides, like ¹²⁵I, to the lungs would be the next pursuit as well since short-lived radionuclides like ¹⁸F may not be possible with this

technique due to the multiple doses that may be required and the limited amount that can be delivered due to regulations. However, recollection and redelivery may surpass this limitation. Right now, dimerized paclitaxel and brush polymers are also being investigated with the nebulizer with some of the imaging results presented herein.

The major component that will need to be investigated further is the co-localization of tumor and AuNPs. Unlike vascular delivery that results in AuNP removal from circulation and retention in the tumor within three days, signal was still seen throughout the entire lungs, including the tumor without much evidence of a biased signal toward the tumor. Since other nanoparticles, like brush polymers, can sit in the lungs for months, this may be a unique characteristic of the lungs itself. A long-term study would need to be performed to discern if the EPR effect occurs in the lungs. Furthermore, drugs and imaging probes may need to be developed that only work once they reach the tumor. This is what occurs with the dimerized paclitaxel as it only becomes active in the presence of glutathione and the brush polymers only break down in the presence of proteases (both increased in the tumor microenvironment). My thoughts are to use gold again but this time completely quenching the fluorescent signal. However, the fluorescent probe will now have components sensitive to proteases, glutathione, or acidity (limited since a significant amount of the probes reach the stomach) that cleave the fluorescent probe and/or drug in the tumor microenvironment. This may also be accomplished with my previous idea of inoculating the tumor with microbes and using AuNPs coated in microbial substrates to break down the substrate and free the drugs and

fluorescent probes. For radionuclides for therapy, I am suggesting a degradable shell that captures most of the emissions until the presence of the tumor microenvironment breaks down that shell, thus allowing macropinocytosis and/or the emissions to interact with and cause damage to the cell.

CHAPTER V

CONCLUSIONS

There is potential in creating novel cancer treatments by combining Targeted Radionuclide Therapy (TRT) and nuclear nanotechnology. As such, the use of nuclear nanotechnologies, where the nanoparticle core can serve as complex carriers of not only radionuclides but chemotherapeutics as well. However, with radionuclides alone this would yield new radiography agents with potentially higher safety and efficacy profile than those currently used clinically. Even combining radiosensitizing chemotherapeutic drugs with radioisotope integrated AuNPs would open a completely new avenue of research that has only recently began to be investigated (Zhao, Zhou, and Li 2016).

In terms of ^{198}Au and (^{198}Au - ^{197}Au) we could determine that it is quite feasible to produce nanoparticles with a therapeutic quantity of radionuclides. This method itself was shown to be capable yielding a good mono-dispersed population of AuNPs with an average diameter 32.9 nm. SKBR3 tumor cells were targeted with HIV-1 Tat cell penetrating peptide as an initial proof of principle. While the results didn't necessarily show increased efficacy an in-vivo model may show enhanced attachment to micrometastases versus nontargeted nanoparticles. The cell growth results showed a clear dependence on the activity administered, with response appearing to only occur above 1000 and 1500 kBq per well, for both functionalized and non-functionalized ^{198}Au , at least within the time frame measured.

Regarding the iodine integrated AuNPs. Due to the strong interactions between ^{125}I ions and gold, as well as iodine's ability to displace citrate groups stabilizing the surfaces of the gold nanoparticles, it is proposed that iodine will be preferentially added to the sides of the nanoparticles that are not completely stabilized by citrates during synthesis. Consequently, the gold nanoparticles will aggregate in areas where iodine has displaced the citrates; this conclusion can also be inferred by the figures produced by Figuerola and colleagues (Figuerola et al. 2009). As a result, a "layering" effect potentially occurs as the nanoparticles are forming. If this is true for normal conditions in which the nanoparticles are already formed and coated, then it is applicable that collisions will also occur where iodines (I_2) and/or iodides (I^-) are being integrated into the matrix of the forming nanoparticles. This would hypothetically create layered materials or ovular nanoparticles as previously suggested in figure 26. Whether iodine atoms get re-shuttled to the surface is questionable but it is suggested to be highly unlikely if polyiodides and/or polyiodines are formed and integrated into the gold nanoparticle structure in layers. There is no known literature precedence that would suggest that impurities can be re-shuttled to the surface in other studies. Since inclusion of iodine could potentially result in a more negative nanoparticle core, a larger concentration of reducing agent seems required to compensate. However, if the concentration of reducing agent is fully maximized or there are a maximum number of citrates on the surface of the nanoparticles, then increased stabilizing agents such as sodium are required to prevent aggregation. This conclusion was supported by the results obtained from our research.

This study demonstrates that there is indeed a kinetics process dominating the formation of gold nanoparticles. As such, future work involving the integration of AuNPs with radiohalogens will require careful attention to kinetic factors. Furthermore, this study also demonstrated the rapid synthesis of gold nanoparticles integrated with ^{125}I for diagnostics and therapeutics that have no statistically significant leaching from the nanoparticle. Subsequent testing showed that ionic solutions, such as boron tri-fluoride, were unable to remove the iodine from the gold nanoparticles. Consequently, there should thus be a higher uptake of the radionuclide in desired target tissues (Smith and Oates 2004).

Continuing with this concept of combining halides with AuNPs were also able to accomplish the combination of ^{211}At . This combination would potentially be a very effective route of treatment for several types of tumors, especially renal cancers and hepatocellular carcinomas (Paciotti, Kingston, and Tamarkin 2006). However, ^{211}At seemed to have no issue being added to the nanoparticles at least at the concentration of gold used in synthesis. This could be due to weaker electronegativity and as such a lower capability of causing an aggregation of nanoparticles during synthesis.

Combining these two ideas, radionuclides with AuNPs, allows for a treatment that not only helps prevent metastasis and proliferation via mitochondrial fusion but could also lead to a new paradigm in which the genetic information of both the mitochondria and nucleus are targeted by re-positioning them adjacently. With the addition of

functionalizing substances, certain apoptotic pathways can be targeted as well (Medine et al. 2011). Therefore, radionuclides integrated with AuNPs are applicable to treatment, due to their multi-faceted approach in preferentially targeting neoplastic cells with fragmented mitochondria or increased energy consumption. Furthermore, short ranged high-LET radiation along the cell membranes would be very powerful in inducing aldehyde formation, which would be very important for inducing senescence of the cancer stem cells (Zhang et al. 2016).

A main component of utilizing these radionuclides (I-125, Au-198, and As-211) is that they are theranostics; capable of being used therapeutically and diagnostically (imaging). The most promising feature of radionuclide integrated AuNPs, however, lies in the potential to image neoplasms while treatment is carried out. *In vivo* imaging is an important tool for preclinical studies of neoplasms and presently with particular interest on lung function and disease. This is because lung cancer is the leading cause of cancer-related deaths for both men and women throughout the developed world (Purandare and Rangarajan 2015). Therefore, to show that AuNPs were efficacious in delivering therapeutics (radionuclides or chemotherapeutics) and diagnostic probes (radionuclides or fluorescence) I was also able to develop a mouse nebulizer bed system with 3D printing technology. The nebulization system was more effective at evenly distributing nanoparticles throughout the entire lungs. This distribution was markedly different than the typical intratracheal delivery. Nebulization was also drastically safer resulting in zero

deaths during studies versus the approximately 1 in 4 deaths observed with every intratracheal delivery with these immunosuppressed mice.

Overall, the goal of this dissertation and doctorate work was to show the development of nanoparticles to be used for theranostic purposes, to deliver these compounds to the lungs of mice utilizing an aerosolizing modality, and to show what techniques could be used to characterize the compounds delivered to the mouse lungs qualitatively and quantitatively. These tasks were accomplished effectively and can be used for starting preclinical imaging and lung treatments at any facility.

REFERENCES

- Ackerman, M. E., D. Pawlowski, and K. D. Wittrup. 2008. 'Effect of antigen turnover rate and expression level on antibody penetration into tumor spheroids', *Mol Cancer Ther*, 7: 2233-40.
- Adinolfi, E., F. Amoroso, and A. L. Giuliani. 2012. 'P2X7 Receptor Function in Bone-Related Cancer', *J Osteoporos*, 2012: 637863.
- Agemy, L., A. Harmelin, T. Waks, I. Leibovitch, T. Rabin, M. R. Pfeffer, and Z. Eshhar. 2008. 'Irradiation enhances the metastatic potential of prostatic small cell carcinoma xenografts', *Prostate*, 68: 530-9.
- Akabani, G., S. J. Kennel, and M. R. Zalutsky. 2003. 'Microdosimetric analysis of alpha-particle-emitting targeted radiotherapeutics using histological images', *J Nucl Med*, 44: 792-805.
- Akabani, G., R. E. McLendon, D. D. Bigner, and M. R. Zalutsky. 2002. 'Vascular targeted endoradiotherapy of tumors using alpha-particle-emitting compounds: theoretical analysis', *Int J Radiat Oncol Biol Phys*, 54: 1259-75.
- Al-Hajj, M., M. S. Wicha, A. Benito-Hernandez, S. J. Morrison, and M. F. Clarke. 2003. 'Prospective identification of tumorigenic breast cancer cells', *Proc Natl Acad Sci U S A*, 100: 3983-8.
- Al Mahmoud, T., M. Mansour, J. Deschenes, C. Edelstein, M. Burnier, M. Marcil, G. Shenouda, C. Corriveau, and M. Evans. 2008. 'Iodine-125 radiotherapy for choroidal melanoma', *Ann N Y Acad Sci*, 1138: 15-8.

- Alessio, N., G. Esposito, G. Galano, R. De Rosa, P. Anello, G. Peluso, M. A. Tabocchini, and U. Galderisi. 2017. 'Irradiation of Mesenchymal Stromal Cells With Low and High Doses of Alpha Particles Induces Senescence and/or Apoptosis', *J Cell Biochem*, 118: 2993-3002.
- Alirol, E., and J. C. Martinou. 2006. 'Mitochondria and cancer: is there a morphological connection?', *Oncogene*, 25: 4706-16.
- Alvarez-Dolado, M., R. Pardal, J. M. Garcia-Verdugo, J. R. Fike, H. O. Lee, K. Pfeffer, C. Lois, S. J. Morrison, and A. Alvarez-Buylla. 2003. 'Fusion of bone-marrow-derived cells with Purkinje neurons, cardiomyocytes and hepatocytes', *Nature*, 425: 968-73.
- Amar, J., C. Chabo, A. Waget, P. Klopp, C. Vachoux, L. G. Bermudez-Humaran, N. Smirnova, M. Berge, T. Sulpice, S. Lahtinen, A. Ouwehand, P. Langella, N. Rautonen, P. J. Sansonetti, and R. Burcelin. 2011. 'Intestinal mucosal adherence and translocation of commensal bacteria at the early onset of type 2 diabetes: molecular mechanisms and probiotic treatment', *Embo Molecular Medicine*, 3: 559-72.
- Amariglio, Ninette, Abraham Hirshberg, Bernd W. Scheithauer, Yoram Cohen, Ron Loewenthal, Luba Trakhtenbrot, Nurit Paz, Maya Koren-Michowitz, Dalia Waldman, Leonor Leider-Trejo, Amos Toren, Shlomi Constantini, and Gideon Rechavi. 2009. 'Donor-Derived Brain Tumor Following Neural Stem Cell Transplantation in an Ataxia Telangiectasia Patient', *PLoS Med*, 6: e1000029.

- Ambudkar, S. V., Z. E. Sauna, M. M. Gottesman, and G. Szakacs. 2005. 'A novel way to spread drug resistance in tumor cells: functional intercellular transfer of P-glycoprotein (ABCB1)', *Trends Pharmacol Sci*, 26: 385-7.
- Anchordoquy, T. J., Y. Barenholz, D. Boraschi, M. Chorny, P. Decuzzi, M. A. Dobrovolskaia, Z. S. Farhangrazi, D. Farrell, A. Gabizon, H. Ghandehari, B. Godin, N. M. La-Beck, J. Ljubimova, S. M. Moghimi, L. Pagliaro, J. H. Park, D. Peer, E. Ruoslahti, N. J. Serkova, and D. Simberg. 2017. 'Mechanisms and Barriers in Cancer Nanomedicine: Addressing Challenges, Looking for Solutions', *ACS Nano*, 11: 12-18.
- Anjilvel, S., and B. Asgharian. 1995. 'A multiple-path model of particle deposition in the rat lung', *Fundam Appl Toxicol*, 28: 41-50.
- Apparatus, Harvard. 2017. 'Aerosol Nebulizers'.
http://www.harvardapparatus.co.uk/hapdfs/HAUK_DOCCAT_3/PY2_F_17.pdf.
- Arch, R., K. Wirth, M. Hofmann, H. Ponta, S. Matzku, P. Herrlich, and M. Zoller. 1992. 'Participation in normal immune responses of a metastasis-inducing splice variant of CD44', *Science*, 257: 682-5.
- Ari, A., and J. B. Fink. 2012. 'Breath-actuated nebulizer versus small-volume nebulizer: efficacy, safety, and satisfaction', *Respir Care*, 57: 1351-3.
- Ari, Arzu. 2014. 'Jet, Ultrasonic, and Mesh Nebulizers: An Evaluation of Nebulizers for Better Clinical Outcomes', *Eurasian Journal of Pulmonology*, 16: 1-7.

- Ari, Arzu, Hasan Areabi, and James B Fink. 2010. 'Evaluation of Aerosol Generator Devices at 3 Locations in Humidified and Non-humidified Circuits During Adult Mechanical Ventilation', *Respiratory Care*, 55: 837-44.
- Arkwright, P. D., F. Luchetti, J. Tour, C. Roberts, R. Ayub, A. P. Morales, J. J. Rodriguez, A. Gilmore, B. Canonico, S. Papa, and M. D. Esposti. 2010. 'Fas stimulation of T lymphocytes promotes rapid intercellular exchange of death signals via membrane nanotubes', *Cell Res*, 20: 72-88.
- Auletta, L., M. Gramanzini, S. Gargiulo, S. Albanese, M. Salvatore, and A. Greco. 2017. 'Advances in multimodal molecular imaging', *Q J Nucl Med Mol Imaging*, 61: 19-32.
- Aurlien, E., R. H. Larsen, G. Kvalheim, and O. S. Bruland. 2000. 'Demonstration of highly specific toxicity of the alpha-emitting radioimmunoconjugate(211)At-rituximab against non-Hodgkin's lymphoma cells', *Br J Cancer*, 83: 1375-9.
- Avin, E., J. Haimovich, and N. Hollander. 2004. 'Anti-idiotypic x anti-CD44 bispecific antibodies inhibit invasion of lymphoid organs by B cell lymphoma', *J Immunol*, 173: 4736-43.
- Azzam, E. I., S. M. de Toledo, and J. B. Little. 2003. 'Oxidative metabolism, gap junctions and the ionizing radiation-induced bystander effect', *Oncogene*, 22: 7050-7.
- Bagley, Rebecca G., and Beverly A. Teicher. 2009. *Stem cells and cancer* (Humana: Totowa, N.J.).

- Balagurumoorthy, P., X. Xu, K. Wang, S. J. Adelstein, and A. I. Kassis. 2012. 'Effect of distance between decaying (125)I and DNA on Auger-electron induced double-strand break yield', *Int J Radiat Biol*, 88: 998-1008.
- Balkwill, F., and A. Mantovani. 2001. 'Inflammation and cancer: back to Virchow?', *Lancet*, 357: 539-45.
- Bamburg, J. R., A. McGough, and S. Ono. 1999. 'Putting a new twist on actin: ADF/cofilins modulate actin dynamics', *Trends Cell Biol*, 9: 364-70.
- Bartczak, D., and A. G. Kanaras. 2011. 'Preparation of peptide-functionalized gold nanoparticles using one pot EDC/sulfo-NHS coupling', *Langmuir*, 27: 10119-23.
- Bennett, F. M., and S. M. Tenney. 1982. 'Comparative mechanics of mammalian respiratory system', *Respir Physiol*, 49: 131-40.
- Benseñor, Lorena B., Ho-Man Kan, Ningning Wang, Horst Wallrabe, Lance A. Davidson, Ying Cai, Dorothy A. Schafer, and George S. Bloom. 2007. 'IQGAP1 regulates cell motility by linking growth factor signaling to actin assembly', *Journal of Cell Science*, 120: 658-69.
- Berg, Rodney D. 1983. 'Bacterial translocation from the gastrointestinal tracts of mice receiving immunosuppressive chemotherapeutic agents', *Current Microbiology*, 8: 285-92.
- Beydoun, N., J. Bucci, and D. Malouf. 2014. 'Iodine-125 prostate seed brachytherapy in renal transplant recipients: an analysis of oncological outcomes and toxicity profile', *J Contemp Brachytherapy*, 6: 15-20.

- Biaglow, John E. 1981. 'The effects of ionizing radiation on mammalian cells', *Journal of Chemical Education*, 58: 144.
- Bjerkvig, R., B. B. Tysnes, K. S. Aboody, J. Najbauer, and A. J. Terzis. 2005. 'Opinion: the origin of the cancer stem cell: current controversies and new insights', *Nat Rev Cancer*, 5: 899-904.
- Black, K. C., Y. Wang, H. P. Luehmann, X. Cai, W. Xing, B. Pang, Y. Zhao, C. S. Cutler, L. V. Wang, Y. Liu, and Y. Xia. 2014. 'Radioactive ¹⁹⁸Au-doped nanostructures with different shapes for in vivo analyses of their biodistribution, tumor uptake, and intratumoral distribution', *ACS Nano*, 8: 4385-94.
- Bogdan, S., and C. Klambt. 2003. 'Kette regulates actin dynamics and genetically interacts with Wave and Wasp', *Development*, 130: 4427-37.
- Boleij, A., B. E. Dutilh, G. A. Kortman, R. Roelofs, C. M. Laarakkers, U. F. Engelke, and H. Tjalsma. 2012. 'Bacterial responses to a simulated colon tumor microenvironment', *Mol Cell Proteomics*, 11: 851-62.
- Bonnet, D., and J. E. Dick. 1997. 'Human acute myeloid leukemia is organized as a hierarchy that originates from a primitive hematopoietic cell', *Nat Med*, 3: 730-7.
- Bradley, E. W., P. C. Chan, and S. J. Adelstein. 1975. 'The radiotoxicity of iodine-125 in mammalian cells. I. Effects on the survival curve of radioiodine incorporated into DNA', *Radiat Res*, 64: 555-63.
- Braganza, M. Z., C. M. Kitahara, A. Berrington de Gonzalez, P. D. Inskip, K. J. Johnson, and P. Rajaraman. 2012. 'Ionizing radiation and the risk of brain and central nervous system tumors: a systematic review', *Neuro Oncol*, 14: 1316-24.

- Bruland, Øyvind S., Dahle Jostein, Dag Rune Olsen, and Roy H. Larsen. 2008. 'Targeted High-LET Therapy of Bone Metastases.' in Torgny Stigbrand, Jörgen Carlsson and Gregory P. Adams (eds.), *Targeted Radionuclide Tumor Therapy* (Springer Netherlands: Dordrecht).
- Bukoreshtliev, N. V., X. Wang, E. Hodneland, S. Gurke, J. F. Barroso, and H. H. Gerdes. 2009. 'Selective block of tunneling nanotube (TNT) formation inhibits intercellular organelle transfer between PC12 cells', *FEBS Lett*, 583: 1481-8.
- Cabiscol, E., J. Tamarit, and J. Ros. 2000. 'Oxidative stress in bacteria and protein damage by reactive oxygen species', *Int Microbiol*, 3: 3-8.
- Caldecott, K. W. 2008. 'Single-strand break repair and genetic disease', *Nat Rev Genet*, 9: 619-31.
- Cannone, F., G. Chirico, A. R. Bizzarri, and S. Cannistraro. 2006. 'Quenching and blinking of fluorescence of a single dye molecule bound to gold nanoparticles', *Journal of Physical Chemistry B*, 110: 16491-8.
- Carrier, M. F., V. Laurent, J. Santolini, R. Melki, D. Didry, G. X. Xia, Y. Hong, N. H. Chua, and D. Pantaloni. 1997. 'Actin depolymerizing factor (ADF/cofilin) enhances the rate of filament turnover: implication in actin-based motility', *J Cell Biol*, 136: 1307-22.
- Ceder, J., and J. Elgqvist. 2016. 'Targeting Prostate Cancer Stem Cells with Alpha-Particle Therapy', *Front Oncol*, 6: 273.
- Ceradini, Daniel J., Anita R. Kulkarni, Matthew J. Callaghan, Oren M. Tepper, Nicholas Bastidas, Mark E. Kleinman, Jennifer M. Capla, Robert D. Galiano, Jamie P.

- Levine, and Geoffrey C. Gurtner. 2004. 'Progenitor cell trafficking is regulated by hypoxic gradients through HIF-1 induction of SDF-1', *Nat Med*, 10: 858-64.
- Chandana, S. R., S. Movva, M. Arora, and T. Singh. 2008. 'Primary brain tumors in adults', *Am Fam Physician*, 77: 1423-30.
- Chang, M. Y., A. L. Shiau, Y. H. Chen, C. J. Chang, H. H. Chen, and C. L. Wu. 2008. 'Increased apoptotic potential and dose-enhancing effect of gold nanoparticles in combination with single-dose clinical electron beams on tumor-bearing mice', *Cancer Sci*, 99: 1479-84.
- Charafe-Jauffret, E., C. Ginestier, F. Iovino, C. Tarpin, M. Diebel, B. Esterni, G. Houvenaeghel, J. M. Extra, F. Bertucci, J. Jacquemier, L. Xerri, G. Dontu, G. Stassi, Y. Xiao, S. H. Barsky, D. Birnbaum, P. Viens, and M. S. Wicha. 2010. 'Aldehyde dehydrogenase 1-positive cancer stem cells mediate metastasis and poor clinical outcome in inflammatory breast cancer', *Clin Cancer Res*, 16: 45-55.
- Chen, A., M. Galloway, R. Landreneau, T. d'Amato, A. Colonias, S. Karlovits, A. Quinn, T. Santucci, S. Kalnicki, and D. Brown. 1999. 'Intraoperative 125I brachytherapy for high-risk stage I non-small cell lung carcinoma', *Int J Radiat Oncol Biol Phys*, 44: 1057-63.
- Chen, E. H., and E. N. Olson. 2005. 'Unveiling the mechanisms of cell-cell fusion', *Science*, 308: 369-73.

- Chen, K. A., P. E. Cruz, D. J. Lanuto, T. R. Flotte, D. R. Borchelt, A. Srivastava, J. Zhang, D. A. Steindler, and T. Zheng. 2011. 'Cellular fusion for gene delivery to SCA1 affected Purkinje neurons', *Mol Cell Neurosci*, 47: 61-70.
- Chen, S., Y. Zhao, G. Zhao, W. Han, L. Bao, K. N. Yu, and L. Wu. 2009. 'Up-regulation of ROS by mitochondria-dependent bystander signaling contributes to genotoxicity of bystander effects', *Mutat Res*, 666: 68-73.
- Chen, X., J. Qiu, D. Yang, J. Lu, C. Yan, X. Zha, and Y. Yin. 2013. 'MDM2 promotes invasion and metastasis in invasive ductal breast carcinoma by inducing matrix metalloproteinase-9', *PLoS One*, 8: e78794.
- Chen, Y. C., Y. W. Chen, H. S. Hsu, L. M. Tseng, P. I. Huang, K. H. Lu, D. T. Chen, L. K. Tai, M. C. Yung, S. C. Chang, H. H. Ku, S. H. Chiou, and W. L. Lo. 2009. 'Aldehyde dehydrogenase 1 is a putative marker for cancer stem cells in head and neck squamous cancer', *Biochem Biophys Res Commun*, 385: 307-13.
- Cheng, W., S. Dong, and E. Wang. 2003. 'Iodine-induced gold-nanoparticle fusion/fragmentation/aggregation and iodine-linked nanostructured assemblies on a glass substrate', *Angew Chem Int Ed Engl*, 42: 449-52.
- Chiozzi, P., J. M. Sanz, D. Ferrari, S. Falzoni, A. Aleotti, G. N. Buell, G. Collo, and F. Di Virgilio. 1997. 'Spontaneous cell fusion in macrophage cultures expressing high levels of the P2Z/P2X7 receptor', *Journal of Cell Biology*, 138: 697-706.
- Chithrani, B. D., and W. C. Chan. 2007. 'Elucidating the mechanism of cellular uptake and removal of protein-coated gold nanoparticles of different sizes and shapes', *Nano Lett*, 7: 1542-50.

- Cho, W. S., M. Cho, J. Jeong, M. Choi, H. Y. Cho, B. S. Han, S. H. Kim, H. O. Kim, Y. T. Lim, B. H. Chung, and J. Jeong. 2009. 'Acute toxicity and pharmacokinetics of 13 nm-sized PEG-coated gold nanoparticles', *Toxicol Appl Pharmacol*, 236: 16-24.
- Chong, H. S., X. Ma, T. Le, B. Kwamena, D. E. Milenic, E. D. Brady, H. A. Song, and M. W. Brechbiel. 2008. 'Rational design and generation of a bimodal bifunctional ligand for antibody-targeted radiation cancer therapy', *J Med Chem*, 51: 118-25.
- Clanton, R., A. Gonzalez, S. Shankar, and G. Akabani. 2017. 'Rapid synthesis of 125I integrated gold nanoparticles for use in combined neoplasm imaging and targeted radionuclide therapy', *Appl Radiat Isot*, 131: 49-57.
- Clanton, R., D. Saucier, J. Ford, and G. Akabani. 2015. 'Microbial influences on hormesis, oncogenesis, and therapy: A review of the literature', *Environ Res*, 142: 239-56.
- Conde, J., A. Ambrosone, V. Sanz, Y. Hernandez, V. Marchesano, F. Tian, H. Child, C. C. Berry, M. R. Ibarra, P. V. Baptista, C. Tortiglione, and J. M. de la Fuente. 2012. 'Design of multifunctional gold nanoparticles for in vitro and in vivo gene silencing', *ACS Nano*, 6: 8316-24.
- Connor, E. E., J. Mwamuka, A. Gole, C. J. Murphy, and M. D. Wyatt. 2005. 'Gold nanoparticles are taken up by human cells but do not cause acute cytotoxicity', *Small*, 1: 325-7.
- Corrie, J. E., W. A. Ratcliffe, and J. S. Macpherson. 1981. 'Generally applicable 125 iodine-based radioimmunoassays for plasma progesterone', *Steroids*, 38: 709-17.

- Croce, C M. 1976. 'Loss of mouse chromosomes in somatic cell hybrids between HT-1080 human fibrosarcoma cells and mouse peritoneal macrophages', *Proceedings of the National Academy of Sciences*, 73: 3248-52.
- Cruje, C, and DB Chithrani. 2014. 'Polyethylene glycol density and length affects nanoparticle uptake by cancer cells', *J. Nanomed. Res.*, 1: 1-6.
- Cui, W., J. Z. Ke, Q. Zhang, H. Z. Ke, C. Chalouni, and A. Vignery. 2006. 'The intracellular domain of CD44 promotes the fusion of macrophages', *Blood*, 107: 796-805.
- Daniel, M. C., and D. Astruc. 2004. 'Gold nanoparticles: assembly, supramolecular chemistry, quantum-size-related properties, and applications toward biology, catalysis, and nanotechnology', *Chem Rev*, 104: 293-346.
- Darquenne, C., J. S. Fleming, I. Katz, A. R. Martin, J. Schroeter, O. S. Usmani, J. Venegas, and O. Schmid. 2016. 'Bridging the Gap Between Science and Clinical Efficacy: Physiology, Imaging, and Modeling of Aerosols in the Lung', *J Aerosol Med Pulm Drug Deliv*, 29: 107-26.
- de Mol, N. J., and M. J. Fischer. 2010. 'Surface plasmon resonance: a general introduction', *Methods Mol Biol*, 627: 1-14.
- DeAngelis, L. M. 2001. 'Brain tumors', *N Engl J Med*, 344: 114-23.
- Dhanani, J., J. F. Fraser, H. K. Chan, J. Rello, J. Cohen, and J. A. Roberts. 2016. 'Fundamentals of aerosol therapy in critical care', *Crit Care*, 20: 269.
- Dhand, R. 2002. 'Nebulizers that use a vibrating mesh or plate with multiple apertures to generate aerosol', *Respir Care*, 47: 1406-16; discussion 16-8.

- Dong, Peixin, Kazuki Nabeshima, Naoko Nishimura, Takehito Kawakami, Toru Hachisuga, Tatsuhiko Kawarabayashi, and Hiroshi Iwasaki. 2006. 'Overexpression and diffuse expression pattern of IQGAP1 at invasion fronts are independent prognostic parameters in ovarian carcinomas', *Cancer letters*, 243: 120-27.
- Du, Shangfeng, Kevin Kendall, Panteha Toloueinia, Yasamin Mehrabadi, Gaurav Gupta, and Jill Newton. 2012. 'Aggregation and adhesion of gold nanoparticles in phosphate buffered saline', *Journal of Nanoparticle Research*, 14: 758.
- Duffy, M. J., T. M. Maguire, A. Hill, E. McDermott, and N. O'Higgins. 2000. 'Metalloproteinases: role in breast carcinogenesis, invasion and metastasis', *Breast Cancer Res*, 2: 252-7.
- Dulkeith, E., A. C. Morteani, T. Niedereichholz, T. A. Klar, J. Feldmann, S. A. Levi, F. C. van Veggel, D. N. Reinhoudt, M. Moller, and D. I. Gittins. 2002. 'Fluorescence quenching of dye molecules near gold nanoparticles: radiative and nonradiative effects', *Phys Rev Lett*, 89: 203002.
- Dulkeith, E., T. Niedereichholz, T. A. Klar, J. Feldmann, G. von Plessen, D. I. Gittins, K. S. Mayya, and F. Caruso. 2004. 'Plasmon emission in photoexcited gold nanoparticles', *Physical Review B*, 70: 205424.
- Dyawanapelly, S., A. Kumar, and M. K. Chourasia. 2017. 'Lessons Learned from Gemcitabine: Impact of Therapeutic Carrier Systems and Gemcitabine's Drug Conjugates on Cancer Therapy', *Crit Rev Ther Drug Carrier Syst*, 34: 63-96.

- Eccles, Laura J., Peter O'Neill, and Martine E. Lomax. 2011. 'Delayed repair of radiation induced clustered DNA damage: Friend or foe?', *Mutat Res*, 711: 134-41.
- Emami, B., J. Lyman, A. Brown, L. Coia, M. Goitein, J. E. Munzenrider, B. Shank, L. J. Solin, and M. Wesson. 1991. 'Tolerance of normal tissue to therapeutic irradiation', *Int J Radiat Oncol Biol Phys*, 21: 109-22.
- Emlet, D. R., P. Gupta, M. Holgado-Madruga, C. A. Del Vecchio, S. S. Mitra, S. Y. Han, G. Li, K. C. Jensen, H. Vogel, L. W. Xu, S. S. Skirboll, and A. J. Wong. 2014. 'Targeting a glioblastoma cancer stem-cell population defined by EGF receptor variant III', *Cancer Res*, 74: 1238-49.
- Erdo, F., C. Buhle, J. Blunk, M. Hoehn, Y. Xia, B. Fleischmann, M. Focking, E. Kustermann, E. Kolossov, J. Hescheler, K. A. Hossmann, and T. Trapp. 2003. 'Host-dependent tumorigenesis of embryonic stem cell transplantation in experimental stroke', *J Cereb Blood Flow Metab*, 23: 780-5.
- Espejel, S., R. Romero, and A. Alvarez-Buylla. 2009. 'Radiation damage increases Purkinje neuron heterokaryons in neonatal cerebellum', *Ann Neurol*, 66: 100-9.
- Estornes, Y., F. Gay, J. C. Gevrey, S. Navoizat, M. Nejjari, J. Y. Scoazec, J. A. Chayvialle, J. C. Saurin, and J. Abello. 2007. 'Differential involvement of destrin and cofilin-1 in the control of invasive properties of Isreco1 human colon cancer cells', *Int J Cancer*, 121: 2162-71.
- Farkhani, S. M., A. Valizadeh, H. Karami, S. Mohammadi, N. Sohrabi, and F. Badrzadeh. 2014. 'Cell penetrating peptides: efficient vectors for delivery of

- nanoparticles, nanocarriers, therapeutic and diagnostic molecules', *Peptides*, 57: 78-94.
- Fearon, U., M. Canavan, M. Biniecka, and D. J. Veale. 2016. 'Hypoxia, mitochondrial dysfunction and synovial invasiveness in rheumatoid arthritis', *Nat Rev Rheumatol*, 12: 385-97.
- Fernandez Tena, A., and P. Casan Clara. 2012. 'Deposition of inhaled particles in the lungs', *Arch Bronconeumol*, 48: 240-6.
- Ferrandina, G., G. Bonanno, L. Pierelli, A. Perillo, A. Procoli, A. Mariotti, M. Corallo, E. Martinelli, S. Rutella, A. Paglia, G. Zannoni, S. Mancuso, and G. Scambia. 2008. 'Expression of CD133-1 and CD133-2 in ovarian cancer', *Int J Gynecol Cancer*, 18: 506-14.
- Figuerola, A., I. R. Franchini, A. Fiore, R. Mastria, A. Falqui, G. Bertoni, S. Bals, G. Van Tendeloo, S. Kudera, R. Cingolani, and L. Manna. 2009. 'End-to-End Assembly of Shape-Controlled Nanocrystals via a Nanowelding Approach Mediated by Gold Domains', *Adv Mater*, 21: 550-4.
- Flor, A. C., A. P. Doshi, and S. J. Kron. 2016. 'Modulation of therapy-induced senescence by reactive lipid aldehydes', *Cell Death Discov*, 2: 16045.
- Floren, A., I. Mager, and U. Langel. 2011. 'Uptake kinetics of cell-penetrating peptides', *Methods Mol Biol*, 683: 117-28.
- Food and Drug Administration. 2014. "Guidance for Industry: Considering Whether an FDA-Regulated Product Involves the Application of Nanotechnology." In.: FDA Maryland.

- Franken, N. A., H. M. Rodermond, J. Stap, J. Haveman, and C. van Bree. 2006. 'Clonogenic assay of cells in vitro', *Nat Protoc*, 1: 2315-9.
- Frens, G. 1973. 'Controlled Nucleation for Regulation of Particle-Size in Monodisperse Gold Suspensions', *Nature-Physical Science*, 241: 20-22.
- Friedlander, G., and W. C. Orr. 1951. 'The Decay of I125', *Physical Review*, 84: 484-86.
- Frohlich, E. 2012. 'The role of surface charge in cellular uptake and cytotoxicity of medical nanoparticles', *Int J Nanomedicine*, 7: 5577-91.
- Fujiwara, T., M. Bandi, M. Nitta, E. V. Ivanova, R. T. Bronson, and D. Pellman. 2005. 'Cytokinesis failure generating tetraploids promotes tumorigenesis in p53-null cells', *Nature*, 437: 1043-7.
- Garay, R. P., R. El-Gewely, J. K. Armstrong, G. Garratty, and P. Richette. 2012. 'Antibodies against polyethylene glycol in healthy subjects and in patients treated with PEG-conjugated agents', *Expert Opin Drug Deliv*, 9: 1319-23.
- Garrastazu Pereira, G., A. J. Lawson, F. Buttini, and F. Sonvico. 2016. 'Loco-regional administration of nanomedicines for the treatment of lung cancer', *Drug Deliv*, 23: 2881-96.
- Garretson, B. R., D. M. Robertson, and J. D. Earle. 1987. 'Choroidal melanoma treatment with iodine 125 brachytherapy', *Arch Ophthalmol*, 105: 1394-7.
- Gaspar, L. E., L. J. Zamorano, F. Shamsa, J. Fontanesi, G. E. Ezzell, and D. A. Yakar. 1999. 'Permanent 125iodine implants for recurrent malignant gliomas', *Int J Radiat Oncol Biol Phys*, 43: 977-82.

- Geiser, M., and W. G. Kreyling. 2010. 'Deposition and biokinetics of inhaled nanoparticles', *Part Fibre Toxicol*, 7: 2.
- Gelmini, S., M. Mangoni, M. Serio, P. Romagnani, and E. Lazzeri. 2008. 'The critical role of SDF-1/CXCR4 axis in cancer and cancer stem cells metastasis', *Journal of Endocrinological Investigation*, 31: 809-19.
- Gendron, Renée, Daniel Grenier, and Léo-François Maheu-Robert. 2000. 'The oral cavity as a reservoir of bacterial pathogens for focal infections', *Microbes and Infection*, 2: 897-906.
- Gerdes, H. H., N. V. Bukoreshtliev, and J. F. Barroso. 2007. 'Tunneling nanotubes: a new route for the exchange of components between animal cells', *FEBS Lett*, 581: 2194-201.
- Ghani, F. I., H. Yamazaki, S. Iwata, T. Okamoto, K. Aoe, K. Okabe, Y. Mimura, N. Fujimoto, T. Kishimoto, T. Yamada, C. W. Xu, and C. Morimoto. 2011. 'Identification of cancer stem cell markers in human malignant mesothelioma cells', *Biochem Biophys Res Commun*, 404: 735-42.
- Ghosh, P., G. Han, M. De, C. K. Kim, and V. M. Rotello. 2008. 'Gold nanoparticles in delivery applications', *Adv Drug Deliv Rev*, 60: 1307-15.
- Goddard, C. P., A. H. Stead, P. A. Mason, B. Law, A. C. Moffat, M. McBrien, and S. Cosby. 1986. 'An iodine-125 radioimmunoassay for the direct detection of benzodiazepines in blood and urine', *Analyst*, 111: 525-9.
- Gomblér, Willy. 1982. 'NMR spectroscopic studies on chalcogen compounds. 4. Carbon-13 isotope effect on selenium-77 and tellurium-125 nuclear shielding and

- its correlation with carbon-selenium bond distances. Tellurium-123 isotope effect on tellurium-125 nuclear shielding', *J Am Chem Soc*, 104: 6616-20.
- Gomes, R. F., and J. H. Bates. 2002. 'Geometric determinants of airway resistance in two isomorphic rodent species', *Respir Physiol Neurobiol*, 130: 317-25.
- Goswami, S., H. J. Pant, J. Biswal, J. S. Samantray, V. K. Sharma, and A. Dash. 2016. 'Synthesis, characterization and application of Au-198 nanoparticles as radiotracer for industrial applications', *Appl Radiat Isot*, 111: 18-25.
- Grabham, P., and P. Sharma. 2013. 'The effects of radiation on angiogenesis', *Vasc Cell*, 5: 19.
- Greenwood, N. N., and A. Earnshaw. 1984. *Chemistry of the elements* (Pergamon Press: Oxford Oxfordshire ; New York).
- Gu, Qing, Yan He, Jianfeng Ji, Yifan Yao, Wenhao Shen, Jialin Luo, Wei Zhu, Han Cao, Yangyang Geng, Jing Xu, Shuyu Zhang, Jianping Cao, and Wei-Qun Ding. 2015. 'Hypoxia-inducible factor 1 α (HIF-1 α) and reactive oxygen species (ROS) mediates radiation-induced invasiveness through the SDF-1 α /CXCR4 pathway in non-small cell lung carcinoma cells', *Oncotarget*, 6.
- Guerard, F., J. F. Gestin, and M. W. Brechbiel. 2013. 'Production of [(211)At]-astatinated radiopharmaceuticals and applications in targeted alpha-particle therapy', *Cancer Biother Radiopharm*, 28: 1-20.
- Guo, Y., J. Ma, J. Wang, X. Che, J. Narula, M. Bigby, M. Wu, and M. S. Sy. 1994. 'Inhibition of human melanoma growth and metastasis in vivo by anti-CD44 monoclonal antibody', *Cancer Res*, 54: 1561-5.

- Gutin, P. H., T. L. Phillips, W. M. Wara, S. A. Leibel, Y. Hosobuchi, V. A. Levin, K. A. Weaver, and S. Lamb. 1984. 'Brachytherapy of recurrent malignant brain tumors with removable high-activity iodine-125 sources', *J Neurosurg*, 60: 61-8.
- Hadnagy, A., L. Gaboury, R. Beaulieu, and D. Balicki. 2006. 'SP analysis may be used to identify cancer stem cell populations', *Exp Cell Res*, 312: 3701-10.
- Hainfeld, J. F., D. N. Slatkin, T. M. Focella, and H. M. Smilowitz. 2006. 'Gold nanoparticles: a new X-ray contrast agent', *Br J Radiol*, 79: 248-53.
- Hainfeld, J. F., H. M. Smilowitz, M. J. O'Connor, F. A. Dilmanian, and D. N. Slatkin. 2013. 'Gold nanoparticle imaging and radiotherapy of brain tumors in mice', *Nanomedicine (Lond)*, 8: 1601-9.
- Hallbrink, M., A. Floren, A. Elmquist, M. Pooga, T. Bartfai, and U. Langel. 2001. 'Cargo delivery kinetics of cell-penetrating peptides', *Biochim Biophys Acta*, 1515: 101-9.
- Hamoui, Zaher Basel. 2015. 'In Vitro Cytotoxicity of ¹⁹⁸Au-NPs Labeled HIV-1 Tat CPP for the Treatment of Metastatic Breast Cancer', Texas A&M University.
- Han, X., F. Li, Z. Fang, Y. Gao, F. Li, R. Fang, S. Yao, Y. Sun, L. Li, W. Zhang, H. Ma, Q. Xiao, G. Ge, J. Fang, H. Wang, L. Zhang, K. K. Wong, H. Chen, Y. Hou, and H. Ji. 2014. 'Transdifferentiation of lung adenocarcinoma in mice with Lkb1 deficiency to squamous cell carcinoma', *Nat Commun*, 5: 3261.
- Hangleiter, A., and R. Hacker. 1990. 'Enhancement of band-to-band Auger recombination by electron-hole correlations', *Phys Rev Lett*, 65: 215-18.

- Haraguchi, N., H. Inoue, F. Tanaka, K. Mimori, T. Utsunomiya, A. Sasaki, and M. Mori. 2006. 'Cancer stem cells in human gastrointestinal cancers', *Hum Cell*, 19: 24-9.
- Harper, PV, WD Siemens, KA Lathrop, and H Endlicht. 1961. 'Production and use of iodine-125', *Argonne Cancer Res. Hosp. semi-ann. rep. to Atomic Energy Comm*, 15: 92-103.
- Hermann, P. C., S. L. Huber, T. Herrler, A. Aicher, J. W. Ellwart, M. Guba, C. J. Bruns, and C. Heeschen. 2007. 'Distinct populations of cancer stem cells determine tumor growth and metastatic activity in human pancreatic cancer', *Cell Stem Cell*, 1: 313-23.
- Heselmeyer, K., E. Schröck, S. du Manoir, H. Blegen, K. Shah, R. Steinbeck, G. Auer, and T. Ried. 1996. 'Gain of chromosome 3q defines the transition from severe dysplasia to invasive carcinoma of the uterine cervix', *Proc Natl Acad Sci U S A*, 93: 479-84.
- Hirschmann-Jax, C., A. E. Foster, G. G. Wulf, J. G. Nuchtern, T. W. Jax, U. Gobel, M. A. Goodell, and M. K. Brenner. 2004. 'A distinct "side population" of cells with high drug efflux capacity in human tumor cells', *Proc Natl Acad Sci U S A*, 101: 14228-33.
- Hofer, K. G. 1996. 'Biophysical aspects of Auger processes--A review', *Acta Oncol*, 35: 789-96.
- . 2000. 'Biophysical aspects of Auger processes', *Acta Oncol*, 39: 651-7.
- Hofer, K. G., and W. L. Hughes. 1971. 'Radiotoxicity of intranuclear tritium, 125 iodine and 131 iodine', *Radiat Res*, 47: 94-101.

Hofer, Kurt G, Nanette van Loon, Martin H Schneiderman, and David E Charlton. 1992.

'The Paradoxical Nature of DNA Damage and Cell Death Induced by¹²⁵I Decay', *Radiation Research*, 130: 121-24.

Hong, Wan Xing, Michael S. Hu, Mikaela Esquivel, Grace Y. Liang, Robert C. Rennert,

Adrian McArdle, Kevin J. Paik, Dominik Duscher, Geoffrey C. Gurtner, H. Peter Lorenz, and Michael T. Longaker. 2014. 'The Role of Hypoxia-Inducible Factor in Wound Healing', *Advances in Wound Care*, 3: 390-99.

Hoskin, P., and C. Coyle. 2011. *Radiotherapy in Practice - Brachytherapy* (OUP Oxford).

Huang, Y. C., Y. C. Yang, K. C. Yang, H. R. Shieh, T. Y. Wang, Y. Hwu, and Y. J.

Chen. 2014. 'Pegylated gold nanoparticles induce apoptosis in human chronic myeloid leukemia cells', *Biomed Res Int*, 2014: 182353.

Humm, John L., Roger W. Howell, and Dandamudi V. Rao. 1995. 'Erratum: "Dosimetry of Auger electron-emitting-radionuclides: Report No. 3 of AAPM Nuclear Medicine Task Group No. 6" [Med. Phys. 2

1

, 1901-1915 (1994)]', *Medical Physics*, 22: 1837-37.

Hussain, S. 2016. 'Nanomedicine for Treatment of Lung Cancer', *Adv Exp Med Biol*, 890: 137-47.

Iida, N., A. Dzutsev, C. A. Stewart, L. Smith, N. Bouladoux, R. A. Weingarten, D. A.

Molina, R. Salcedo, T. Back, S. Cramer, R. M. Dai, H. Kiu, M. Cardone, S. Naik,

- A. K. Patri, E. Wang, F. M. Marincola, K. M. Frank, Y. Belkaid, G. Trinchieri, and R. S. Goldszmid. 2013. 'Commensal bacteria control cancer response to therapy by modulating the tumor microenvironment', *Science*, 342: 967-70.
- Illmensee, K., and B. Mintz. 1976. 'Totipotency and normal differentiation of single teratocarcinoma cells cloned by injection into blastocysts', *Proc Natl Acad Sci U S A*, 73: 549-53.
- Imam, S. K. 2001a. 'Advancements in cancer therapy with alpha-emitters: a review', *Int J Radiat Oncol Biol Phys*, 51: 271-8.
- Imam, Seyed K. 2001b. 'Advancements in cancer therapy with alpha-emitters: a review', *International Journal of Radiation Oncology*Biology*Physics*, 51: 271-78.
- Innes, B. A., and J. R. Dorin. 2001. 'Submucosal gland distribution in the mouse has a genetic determination localized on chromosome 9', *Mamm Genome*, 12: 124-8.
- Irvin, C. G., and J. H. Bates. 2003. 'Measuring the lung function in the mouse: the challenge of size', *Respir Res*, 4: 4.
- Isawa, T., T. Teshima, T. Hirano, A. Ebina, M. Motomiya, and K. Konno. 1984. 'Lung clearance mechanisms in obstructive airways disease', *J Nucl Med*, 25: 447-54.
- Isawa, Toyoharu. 1994. "Nonrespiratory lung function." In, 64-87. International Atomic Energy Agency (IAEA).
- Ishii, Takehiko, Hidenori Otsuka, Kazunori Kataoka, and Yukio Nagasaki. 2004. 'Preparation of Functionally PEGylated Gold Nanoparticles with Narrow Distribution through Autoreduction of Auric Cation by α -Biotinyl-PEG-block-[poly(2-(N,N-dimethylamino)ethyl methacrylate)]', *Langmuir*, 20: 561-64.

- Iyer, R., C. C. Hsia, and K. T. Nguyen. 2015. 'Nano-Therapeutics for the Lung: State-of-the-Art and Future Perspectives', *Curr Pharm Des*, 21: 5233-44.
- Jacob, B., B.R. O'Driscoll, and J.H. Dennis. 2003. *Practical Handbook of Nebulizer Therapy* (Taylor & Francis).
- Jain, R. K. 1999. 'Transport of molecules, particles, and cells in solid tumors', *Annu Rev Biomed Eng*, 1: 241-63.
- Jay, S. M., E. A. Skokos, J. Zeng, K. Knox, and T. R. Kyriakides. 2010. 'Macrophage fusion leading to foreign body giant cell formation persists under phagocytic stimulation by microspheres in vitro and in vivo in mouse models', *J Biomed Mater Res A*, 93: 189-99.
- Jay, S. M., E. Skokos, F. Laiwalla, M. M. Krady, and T. R. Kyriakides. 2007. 'Foreign body giant cell formation is preceded by lamellipodia formation and can be attenuated by inhibition of Rac1 activation', *Am J Pathol*, 171: 632-40.
- Jiang, S., L. Walker, M. Afentoulis, D. A. Anderson, L. Jauron-Mills, C. L. Corless, and W. H. Fleming. 2004. 'Transplanted human bone marrow contributes to vascular endothelium', *Proc Natl Acad Sci U S A*, 101: 16891-6.
- Jin, L., K. J. Hope, Q. Zhai, F. Smadja-Joffe, and J. E. Dick. 2006. 'Targeting of CD44 eradicates human acute myeloid leukemic stem cells', *Nat Med*, 12: 1167-74.
- Jin, Qunyan, Wei Ding, and Kathleen M. Mulder. 2012. 'The TGF β Receptor-interacting Protein km23-1/DYNLRB1 Plays an Adaptor Role in TGF β 1 Autoinduction via Its Association with Ras', *Journal of Biological Chemistry*, 287: 26453-63.

- Jin, Qunyan, Nageswara R Pulipati, Weidong Zhou, Cory M Staub, Lance A Liotta, and Kathleen M Mulder. 2012. 'Role of km23-1 in RhoA/actin-based cell migration', *Biochemical and biophysical research communications*, 428: 333-38.
- Jing, S. W., Y. D. Wang, M. Kuroda, J. W. Su, G. G. Sun, Q. Liu, Y. J. Cheng, and C. R. Yang. 2012. 'HIF-1alpha contributes to hypoxia-induced invasion and metastasis of esophageal carcinoma via inhibiting E-cadherin and promoting MMP-2 expression', *Acta Med Okayama*, 66: 399-407.
- Johansson, C. B., S. Youssef, K. Koleckar, C. Holbrook, R. Doyonnas, S. Y. Corbel, L. Steinman, F. M. Rossi, and H. M. Blau. 2008. 'Extensive fusion of haematopoietic cells with Purkinje neurons in response to chronic inflammation', *Nat Cell Biol*, 10: 575-83.
- Joseph, Deepak, Raju K. Puttaswamy, and Hari Krovvidi. 2013. 'Non-respiratory functions of the lung', *Continuing Education in Anaesthesia, Critical Care & Pain*, 13: 98-102.
- Karamanos, N., D. Gullberg, H. Paraskevi, L. Schaefer, R. Tenni, A. Theocharis, and J.O. Winberg. 2012. *Extracellular Matrix: Pathobiology and Signaling* (De Gruyter).
- Karatas, O. F., E. Sezgin, O. Aydin, and M. Culha. 2009. 'Interaction of gold nanoparticles with mitochondria', *Colloids Surf B Biointerfaces*, 71: 315-8.
- Karnoub, Antoine E., Ajeeta B. Dash, Annie P. Vo, Andrew Sullivan, Mary W. Brooks, George W. Bell, Andrea L. Richardson, Kornelia Polyak, Ross Tubo, and Robert

- A. Weinberg. 2007. 'Mesenchymal stem cells within tumour stroma promote breast cancer metastasis', *Nature*, 449: 557-63.
- Kassis, A. I. 2004. 'The amazing world of auger electrons', *Int J Radiat Biol*, 80: 789-803.
- Kawashima, M., K. Doh-ura, E. Mekada, M. Fukui, and T. Iwaki. 2002. 'CD9 expression in solid non-neuroepithelial tumors and infiltrative astrocytic tumors', *J Histochem Cytochem*, 50: 1195-203.
- Kellar, A., C. Egan, and D. Morris. 2015. 'Preclinical Murine Models for Lung Cancer: Clinical Trial Applications', *Biomed Res Int*, 2015: 621324.
- Kemp, K., D. Gordon, D. C. Wraith, E. Mallam, E. Hartfield, J. Uney, A. Wilkins, and N. Scolding. 2011. 'Fusion between human mesenchymal stem cells and rodent cerebellar Purkinje cells', *Neuropathol Appl Neurobiol*, 37: 166-78.
- Kemp, K., A. Wilkins, and N. Scolding. 2014. 'Cell fusion in the brain: two cells forward, one cell back', *Acta Neuropathol*, 128: 629-38.
- Kemper, Kristel, Martin R Sprick, Martijn de Bree, Alessandro Scopelliti, Louis Vermeulen, Maarten Hoek, Jurrit Zeilstra, Steven T Pals, Huseyin Mehmet, and Giorgio Stassi. 2010. 'The AC133 epitope, but not the CD133 protein, is lost upon cancer stem cell differentiation', *Cancer research*, 70: 719-29.
- Kespichayawattana, W., S. Rattanachetkul, T. Wanun, P. Utaisinchaoen, and S. Sirisinha. 2000. 'Burkholderia pseudomallei induces cell fusion and actin-associated membrane protrusion: a possible mechanism for cell-to-cell spreading', *Infect Immun*, 68: 5377-84.

- Khan, M., Gowda, V. Siddaramaiah, H. 2011. 'Gold nanoparticles: A paradigm shift in biomedical applications', *Advances in Colloid and Interface Science*.
- Kiessling, F., S. Fokong, J. Bzyl, W. Lederle, M. Palmowski, and T. Lammers. 2014. 'Recent advances in molecular, multimodal and theranostic ultrasound imaging', *Adv Drug Deliv Rev*, 72: 15-27.
- Kim, Sun-Hee, Eun-Mi Kim, Chang-Moon Lee, Dong Wook Kim, Seok Tae Lim, Myung-Hee Sohn, and Hwan-Jeong Jeong. 2012. 'Synthesis of PEG-Iodine-Capped Gold Nanoparticles and Their Contrast Enhancement in In Vitro and In Vivo for X-Ray/CT', *Journal of Nanomaterials*, 2012: 1-9.
- Kimling, J., M. Maier, B. Okenve, V. Kotaidis, H. Ballot, and A. Plech. 2006. 'Turkevich method for gold nanoparticle synthesis revisited', *Journal of Physical Chemistry B*, 110: 15700-7.
- Kirkby, C., and E. Ghasroddashti. 2015. 'Targeting mitochondria in cancer cells using gold nanoparticle-enhanced radiotherapy: a Monte Carlo study', *Medical Physics*, 42: 1119-28.
- Kischel, P., A. Bellahcene, B. Deux, V. Lamour, R. Dobson, D. E. Pauw E, P. Clezardin, and V. Castronovo. 2012. 'Overexpression of CD9 in human breast cancer cells promotes the development of bone metastases', *Anticancer Res*, 32: 5211-20.
- Klose, Theresa, Ivane Abiatari, Tamar Samkharadze, Tiago De Oliveira, Carsten Jäger, Merab Kiladze, Nataliya Valkovskaya, Helmut Friess, Christoph W. Michalski, and Jörg Kleeff. 2012. 'The actin binding protein destrin is associated with growth and perineural invasion of pancreatic cancer', *Pancreatology*, 12: 350-57.

- Kogelnik, H. D. 1998. '[100 years radiotherapy. On the birth of a new specialty]', *Wien Klin Wochenschr*, 110: 313-20.
- Kozak, K. R., and J. S. Moody. 2009. 'Giant cell glioblastoma: a glioblastoma subtype with distinct epidemiology and superior prognosis', *Neuro Oncol*, 11: 833-41.
- Kucia, M., R. Reza, K. Miekus, J. Wanzeck, W. Wojakowski, A. Janowska-Wieczorek, J. Ratajczak, and M. Z. Ratajczak. 2005. 'Trafficking of normal stem cells and metastasis of cancer stem cells involve similar mechanisms: pivotal role of the SDF-1-CXCR4 axis', *Stem Cells*, 23: 879-94.
- Kukita, Toshio, Akira Takahashi, Jing-Qi Zhang, and Akiko Kukita. 2015. 'Membrane Nanotube Formation in Osteoclastogenesis.' in Kurt Pfannkuche (ed.), *Cell Fusion* (Springer New York).
- Kumar, S., J. Aaron, and K. Sokolov. 2008. 'Directional conjugation of antibodies to nanoparticles for synthesis of multiplexed optical contrast agents with both delivery and targeting moieties', *Nat Protoc*, 3: 314-20.
- Landesman-Milo, D., S. Ramishetti, and D. Peer. 2015. 'Nanomedicine as an emerging platform for metastatic lung cancer therapy', *Cancer Metastasis Rev*, 34: 291-301.
- Landskron, G., M. De la Fuente, P. Thuwajit, C. Thuwajit, and M. A. Hermoso. 2014. 'Chronic inflammation and cytokines in the tumor microenvironment', *J Immunol Res*, 2014: 149185.
- Lapidot, T., C. Sirard, J. Vormoor, B. Murdoch, T. Hoang, J. Caceres-Cortes, M. Minden, B. Paterson, M. A. Caligiuri, and J. E. Dick. 1994. 'A cell initiating

- human acute myeloid leukaemia after transplantation into SCID mice', *Nature*, 367: 645-8.
- Larizza, L., and V. Schirmacher. 1984. 'Somatic cell fusion as a source of genetic rearrangement leading to metastatic variants', *Cancer and Metastasis Reviews*, 3: 193-222.
- Lathia, J. D., J. Gallagher, J. T. Myers, M. Li, A. VasANJI, R. E. McLendon, A. B. Hjelmeland, A. Y. Huang, and J. N. Rich. 2011. 'Direct in vivo evidence for tumor propagation by glioblastoma cancer stem cells', *PLoS One*, 6: e24807.
- Lazova, R., A. Chakraborty, and J. M. Pawelek. 2011. 'Leukocyte-cancer cell fusion: initiator of the warburg effect in malignancy?', *Adv Exp Med Biol*, 714: 151-72.
- Leach, J. K., G. Van Tuyle, P. S. Lin, R. Schmidt-Ullrich, and R. B. Mikkelsen. 2001. 'Ionizing radiation-induced, mitochondria-dependent generation of reactive oxygen/nitrogen', *Cancer Res*, 61: 3894-901.
- Lee, S. Y., E. K. Jeong, M. K. Ju, H. M. Jeon, M. Y. Kim, C. H. Kim, H. G. Park, S. I. Han, and H. S. Kang. 2017. 'Induction of metastasis, cancer stem cell phenotype, and oncogenic metabolism in cancer cells by ionizing radiation', *Mol Cancer*, 16: 10.
- Lehnert, B. E., Y. E. Valdez, and C. C. Stewart. 1986. 'Translocation of particles to the tracheobronchial lymph nodes after lung deposition: kinetics and particle-cell relationships', *Exp Lung Res*, 10: 245-66.

- Leroi, N., F. Lallemand, P. Coucke, A. Noel, and P. Martinive. 2016. 'Impacts of Ionizing Radiation on the Different Compartments of the Tumor Microenvironment', *Front Pharmacol*, 7: 78.
- Lewis, M. R., J. Y. Kao, A. L. Anderson, J. E. Shively, and A. Raubitschek. 2001. 'An improved method for conjugating monoclonal antibodies with N-hydroxysulfosuccinimidyl DOTA', *Bioconjug Chem*, 12: 320-4.
- Li, F., L. Gao, Q. Jiang, Z. Wang, B. Dong, T. Yan, and X. Chen. 2013. 'Radiation enhances the invasion abilities of pulmonary adenocarcinoma cells via STAT3', *Mol Med Rep*, 7: 1883-8.
- Li, Ruhong, Arvind Sonik, Reinhard Stindl, David Rasnick, and Peter Duesberg. 2000. 'Aneuploidy vs. gene mutation hypothesis of cancer: Recent study claims mutation but is found to support aneuploidy', *Proceedings of the National Academy of Sciences*, 97: 3236-41.
- Libutti, S. K., G. F. Paciotti, A. A. Byrnes, H. R. Alexander, Jr., W. E. Gannon, M. Walker, G. D. Seidel, N. Yuldasheva, and L. Tamarkin. 2010. 'Phase I and pharmacokinetic studies of CYT-6091, a novel PEGylated colloidal gold-rhTNF nanomedicine', *Clin Cancer Res*, 16: 6139-49.
- Lin, X., A. A. Farooqi, M. Z. Qureshi, M. A. Romero, S. Tabassum, and M. Ismail. 2016. 'Prostate Cancer Stem Cells: Viewing Signaling Cascades at a Finer Resolution', *Arch Immunol Ther Exp (Warsz)*, 64: 217-23.

- Ling, C. C. 1992. 'Permanent Implants Using Au-198, Pd-103 and I-125 - Radiobiological Considerations Based on the Linear Quadratic Model', *International Journal of Radiation Oncology Biology Physics*, 23: 81-87.
- Liu, X., M. Atwater, J. Wang, and Q. Huo. 2007. 'Extinction coefficient of gold nanoparticles with different sizes and different capping ligands', *Colloids Surf B Biointerfaces*, 58: 3-7.
- Liu, X., N. Huang, H. Li, Q. Jin, and J. Ji. 2013. 'Surface and size effects on cell interaction of gold nanoparticles with both phagocytic and nonphagocytic cells', *Langmuir*, 29: 9138-48.
- Lluis, F., and M. P. Cosma. 2010. 'Cell-fusion-mediated somatic-cell reprogramming: a mechanism for tissue regeneration', *J Cell Physiol*, 223: 6-13.
- Loesch, K., S. Galaviz, Z. Hamoui, R. Clanton, G. Akabani, M. Deveau, M. DeJesus, T. Ioerger, J. C. Sacchetti, and D. Wallis. 2015. 'Functional genomics screening utilizing mutant mouse embryonic stem cells identifies novel radiation-response genes', *PLoS One*, 10: e0120534.
- Loira-Pastoriza, C., J. Todoroff, and R. Vanbever. 2014. 'Delivery strategies for sustained drug release in the lungs', *Adv Drug Deliv Rev*, 75: 81-91.
- Lokody, I. 2014. 'Tumour microenvironment: bacterial balance affects cancer treatment', *Nat Rev Cancer*, 14: 10.
- Lou, E., S. Fujisawa, A. Barlas, Y. Romin, K. Manova-Todorova, M. A. Moore, and S. Subramanian. 2012. 'Tunneling Nanotubes: A new paradigm for studying

- intercellular communication and therapeutics in cancer', *Commun Integr Biol*, 5: 399-403.
- Lou, E., S. Fujisawa, A. Morozov, A. Barlas, Y. Romin, Y. Dogan, S. Gholami, A. L. Moreira, K. Manova-Todorova, and M. A. Moore. 2012. 'Tunneling nanotubes provide a unique conduit for intercellular transfer of cellular contents in human malignant pleural mesothelioma', *PLoS One*, 7: e33093.
- Lourenço, Ruy V. 1982. 'Clinical Aerosols', *Archives of Internal Medicine*, 142: 2163-72.
- Lu, X., and Y. Kang. 2009. 'Cell fusion as a hidden force in tumor progression', *Cancer Res*, 69: 8536-9.
- Lu, Xin, and Yibin Kang. 2011. 'Cell Fusion Hypothesis of the Cancer Stem Cell.' in Thomas Dittmar and Kurt S. Zänker (eds.), *Cell Fusion in Health and Disease* (Springer Netherlands).
- Luchetti, F., B. Canonico, M. Arcangeletti, M. Guescini, E. Cesarini, V. Stocchi, M. Degli Esposti, and S. Papa. 2012. 'Fas signalling promotes intercellular communication in T cells', *PLoS One*, 7: e35766.
- Lundborg, M., B. Lind, and P. Camner. 1984. 'Ability of rabbit alveolar macrophages to dissolve metals', *Exp Lung Res*, 7: 11-22.
- Lundh, C., U. Lindencrona, A. Schmitt, M. Nilsson, and E. Forssell-Aronsson. 2006. 'Biodistribution of free ²¹¹At and ¹²⁵I- in nude mice bearing tumors derived from anaplastic thyroid carcinoma cell lines', *Cancer Biother Radiopharm*, 21: 591-600.

- Luo, J., S. Ok Lee, L. Liang, C. K. Huang, L. Li, S. Wen, and C. Chang. 2014. 'Infiltrating bone marrow mesenchymal stem cells increase prostate cancer stem cell population and metastatic ability via secreting cytokines to suppress androgen receptor signaling', *Oncogene*, 33: 2768-78.
- MacLauchlan, S., E. A. Skokos, N. Meznarich, D. H. Zhu, S. Raof, J. M. Shipley, R. M. Senior, P. Bornstein, and T. R. Kyriakides. 2009. 'Macrophage fusion, giant cell formation, and the foreign body response require matrix metalloproteinase 9', *J Leukoc Biol*, 85: 617-26.
- Madani, I., W. De Neve, and M. Mareel. 2008. 'Does ionizing radiation stimulate cancer invasion and metastasis?', *Bull Cancer*, 95: 292-300.
- Majeti, Ravindra, Mark P Chao, Ash A Alizadeh, Wendy W Pang, Siddhartha Jaiswal, Kenneth D Gibbs, Nico van Rooijen, and Irving L Weissman. 2009. 'CD47 is an adverse prognostic factor and therapeutic antibody target on human acute myeloid leukemia stem cells', *Cell*, 138: 286-99.
- Marcato, Paola, Cheryl A Dean, Da Pan, Rakhna Araslanova, Megan Gillis, Madalsa Joshi, Lucy Helyer, Luzhe Pan, Andrew Leidal, and Shashi Gujar. 2011. 'Aldehyde dehydrogenase activity of breast cancer stem cells is primarily due to isoform ALDH1A3 and its expression is predictive of metastasis', *Stem Cells*, 29: 32-45.
- Marcato, Paola, Cheryl A. Dean, Carman A. Giacomantonio, and Patrick W. K. Lee. 2011. 'Aldehyde dehydrogenase: Its role as a cancer stem cell marker comes down to the specific isoform', *Cell Cycle*, 10: 1378-84.

- Martin, R. F., and W. A. Haseltine. 1981. 'Range of radiochemical damage to DNA with decay of iodine-125', *Science*, 213: 896-8.
- Martinez-Rodriguez, I., and I. Banzo. 2017. 'Advances in PET: The success of multimodal molecular imaging', *Med Clin (Barc)*, 148: 354-56.
- Martinez, A., M. Martinez-Ramirez, D. Martinez-Caballero, P. Beneit, J. Clavel, G. Figueroa, and J. Verdu. 2017. 'Radioimmunotherapy for non-Hodgkin's lymphoma; positioning, safety, and efficacy of 90Y-Ibritumomab. 10 years of experience and follow-up', *Rev Esp Med Nucl Imagen Mol*, 36: 13-19.
- McBurney, M. W. 1977. 'Chimeric mice derived from normal embryos injected with teratocarcinoma cells', *Am J Pathol*, 89: 685-6.
- McLaughlin, R. W., H. Vali, P. C. K. Lau, R. G. E. Palfree, A. De Ciccio, M. Sirois, D. Ahmad, R. Villemur, M. Desrosiers, and E. C. S. Chan. 2002. 'Are There Naturally Occurring Pleomorphic Bacteria in the Blood of Healthy Humans?', *Journal of Clinical Microbiology*, 40: 4771-75.
- Medine, E Ilker, Perihan Ünak, Serhan Sakarya, and Feriha Özkaya. 2011. 'Investigation of in vitro efficiency of magnetic nanoparticle-conjugated 125I-uracil glucuronides in adenocarcinoma cells', *Journal of Nanoparticle Research*, 13: 4703-15.
- Mehlen, P., and A. Puisieux. 2006. 'Metastasis: a question of life or death', *Nat Rev Cancer*, 6: 449-58.
- Mendez, L. B., G. Gookin, and R. F. Phalen. 2010. 'Inhaled aerosol particle dosimetry in mice: a review', *Inhal Toxicol*, 22 Suppl 2: 15-20.

- Merryman, Don J., John D. Corbett, and Paul A. Edwards. 1975. 'Polyiodine cations as chlorometalate salts. Synthesis and nuclear quadrupole resonance characterization of triiodinium, pentaiodinium, and chlorodiiodinium tetrachloroaluminates', *Inorganic Chemistry*, 14: 428-34.
- Meuwissen, R., and A. Berns. 2005. 'Mouse models for human lung cancer', *Genes Dev*, 19: 643-64.
- Milenic, D. E., E. D. Brady, and M. W. Brechbiel. 2004. 'Antibody-targeted radiation cancer therapy', *Nat Rev Drug Discov*, 3: 488-99.
- Mitchell, J. P., J. Suggett, and M. Nagel. 2016. 'Clinically Relevant In Vitro Testing of Orally Inhaled Products-Bridging the Gap Between the Lab and the Patient', *AAPS PharmSciTech*, 17: 787-804.
- Miyamoto, S., H. Baba, S. Kuroda, K. Kaibuchi, T. Fukuda, Y. Maehara, and T. Saito. 2000. 'Changes in E-cadherin associated with cytoplasmic molecules in well and poorly differentiated endometrial cancer', *Br J Cancer*, 83: 1168-75.
- Mkandawire, M. M., M. Lakatos, A. Springer, A. Clemens, D. Appelhans, U. Krause-Buchholz, W. Pompe, G. Rodel, and M. Mkandawire. 2015. 'Induction of apoptosis in human cancer cells by targeting mitochondria with gold nanoparticles', *Nanoscale*, 7: 10634-40.
- Morrissey, D., G. C. O'Sullivan, and M. Tangney. 2010. 'Tumour targeting with systemically administered bacteria', *Curr Gene Ther*, 10: 3-14.
- Mortensen, N. P., and A. J. Hickey. 2014. 'Targeting inhaled therapy beyond the lungs', *Respiration*, 88: 353-4.

- Morton, C. L., and P. J. Houghton. 2007. 'Establishment of human tumor xenografts in immunodeficient mice', *Nat Protoc*, 2: 247-50.
- Mountain, C. F. 1997. 'Revisions in the International System for Staging Lung Cancer', *Chest*, 111: 1710-7.
- Muller, H. J. 1927. 'Artificial Transmutation of the Gene', *Science*, 66: 84-87.
- Muralidharan, P., M. Malapit, E. Mallory, D. Hayes, Jr., and H. M. Mansour. 2015. 'Inhalable nanoparticulate powders for respiratory delivery', *Nanomedicine*, 11: 1189-99.
- Murch, A. R., M. D. Grounds, C. A. Marshall, and J. M. Papadimitriou. 1982. 'Direct evidence that inflammatory multinucleate giant cells form by fusion', *J Pathol*, 137: 177-80.
- Nabeshima, Kazuki, Yoshiya Shima, Teruhiko Inoue, and Masashi Koono. 2002. 'Immunohistochemical analysis of IQGAP1 expression in human colorectal carcinomas: its overexpression in carcinomas and association with invasion fronts', *Cancer letters*, 176: 101-09.
- Nakayama, M., K. Itoh, and E. Takahashi. 1997. 'Cyclophosphamide-induced bacterial translocation in Escherichia coli C25-monoassociated specific pathogen-free mice', *Microbiol Immunol*, 41: 587-93.
- Narra, V. R., R. W. Howell, R. S. Harapanhalli, K. S. Sastry, and D. V. Rao. 1992. 'Radiotoxicity of some iodine-123, iodine-125 and iodine-131-labeled compounds in mouse testes: implications for radiopharmaceutical design', *J Nucl Med*, 33: 2196-201.

- National Institute for Public Health and the Environment (RIVM). 2002. "Multiple Path Particle Dosimetry Model (MPPD v 1.0): A Model for Human and Rat Airway Particle Dosimetry. Report 650010030." In. Bilthoven, The Netherlands: RIVA.
- Nicolson, Garth L. 2014. 'Mitochondrial Dysfunction and Chronic Disease: Treatment With Natural Supplements', *Integrative Medicine: A Clinician's Journal*, 13: 35-43.
- Nilsson, S. 2016. 'Radionuclide Therapies in Prostate Cancer: Integrating Radium-223 in the Treatment of Patients With Metastatic Castration-Resistant Prostate Cancer', *Curr Oncol Rep*, 18: 14.
- Nishida, H., H. Yamazaki, T. Yamada, S. Iwata, N. H. Dang, T. Inukai, K. Sugita, Y. Ikeda, and C. Morimoto. 2009. 'CD9 correlates with cancer stem cell potentials in human B-acute lymphoblastic leukemia cells', *Biochem Biophys Res Commun*, 382: 57-62.
- Noubissi, F. K., T. Harkness, C. M. Alexander, and B. M. Ogle. 2015. 'Apoptosis-induced cancer cell fusion: a mechanism of breast cancer metastasis', *FASEB J*, 29: 4036-45.
- Nowak-Imialek, M., W. A. Kues, C. Rudolph, B. Schlegelberger, U. Taylor, J. W. Carnwath, and H. Niemann. 2010. 'Preferential loss of porcine chromosomes in reprogrammed interspecies cell hybrids', *Cell Reprogram*, 12: 55-65.
- Nussbaum, J., E. Minami, M. A. Laflamme, J. A. Virag, C. B. Ware, A. Masino, V. Muskheli, L. Pabon, H. Reinecke, and C. E. Murry. 2007. 'Transplantation of

- undifferentiated murine embryonic stem cells in the heart: teratoma formation and immune response', *FASEB J*, 21: 1345-57.
- O'Brien, C. A., A. Pollett, S. Gallinger, and J. E. Dick. 2007. 'A human colon cancer cell capable of initiating tumour growth in immunodeficient mice', *Nature*, 445: 106-10.
- Oberdörster, G. 1988. 'Lung clearance of inhaled insoluble and soluble particles', *Journal of Aerosol Medicine*, 1: 289-330.
- Okamoto, R., T. Yajima, M. Yamazaki, T. Kanai, M. Mukai, S. Okamoto, Y. Ikeda, T. Hibi, J. Inazawa, and M. Watanabe. 2002. 'Damaged epithelia regenerated by bone marrow-derived cells in the human gastrointestinal tract', *Nat Med*, 8: 1011-7.
- Olempska, M., P. A. Eisenach, O. Ammerpohl, H. Ungefroren, F. Fandrich, and H. Kalthoff. 2007. 'Detection of tumor stem cell markers in pancreatic carcinoma cell lines', *Hepatobiliary Pancreat Dis Int*, 6: 92-7.
- Olney, H. J., M. A. Freeman, D. A. Stewart, J. E. Mangel, D. J. White, and J. O. Elia-Pacitti. 2014. 'Prolonged progression-free survival and preserved quality of life in the Canadian prospective study of tositumomab and iodine(131)-tositumomab for previously treated, rituximab-exposed, indolent non-Hodgkin lymphoma', *Leuk Lymphoma*, 55: 2754-60.
- Orian-Rousseau, V. 2010. 'CD44, a therapeutic target for metastasising tumours', *Eur J Cancer*, 46: 1271-7.

- Paciotti, G. F., L. Myer, D. Weinreich, D. Goia, N. Pavel, R. E. McLaughlin, and L. Tamarkin. 2004. 'Colloidal gold: a novel nanoparticle vector for tumor directed drug delivery', *Drug Deliv*, 11: 169-83.
- Paciotti, Giulio F., David G. I. Kingston, and Lawrence Tamarkin. 2006. 'Colloidal gold nanoparticles: a novel nanoparticle platform for developing multifunctional tumor-targeted drug delivery vectors', *Drug Development Research*, 67: 47-54.
- Paillas, S., R. Ladjohounlou, C. Lozza, A. Pichard, V. Boudousq, M. Jarlier, S. Sevestre, M. Le Blay, E. Deshayes, J. Sosabowski, T. Chardes, I. Navarro-Teulon, R. J. Mairs, and J. P. Pouget. 2016. 'Localized Irradiation of Cell Membrane by Auger Electrons Is Cytotoxic Through Oxidative Stress-Mediated Nontargeted Effects', *Antioxid Redox Signal*, 25: 467-84.
- Palm, S., J. L. Humm, R. Rundqvist, and L. Jacobsson. 2004. 'Microdosimetry of astatine-211 single-cell irradiation: role of daughter polonium-211 diffusion', *Medical Physics*, 31: 218-25.
- Pandit-Taskar, N., S. M. Larson, and J. A. Carrasquillo. 2014. 'Bone-seeking radiopharmaceuticals for treatment of osseous metastases, Part 1: alpha therapy with ²²³Ra-dichloride', *J Nucl Med*, 55: 268-74.
- Papaioannou, V. E., R. L. Gardner, M. W. McBurney, C. Babinet, and M. J. Evans. 1978. 'Participation of cultured teratocarcinoma cells in mouse embryogenesis', *J Embryol Exp Morphol*, 44: 93-104.
- Papaioannou, V. E., M. W. McBurney, R. L. Gardner, and M. J. Evans. 1975. 'Fate of teratocarcinoma cells injected into early mouse embryos', *Nature*, 258: 70-73.

- Patra, H. K., S. Banerjee, U. Chaudhuri, P. Lahiri, and A. K. Dasgupta. 2007. 'Cell selective response to gold nanoparticles', *Nanomedicine*, 3: 111-9.
- Pawelek, John M. 2007. 'Viewing Malignant Melanoma Cells as Macrophage-Tumor Hybrids', *Cell Adhesion & Migration*, 1: 2-6.
- Pawelek, John M., K. Brooks Low, and David Bermudes. 2003. 'Bacteria as tumour-targeting vectors', *The Lancet Oncology*, 4: 548-56.
- Peer, D., J. M. Karp, S. Hong, O. C. Farokhzad, R. Margalit, and R. Langer. 2007. 'Nanocarriers as an emerging platform for cancer therapy', *Nat Nanotechnol*, 2: 751-60.
- Pialoux, V., R. Mounier, A. D. Brown, C. D. Steinback, J. M. Rawling, and M. J. Poulin. 2009. 'Relationship between oxidative stress and HIF-1 alpha mRNA during sustained hypoxia in humans', *Free Radic Biol Med*, 46: 321-6.
- Piotr, Zygmanski, Liu Bo, Tsiamas Panagiotis, Cifter Fulya, Petersheim Markus, Hesser Jürgen, and Sajo Erno. 2013. 'Dependence of Monte Carlo microdosimetric computations on the simulation geometry of gold nanoparticles', *Physics in Medicine and Biology*, 58: 7961.
- Polte, J., T. T. Ahner, F. Delissen, S. Sokolov, F. Emmerling, A. F. Thunemann, and R. Kraehnert. 2010. 'Mechanism of gold nanoparticle formation in the classical citrate synthesis method derived from coupled in situ XANES and SAXS evaluation', *J Am Chem Soc*, 132: 1296-301.

- Pontow, S. E., N. V. Heyden, S. Wei, and L. Ratner. 2004. 'Actin cytoskeletal reorganizations and coreceptor-mediated activation of rac during human immunodeficiency virus-induced cell fusion', *J Virol*, 78: 7138-47.
- Powell, A. E., E. C. Anderson, P. S. Davies, A. D. Silk, C. Pelz, S. Impey, and M. H. Wong. 2011. 'Fusion between Intestinal epithelial cells and macrophages in a cancer context results in nuclear reprogramming', *Cancer Res*, 71: 1497-505.
- Prince, J. R., S. M. Zu'bi, and B. L. Haag. 1979. 'Thyroid imaging with iodine-125 and technetium-99m', *Eur J Nucl Med*, 4: 37-41.
- Prince, M. E., R. Sivanandan, A. Kaczorowski, G. T. Wolf, M. J. Kaplan, P. Dalerba, I. L. Weissman, M. F. Clarke, and L. E. Ailles. 2007. 'Identification of a subpopulation of cells with cancer stem cell properties in head and neck squamous cell carcinoma', *Proc Natl Acad Sci U S A*, 104: 973-8.
- Pulley, Marina Lee 2015. 'Energy Deposition and Nanodosimetry of Iodine-125 and Tin-117m Labeled Gold Nanoparticles: A Computational Model Using Geant4-DNA', Master's Thesis, Texas A&M University.
- Purandare, N. C., and V. Rangarajan. 2015. 'Imaging of lung cancer: Implications on staging and management', *Indian J Radiol Imaging*, 25: 109-20.
- Pyykkö, Pekka. 2005. 'Theoretical chemistry of gold. II', *Inorganica Chimica Acta*, 358: 4113-30.
- Quere, R., S. Andradottir, A. C. Brun, R. A. Zubarev, G. Karlsson, K. Olsson, M. Magnusson, J. Cammenga, and S. Karlsson. 2011. 'High levels of the adhesion

- molecule CD44 on leukemic cells generate acute myeloid leukemia relapse after withdrawal of the initial transforming event', *Leukemia*, 25: 515-26.
- Rahman, W. N., N. Bishara, T. Ackerly, C. F. He, P. Jackson, C. Wong, R. Davidson, and M. Geso. 2009. 'Enhancement of radiation effects by gold nanoparticles for superficial radiation therapy', *Nanomedicine*, 5: 136-42.
- Rahmani, M., B. W. Wong, L. Ang, C. C. Cheung, J. M. Carthy, H. Walinski, and B. M. McManus. 2006. 'Versican: signaling to transcriptional control pathways', *Can J Physiol Pharmacol*, 84: 77-92.
- Rappa, G., T. M. Green, J. Karbanova, D. Corbeil, and A. Loricco. 2015. 'Tetraspanin CD9 determines invasiveness and tumorigenicity of human breast cancer cells', *Oncotarget*, 6: 7970-91.
- Rau, J. L., A. Ari, and R. D. Restrepo. 2004. 'Performance comparison of nebulizer designs: constant-output, breath-enhanced, and dosimetric', *Respir Care*, 49: 174-9.
- Rehman, J., H. J. Zhang, P. T. Toth, Y. Zhang, G. Marsboom, Z. Hong, R. Salgia, A. N. Husain, C. Wietholt, and S. L. Archer. 2012. 'Inhibition of mitochondrial fission prevents cell cycle progression in lung cancer', *FASEB J*, 26: 2175-86.
- Reist, Craig J., Catherine F. Foulon, Kevin Alston, Darell D. Bigner, and Michael R. Zalutsky. 1999. 'Astatine-211 labeling of internalizing anti-EGFRvIII monoclonal antibody using N-succinimidyl 5-[211At]astato-3-pyridinecarboxylate', *Nuclear Medicine and Biology*, 26: 405-11.

- Rempel, S. A., S. Dudas, S. Ge, and J. A. Gutierrez. 2000. 'Identification and localization of the cytokine SDF1 and its receptor, CXC chemokine receptor 4, to regions of necrosis and angiogenesis in human glioblastoma', *Clin Cancer Res*, 6: 102-11.
- Reynolds, S. D., and A. M. Malkinson. 2010. 'Clara cell: progenitor for the bronchiolar epithelium', *Int J Biochem Cell Biol*, 42: 1-4.
- Ricci-Vitiani, L., D. G. Lombardi, E. Pilozzi, M. Biffoni, M. Todaro, C. Peschle, and R. De Maria. 2007. 'Identification and expansion of human colon-cancer-initiating cells', *Nature*, 445: 111-5.
- Riley, P. A. 1994. 'Free radicals in biology: oxidative stress and the effects of ionizing radiation', *Int J Radiat Biol*, 65: 27-33.
- Robinson, J. M., D. S. Roos, R. L. Davidson, and M. J. Karnovsky. 1979. 'Membrane alterations and other morphological features associated with polyethylene glycol-induced cell fusion', *J Cell Sci*, 40: 63-75.
- Roy, H. K., J. K. DiBaise, J. Black, W. J. Karolski, A. Ratashak, and S. Ansari. 2001. 'Polyethylene glycol induces apoptosis in HT-29 cells: potential mechanism for chemoprevention of colon cancer', *FEBS Lett*, 496: 143-6.
- Ruff, M. R., and C. B. Pert. 1984. 'Small cell carcinoma of the lung: macrophage-specific antigens suggest hemopoietic stem cell origin', *Science*, 225: 1034-6.
- Sakko, A. J., C. Ricciardelli, K. Mayne, S. Suwivat, R. G. LeBaron, V. R. Marshall, W. D. Tilley, and D. J. Horsfall. 2003. 'Modulation of prostate cancer cell attachment to matrix by versican', *Cancer Res*, 63: 4786-91.

- Salaun, P. Y., L. Campion, C. Bournaud, A. Faivre-Chauvet, J. P. Vuillez, D. Taieb, C. Ansquer, C. Rousseau, F. Borson-Chazot, S. Bardet, A. Oudoux, B. Cariou, E. Mirallie, C. H. Chang, R. M. Sharkey, D. M. Goldenberg, J. F. Chatal, J. Barbet, and F. Kraeber-Bodere. 2012. 'Phase II trial of anticarcinoembryonic antigen pretargeted radioimmunotherapy in progressive metastatic medullary thyroid carcinoma: biomarker response and survival improvement', *J Nucl Med*, 53: 1185-92.
- Samudio, I., M. Fiegl, and M. Andreeff. 2009. 'Mitochondrial uncoupling and the Warburg effect: molecular basis for the reprogramming of cancer cell metabolism', *Cancer Res*, 69: 2163-6.
- Sanford, K. 2005. 'Reintroduction to nutrition and cancer treatment', *Semin Oncol Nurs*, 21: 164-72.
- Sansare, K., V. Khanna, and F. Karjodkar. 2011. 'Early victims of X-rays: a tribute and current perception', *Dentomaxillofacial Radiology*, 40: 123-25.
- Sąsiadek, Maria, and Paweł Karpiński. 2009. "Genetic Theory of Cancer. Short Review." In *Polish Journal of Surgery*, 478.
- Schatton, T., G. F. Murphy, N. Y. Frank, K. Yamaura, A. M. Waaga-Gasser, M. Gasser, Q. Zhan, S. Jordan, L. M. Duncan, C. Weishaupt, R. C. Fuhlbrigge, T. S. Kupper, M. H. Sayegh, and M. H. Frank. 2008. 'Identification of cells initiating human melanomas', *Nature*, 451: 345-9.
- Schneider, C. A., W. S. Rasband, and K. W. Eliceiri. 2012. 'NIH Image to ImageJ: 25 years of image analysis', *Nat Methods*, 9: 671-5.

- Seigel, G. M., A. S. Hackam, A. Ganguly, L. M. Mandell, and F. Gonzalez-Fernandez. 2007. 'Human embryonic and neuronal stem cell markers in retinoblastoma', *Mol Vis*, 13: 823-32.
- Seiter, S., R. Arch, S. Reber, D. Komitowski, M. Hofmann, H. Ponta, P. Herrlich, S. Matzku, and M. Zoller. 1993. 'Prevention of tumor metastasis formation by anti-variant CD44', *J Exp Med*, 177: 443-55.
- Semenza, G. L. 2002. 'HIF-1 and tumor progression: pathophysiology and therapeutics', *Trends Mol Med*, 8: S62-7.
- Semmler-Behnke, M., S. Takenaka, S. Fertsch, A. Wenk, J. Seitz, P. Mayer, G. Oberdorster, and W. G. Kreyling. 2007. 'Efficient elimination of inhaled nanoparticles from the alveolar region: evidence for interstitial uptake and subsequent reentrainment onto airways epithelium', *Environ Health Perspect*, 115: 728-33.
- Semmler, M., J. Seitz, F. Erbe, P. Mayer, J. Heyder, G. Oberdorster, and W. G. Kreyling. 2004. 'Long-term clearance kinetics of inhaled ultrafine insoluble iridium particles from the rat lung, including transient translocation into secondary organs', *Inhal Toxicol*, 16: 453-9.
- Sgouros, G. 2008. 'Alpha-particles for targeted therapy', *Adv Drug Deliv Rev*, 60: 1402-6.
- Shabo, I., and J. Svanvik. 2011. 'Expression of macrophage antigens by tumor cells', *Adv Exp Med Biol*, 714: 141-50.

- Shao, C., Y. Furusawa, M. Aoki, and K. Ando. 2003. 'Role of gap junctional intercellular communication in radiation-induced bystander effects in human fibroblasts', *Radiat Res*, 160: 318-23.
- Shaw, A. T., D. G. Kirsch, and T. Jacks. 2005. 'Future of early detection of lung cancer: the role of mouse models', *Clin Cancer Res*, 11: 4999s-5003s.
- Shekhani, M. T., A. S. Jayanthi, N. Maddodi, and V. Setaluri. 2013. 'Cancer stem cells and tumor transdifferentiation: implications for novel therapeutic strategies', *Am J Stem Cells*, 2: 52-61.
- Shete, H. K., S. S. Vyas, V. B. Patravale, and J. I. Disouza. 2014. 'Pulmonary multifunctional nano-oncological modules for lung cancer treatment and prevention', *J Biomed Nanotechnol*, 10: 1863-93.
- Shukla, R., V. Bansal, M. Chaudhary, A. Basu, R. R. Bhonde, and M. Sastry. 2005. 'Biocompatibility of gold nanoparticles and their endocytotic fate inside the cellular compartment: a microscopic overview', *Langmuir*, 21: 10644-54.
- Silberstein, E. B. 2012. 'Radioiodine: the classic theranostic agent', *Semin Nucl Med*, 42: 164-70.
- Silk, A. D., C. E. Gast, P. S. Davies, F. D. Fakhari, G. E. Vanderbeek, M. Mori, and M. H. Wong. 2013. 'Fusion between hematopoietic and epithelial cells in adult human intestine', *PLoS One*, 8: e55572.
- Singh, S. K., I. D. Clarke, M. Terasaki, V. E. Bonn, C. Hawkins, J. Squire, and P. B. Dirks. 2003. 'Identification of a cancer stem cell in human brain tumors', *Cancer Res*, 63: 5821-8.

- Singh, S. K., C. Hawkins, I. D. Clarke, J. A. Squire, J. Bayani, T. Hide, R. M. Henkelman, M. D. Cusimano, and P. B. Dirks. 2004. 'Identification of human brain tumour initiating cells', *Nature*, 432: 396-401.
- Smith, J. R., and E. Oates. 2004. 'Radionuclide imaging of the thyroid gland: patterns, pearls, and pitfalls', *Clin Nucl Med*, 29: 181-93.
- Smith, K. A. 2012. 'Louis pasteur, the father of immunology?', *Front Immunol*, 3: 68.
- Sofia Vala, I., L. R. Martins, N. Imaizumi, R. J. Nunes, J. Rino, F. Kuonen, L. M. Carvalho, C. Ruegg, I. M. Grillo, J. T. Barata, M. Mareel, and S. C. Santos. 2010. 'Low doses of ionizing radiation promote tumor growth and metastasis by enhancing angiogenesis', *PLoS One*, 5: e11222.
- Stepanek, J., B. Larsson, and R. Weinreich. 1996. 'Auger-electron spectra of radionuclides for therapy and diagnostics', *Acta Oncol*, 35: 863-8.
- Sterling, H., C. Saginario, and A. Vignery. 1998. 'CD44 occupancy prevents macrophage multinucleation', *Journal of Cell Biology*, 143: 837-47.
- Stone, H. B., C. N. Coleman, M. S. Anscher, and W. H. McBride. 2003. 'Effects of radiation on normal tissue: consequences and mechanisms', *Lancet Oncol*, 4: 529-36.
- Svensson, P. H., and L. Kloo. 2003. 'Synthesis, structure, and bonding in polyiodide and metal iodide-iodine systems', *Chem Rev*, 103: 1649-84.
- Swank, G. M., and E. A. Deitch. 1996. 'Role of the gut in multiple organ failure: bacterial translocation and permeability changes', *World J Surg*, 20: 411-7.

- Swierczewska, M., S. Lee, and X. Chen. 2011. 'The design and application of fluorophore-gold nanoparticle activatable probes', *Phys Chem Chem Phys*, 13: 9929-41.
- Taggart, L. E., S. J. McMahon, F. J. Currell, K. M. Prise, and K. T. Butterworth. 2014. 'The role of mitochondrial function in gold nanoparticle mediated radiosensitisation', *Cancer Nanotechnol*, 5: 5.
- Tang, S., Y. Wu, W. Liao, R. Bai, C. Liu, and A. Lei. 2014. 'Revealing the metal-like behavior of iodine: an iodide-catalysed radical oxidative alkenylation', *Chem Commun (Camb)*, 50: 4496-9.
- Teicher, B. A., and S. P. Fricker. 2010. 'CXCL12 (SDF-1)/CXCR4 pathway in cancer', *Clin Cancer Res*, 16: 2927-31.
- Terada, N., T. Hamazaki, M. Oka, M. Hoki, D. M. Mastalerz, Y. Nakano, E. M. Meyer, L. Morel, B. E. Petersen, and E. W. Scott. 2002. 'Bone marrow cells adopt the phenotype of other cells by spontaneous cell fusion', *Nature*, 416: 542-5.
- Thannickal, V. J., and B. L. Fanburg. 2000. 'Reactive oxygen species in cell signaling', *Am J Physiol Lung Cell Mol Physiol*, 279: L1005-28.
- Theise, N. D., M. Nimmakayalu, R. Gardner, P. B. Illei, G. Morgan, L. Teperman, O. Henegariu, and D. S. Krause. 2000. 'Liver from bone marrow in humans', *Hepatology*, 32: 11-6.
- Ting, G., C. H. Chang, H. E. Wang, and T. W. Lee. 2010. 'Nanotargeted radionuclides for cancer nuclear imaging and internal radiotherapy', *J Biomed Biotechnol*, 2010.

- Trinchieri, G. 2013. 'L06.03 * Gut Commensal Bacteria Determine Cancer Response to Treatment by Modulating Systemic Inflammation', *Annals of Oncology*, 24: i12-i12.
- Turkington, T. G., M. R. Zalutsky, R. J. Jaszczak, P. K. Garg, G. Vaidyanathan, and R. E. Coleman. 1993. 'Measuring astatine-211 distributions with SPECT', *Phys Med Biol*, 38: 1121-30.
- Ucar, Deniz, Christopher R Cogle, James R Zucali, Blanca Ostmark, Edward W Scott, Robert Zori, Brian A Gray, and Jan S Moreb. 2009. 'Aldehyde dehydrogenase activity as a functional marker for lung cancer', *Chemico-biological interactions*, 178: 48-55.
- Vaca, C. E., J. Wilhelm, and M. Harms-Ringdahl. 1988. 'Interaction of lipid peroxidation products with DNA. A review', *Mutat Res*, 195: 137-49.
- van der Schee, M. P., T. Paff, P. Brinkman, W. M. C. van Aalderen, E. G. Haarman, and P. J. Sterk. 2015. 'Breathomics in lung disease', *Chest*, 147: 224-31.
- Vandamme, T. F. 2014. 'Use of rodents as models of human diseases', *J Pharm Bioallied Sci*, 6: 2-9.
- Vaughan, Douglas. 1986. "X-ray data booklet. Revision." In.: Lawrence Berkeley Lab., CA (USA).
- Verschoor, J. A., C. H. Boshoff, L. Coetzee, S. Van Wyngaardt, and L. Visser. 1990. 'Spontaneous fusion between splenocytes and myeloma cells induced by bacterial immunization', *Hybridoma*, 9: 511-8.

- Viaud, S., F. Saccheri, G. Mignot, T. Yamazaki, R. Daillere, D. Hannani, D. P. Enot, C. Pfirschke, C. Engblom, M. J. Pittet, A. Schlitzer, F. Ginhoux, L. Apetoh, E. Chachaty, P. L. Woerther, G. Eberl, M. Berard, C. Ecobichon, D. Clermont, C. Bizet, V. Gaboriau-Routhiau, N. Cerf-Bensussan, P. Opolon, N. Yessaad, E. Vivier, B. Ryffel, C. O. Elson, J. Dore, G. Kroemer, P. Lepage, I. G. Boneca, F. Ghiringhelli, and L. Zitvogel. 2013. 'The intestinal microbiota modulates the anticancer immune effects of cyclophosphamide', *Science*, 342: 971-6.
- Villiers, C., H. Freitas, R. Couderc, M. B. Villiers, and P. Marche. 2010. 'Analysis of the toxicity of gold nano particles on the immune system: effect on dendritic cell functions', *J Nanopart Res*, 12: 55-60.
- Virchow, Rudolf Ludwig Karl. 1865. *Die krankhaften Geschwülste* (A. Hirschwald).
- Wallace, D. C. 2005a. 'A mitochondrial paradigm of metabolic and degenerative diseases, aging, and cancer: a dawn for evolutionary medicine', *Annu Rev Genet*, 39: 359-407.
- Wallace, DC. 2005b. "Mitochondria and cancer: Warburg addressed." In *Cold Spring Harbor symposia on quantitative biology*, 363-74. Cold Spring Harbor Laboratory Press.
- Wang, G. P., and X. F. Han. 2015. 'CD9 modulates proliferation of human glioblastoma cells via epidermal growth factor receptor signaling', *Mol Med Rep*, 12: 1381-6.
- Wang, J., L. P. Guo, L. Z. Chen, Y. X. Zeng, and S. H. Lu. 2007. 'Identification of cancer stem cell-like side population cells in human nasopharyngeal carcinoma cell line', *Cancer Res*, 67: 3716-24.

- Wang, L., Y. Liu, W. Li, X. Jiang, Y. Ji, X. Wu, L. Xu, Y. Qiu, K. Zhao, T. Wei, Y. Li, Y. Zhao, and C. Chen. 2011. 'Selective targeting of gold nanorods at the mitochondria of cancer cells: implications for cancer therapy', *Nano Lett*, 11: 772-80.
- Wang, W., R. Eddy, and J. Condeelis. 2007. 'The cofilin pathway in breast cancer invasion and metastasis', *Nat Rev Cancer*, 7: 429-40.
- Wang, W., S. Goswami, K. Lapidus, A. L. Wells, J. B. Wyckoff, E. Sahai, R. H. Singer, J. E. Segall, and J. S. Condeelis. 2004. 'Identification and testing of a gene expression signature of invasive carcinoma cells within primary mammary tumors', *Cancer Res*, 64: 8585-94.
- Wang, X., M. Fox, S. Povey, and J. R. Masters. 1998. 'Mouse-human somatic cell hybrids: loss of mouse and human chromosomes', *Somat Cell Mol Genet*, 24: 165-71.
- Wang, X., and H. H. Gerdes. 2015. 'Transfer of mitochondria via tunneling nanotubes rescues apoptotic PC12 cells', *Cell Death Differ*, 22: 1181-91.
- Wang, Y., J. Cui, X. Sun, and Y. Zhang. 2011. 'Tunneling-nanotube development in astrocytes depends on p53 activation', *Cell Death Differ*, 18: 732-42.
- Warburg, O. 1956. 'On the origin of cancer cells', *Science*, 123: 309-14.
- Warburg, Otto. 1924. 'Über den Stoffwechsel der Carcinomzelle', *Naturwissenschaften*, 12: 1131-37.

- Watts, A. B., J. T. McConville, and R. O. Williams, 3rd. 2008. 'Current therapies and technological advances in aqueous aerosol drug delivery', *Drug Dev Ind Pharm*, 34: 913-22.
- Weimann, J. M., C. A. Charlton, T. R. Brazelton, R. C. Hackman, and H. M. Blau. 2003. 'Contribution of transplanted bone marrow cells to Purkinje neurons in human adult brains', *Proc Natl Acad Sci U S A*, 100: 2088-93.
- Weimann, J. M., C. B. Johansson, A. Trejo, and H. M. Blau. 2003. 'Stable reprogrammed heterokaryons form spontaneously in Purkinje neurons after bone marrow transplant', *Nat Cell Biol*, 5: 959-66.
- Weinberg, Joel M., Manjeri A. Venkatachalam, Nancy F. Roeser, and Itzhak Nissim. 2000. 'Mitochondrial dysfunction during hypoxia/reoxygenation and its correction by anaerobic metabolism of citric acid cycle intermediates', *Proceedings of the National Academy of Sciences*, 97: 2826-31.
- Werth, N., C. Beerlage, C. Rosenberger, A. S. Yazdi, M. Edelmann, A. Amr, W. Bernhardt, C. von Eiff, K. Becker, A. Schafer, A. Peschel, and V. A. Kempf. 2010. 'Activation of hypoxia inducible factor 1 is a general phenomenon in infections with human pathogens', *PLoS One*, 5: e11576.
- Wieland, D. M., L. E. Brown, W. L. Rogers, K. C. Worthington, J. L. Wu, N. H. Clinthorne, C. A. Otto, D. P. Swanson, and W. H. Beierwaltes. 1981. 'Myocardial imaging with a radioiodinated norepinephrine storage analog', *J Nucl Med*, 22: 22-31.

- Wiersema, Anita, Freak Dijk, Bert Dontje, Johannes J. van der Want, and Gerald de Haan. 2008. 'Cerebellar heterokaryon formation increases with age and after irradiation', *Stem Cell Research*, 1: 150-54.
- Wojcieszyn, J. W. 1983. 'Studies on the mechanism of polyethylene glycol-mediated cell fusion using fluorescent membrane and cytoplasmic probes', *The Journal of Cell Biology*, 96: 151-59.
- Wolfsberg, Max. 2002. 'Theoretical evaluation of experimentally observed isotope effects', *Accounts of Chemical Research*, 5: 225-33.
- Wong, J. Y. C., D. Z. Chu, D. M. Yamauchi, L. E. Williams, A. Liu, S. Wilczynski, A. M. Wu, J. E. Shively, J. H. Doroshov, and A. A. Raubitschek. 2000. 'A phase I radioimmunotherapy trial evaluating 90yttrium-labeled anti-carcinoembryonic antigen (CEA) chimeric T84.66 in patients with metastatic CEA-producing malignancies', *Clin Cancer Res*, 6: 3855-63.
- Wurmser, A. E., and F. H. Gage. 2002. 'Stem cells: cell fusion causes confusion', *Nature*, 416: 485-7.
- Yamada, M., H. Kubo, S. Kobayashi, K. Ishizawa, M. Numasaki, S. Ueda, T. Suzuki, and H. Sasaki. 2004. 'Bone marrow-derived progenitor cells are important for lung repair after lipopolysaccharide-induced lung injury', *J Immunol*, 172: 1266-72.
- Yamamori, T., H. Yasui, M. Yamazumi, Y. Wada, Y. Nakamura, H. Nakamura, and O. Inanami. 2012. 'Ionizing radiation induces mitochondrial reactive oxygen species production accompanied by upregulation of mitochondrial electron transport

- chain function and mitochondrial content under control of the cell cycle checkpoint', *Free Radic Biol Med*, 53: 260-70.
- Yan, F., H. Cao, T. L. Cover, R. Whitehead, M. K. Washington, and D. B. Polk. 2007. 'Soluble proteins produced by probiotic bacteria regulate intestinal epithelial cell survival and growth', *Gastroenterology*, 132: 562-75.
- Yang, W., J. I. Peters, and R. O. Williams, 3rd. 2008. 'Inhaled nanoparticles--a current review', *Int J Pharm*, 356: 239-47.
- Yang, Y., N. Gao, Y. Hu, C. Jia, T. Chou, H. Du, and H. Wang. 2015. 'Gold nanoparticle-enhanced photodynamic therapy: effects of surface charge and mitochondrial targeting', *Ther Deliv*, 6: 307-21.
- Yin, M., Q. Lu, X. Liu, T. Wang, Y. Liu, and L. Chen. 2016. 'Silencing Drp1 inhibits glioma cells proliferation and invasion by RHOA/ ROCK1 pathway', *Biochem Biophys Res Commun*, 478: 663-8.
- Ying, Q. L., J. Nichols, E. P. Evans, and A. G. Smith. 2002. 'Changing potency by spontaneous fusion', *Nature*, 416: 545-8.
- You, J., J. Zhou, M. Zhou, Y. Liu, J. D. Robertson, D. Liang, C. Van Pelt, and C. Li. 2014. 'Pharmacokinetics, clearance, and biosafety of polyethylene glycol-coated hollow gold nanospheres', *Part Fibre Toxicol*, 11: 26.
- Yu, Y. A., S. Shabahang, T. M. Timiryasova, Q. Zhang, R. Beltz, I. Gentshev, W. Goebel, and A. A. Szalay. 2004. 'Visualization of tumors and metastases in live animals with bacteria and vaccinia virus encoding light-emitting proteins', *Nat Biotechnol*, 22: 313-20.

- Zalutsky, M. R., P. K. Garg, H. S. Friedman, and D. D. Bigner. 1989. 'Labeling monoclonal antibodies and F(ab')₂ fragments with the alpha-particle-emitting nuclide astatine-211: preservation of immunoreactivity and in vivo localizing capacity', *Proc Natl Acad Sci U S A*, 86: 7149-53.
- Zalutsky, M. R., and M. Pruszynski. 2011. 'Astatine-211: production and availability', *Curr Radiopharm*, 4: 177-85.
- Zen, Y., T. Fujii, S. Yoshikawa, H. Takamura, T. Tani, T. Ohta, and Y. Nakanuma. 2007. 'Histological and culture studies with respect to ABCG2 expression support the existence of a cancer cell hierarchy in human hepatocellular carcinoma', *Am J Pathol*, 170: 1750-62.
- Zhang, G., Z. Yang, W. Lu, R. Zhang, Q. Huang, M. Tian, L. Li, D. Liang, and C. Li. 2009. 'Influence of anchoring ligands and particle size on the colloidal stability and in vivo biodistribution of polyethylene glycol-coated gold nanoparticles in tumor-xenografted mice', *Biomaterials*, 30: 1928-36.
- Zhang, J. 2014. 'Intestinal Bacteria Regulate Anticancer Therapy Responses', *Cancer Discovery*, 4: 18-18.
- Zhang, X., C. Ye, F. Sun, W. Wei, B. Hu, and J. Wang. 2016. 'Both Complexity and Location of DNA Damage Contribute to Cellular Senescence Induced by Ionizing Radiation', *PLoS One*, 11: e0155725.
- Zhang, Zhen, and John T Yates Jr. 2010. 'Direct Observation of Surface-Mediated Electron– Hole Pair Recombination in TiO₂ (110)', *The Journal of Physical Chemistry C*, 114: 3098-101.

- Zhao, E., Z. Zhao, J. Wang, C. Yang, C. Chen, L. Gao, Q. Feng, W. Hou, M. Gao, and Q. Zhang. 2012. 'Surface engineering of gold nanoparticles for in vitro siRNA delivery', *Nanoscale*, 4: 5102-9.
- Zhao, J., J. Zhang, M. Yu, Y. Xie, Y. Huang, D. W. Wolff, P. W. Abel, and Y. Tu. 2013. 'Mitochondrial dynamics regulates migration and invasion of breast cancer cells', *Oncogene*, 32: 4814-24.
- Zhao, J., M. Zhou, and C. Li. 2016. 'Synthetic nanoparticles for delivery of radioisotopes and radiosensitizers in cancer therapy', *Cancer Nanotechnol*, 7: 9.
- Zhou, X., K. Merchak, W. Lee, J. P. Grande, M. Cascalho, and J. L. Platt. 2015. 'Cell Fusion Connects Oncogenesis with Tumor Evolution', *Am J Pathol*, 185: 2049-60.
- Zinkernagel, A. S., R. S. Johnson, and V. Nizet. 2007. 'Hypoxia inducible factor (HIF) function in innate immunity and infection', *J Mol Med (Berl)*, 85: 1339-46.
- Zorko, M., and U. Langel. 2005. 'Cell-penetrating peptides: mechanism and kinetics of cargo delivery', *Adv Drug Deliv Rev*, 57: 529-45.